

THESIS FOR THE DEGREE OF DOCTOR OF PHILOSOPHY

CORROSION OF METALLIC INTERCONNECTS FOR SOLID
OXIDE FUEL CELLS

MITIGATING CHROMIUM EVAPORATION AND DUAL-ATMOSPHERE CHALLENGES

Matthieu Tomas

Department of Chemistry and Chemical Engineering
CHALMERS UNIVERSITY OF TECHNOLOGY
Gothenburg, Sweden 2024

CORROSION OF METALLIC INTERCONNECTS FOR SOLID OXIDE FUEL CELLS
Mitigating chromium evaporation and dual-atmosphere challenges.

MATTHIEU TOMAS
ISBN 978-91-8103-038-9

© MATTHIEU TOMAS, 2024

Doktorsavhandlingar vid Chalmers tekniska högskola
Ny serie nr 5496
ISSN 0346-718X

Department of Chemistry and Chemical Engineering
Chalmers University of Technology
SE-412 96, Gothenburg
Sweden
Telephone: +46 (0)31-772 1000

Cover:

Graphical abstract describing the Cr(VI) evaporation, the dual-atmosphere effect and the different mitigation strategies investigated in this thesis.

Top-left image is a schematic representation of an interconnect under dual-atmosphere conditions, i.e., humid air on one side and humid hydrogen on the other side. Top-right picture is a scanning electron micrograph of a hematite nodule observed on an AISI 441 sample exposed under dual-atmosphere conditions. Bottom-left image is a top-view optical photograph of the air-side of a ferritic stainless steel. The bottom-middle image is a top-view optical photograph of the air-side of AISI 441 that is Ce/Co-coated on the air-side. The bottom-right image is a top-view optical photograph of the air-side of AISI 441 that is Ce/Co-coated on the air-side and Al-coated on the fuel-side steel, exposed under dual-atmosphere conditions.

Printed by Chalmers Digitaltryck
Gothenburg, Sweden 2024

Corrosion of Metallic Interconnects for Solid Oxide Fuel Cells

Mitigating Chromium Evaporation and Dual-Atmosphere Challenges

MATTHIEU TOMAS

Department of Chemistry and Chemical Engineering
Chalmers University of Technology

Abstract

Solid Oxide Cells (SOCs) are high-temperature energy conversion systems that have attracted attention in the last decades due to their high efficiency. Depending on the operating mode, SOCs can act as either Solid Oxide Fuel Cells (SOFCs), producing electricity from various fuels, or Solid Oxide Electrolyser Cells (SOECs), converting electricity to fuel (e.g., H₂). However, high system costs and limited life-times have hindered their widespread commercialisation. A factor that limits the life-time of an SOC stack is the interconnects, which electrically connect the individual cells. Nowadays, interconnects are made of Ferritic Stainless Steel (FSS) and suffer from severe corrosion owing to operation at high temperatures (600 ° – 900 °C) and in harsh environments.

Degradation phenomena, such as chromium evaporation (CrVI) from the Cr₂O₃ scale and continuous scale growth, negatively impact cell performance due to cathode poisoning and increased electrical resistance, respectively. It has been shown that these degradation phenomena are effectively mitigated by the application of a coating, such as (Co,Mn)₃O₄, sometimes in combination with a “Reactive Element” coating, such as cerium (Ce). This thesis aims primarily to investigate new mitigation strategies that effectively reduce costs and increase the life-span of the SOC stack. The first part of this work investigates the efficiency of using copper (Cu) instead of cobalt (Co) for coating applications in terms of: Cr evaporation, oxide scale growth, oxide microstructure, and area-specific resistance.

Another corrosion phenomenon investigated within the scope of this work, is the dual-atmosphere effect. This effect leads to increased corrosion on the *air-side* of the interconnect if the FSS is exposed to a dual atmosphere, i.e., with hydrogen on the other side. In this thesis, the corrosion behaviours of a selection of uncoated commercial steels are studied under single-atmosphere and dual-atmosphere conditions at 600 °C. Furthermore, the effect of the “fuel gas” composition is investigated. The results show that the fuel-side of the interconnect must be protected to reduce hydrogen ingress.

These observations lead to the last part of this thesis, which is the development and study of hydrogen barrier coatings, so as to reduce hydrogen permeation from the *fuel-side*, as well as a combination of coatings on both sides, to address both of the afore-mentioned degradation mechanisms. The main finding is that a combination of coatings is highly effective.

Keywords: SOFC, SOEC, Corrosion, Interconnect, Dual-atmosphere, Coatings, Area-Specific Resistance.

Acknowledgements

I would like to take this opportunity to acknowledge all the people who made this thesis possible and supported me along the way. Firstly, I would like to thank my main supervisor Professor Jan Froitzheim and my co-supervisor Professor Jan-Erik Svensson for giving me the opportunity to complete my Ph.D. in the Solid Oxide Fuel Cell Group at Chalmers University of Technology. It has been a wonderful experience. As a wise *old* sage once said: “you will never get a better boss than you deserve”. I have been blessed by having two of the best. Thank you for your unwavering support and help throughout these years!

Secondly, I would like to thank my former supervisor Claudia, for giving me the opportunity to join the Solid Oxide Fuel Cell group as an intern, allowing me to become a Ph.D. student. I learned a lot from you, both in Science and in practical aspects. Thanks to you, I feel more confident as a researcher. I would also like to thank the members of the department for their guidance and continuous support over the past 5 years. Also, thank you for all the after-work evenings, which helped with the frustration that comes with doing research. Special thanks to Sandra for helping with all the bureaucracy and always going the extra mile.

This work would not have been possible without the fantastic team with which I have been working for the past years in the Fuel Cell Group. Thank you for welcoming me so warmly and for bearing with me. Special thanks go to Alberto, for the laughs, jokes, happiness, and support, especially during the rough times. Thank you, Reddy, for your always insightful talks, jokes, and unconditional support. They have brightened up my days more than once. Thank you for always tolerating my moody attitude. I will miss our morning *greetings*. Thank you, Camilla and Luca, #The Italians, for your perpetual good mood and the good talks that we had together. Overall, a big thank you to all of you for making the past 5 years exceptional. Thank you, Loli, for always having a smile and a good mood. I will never get enough of this amazing Spanish ham. Thank you, Christine, for the moral support and insightful discussion, either the scientific or more casual ones. Special thanks go to Robin for being an amazing office mate, Swedish teacher and more importantly, a great friend. Special thanks to Hampus for the daily pep-talks, encouragements, praise about my Ph.D. and artistic skills and for being a great friend. Both of you made coming to work much more enjoyable. I will miss our *legendary* ping-pong games. Thank you Hlib for the extra smile and help when things got busy. I would like to extend my thanks to the OOMK teams, as it is filled with great and supportive colleagues who made the journey exceptional.

I would also like to thank my past friends and colleagues who helped me undertake this journey. Thank you, Hannes, for the excellent advice, chats, and support that you gave me during my first internship in the Fuel Cell Group. Thank you for being a great friend. I am missing our chats at midnight about High Temperature Corrosion with a glass of whisky in our hands to stimulate our intellect. Thank you, Valentina, for your unconditional support and friendship throughout the years: always ready to help me even from far away. I would also like to thank you, Andrea, for bringing happiness and laughter to the office. Special thanks also go to Julien for his never-ending friendship and support. Thanks for being the French part at

Chalmers. I will miss our talks in your office and your ability to make me discover new ways to stimulate my nose. A big thank you to Johan for teaching me the best Swedish sentences and your perpetual support throughout our time together sharing the office. I will miss our “intellectual” chats, the scream in the office and those *artistic* screen backgrounds on my computer. Thank you, Tommy, for the excellent atmosphere in the office and for all the help and good insights you provided me with, both in Science and in *Economy*.

Thanks to our industrial partners for interesting new research questions and good discussions. Special thanks to Alleima, Elcogen, Ceres Power and Outokumpu for providing us with the necessary materials and coatings that made this research possible. High-quality research always requires funding, so I would like to acknowledge all the funding that we received, from the High Temperature Corrosion Centre, the Swedish Energy Agency, and the FFI program. In addition, this work was performed in part at the Chalmers Materials Analysis Laboratory, CMAL. Thank you, Michal, for helping me to obtain neat grazing-incidence diffractograms.

I would not be here without the support of my family and friends. Therefore, I would like to take this opportunity to thank my parents, Nathalie Peyruquéou and Jean-Yves Tomas and my step-parents Cathy Tomas and Daniel Satre. Without your continuous support, I would not have been able to achieve this. And all of you know that it has been a long journey on a bumpy road. I will never be grateful enough.

Lastly but most importantly, heartfelt thanks to you, Ema, for you have been my constant companion and source of strength throughout this journey. Your love, support and encouragement have been invaluable to me. I am grateful for your unwavering belief in me and for always being there to cheer me on, no matter how difficult it has been.

List of Publications

This thesis is based on the following publications and manuscript, which are referred to in the text according to their Roman numerals:

Paper I:

Tomas, M., V. Asokan, J. Puranen, J.E. Svensson and J. Froitzheim, “**Efficiencies of cobalt-and copper-based coatings applied by different deposition processes for applications in intermediate-temperature solid oxide fuel cells**”. *International Journal of Hydrogen Energy*, 2022. 47(76): p. 32628-32640.

Paper II:

M. Tomas, J-E. Svensson and J. Froitzheim, “**Evaluation of selected Fe-Cr steels under single- and dual-atmosphere conditions for Intermediate-Temperature Solid Oxide Fuel Cell interconnect applications**”. *International Journal of Hydrogen Energy*, 2024. 65: p. 112-125.

Paper III:

M. Tomas, J-E. Svensson and J. Froitzheim. “**Effect of the fuel gas composition on ferritic stainless steel exposed in dual-atmosphere conditions**”. Manuscript.

Paper IV:

Tomas, M., J.E. Svensson and J. Froitzheim, “**Hydrogen-barrier coatings against dual-atmosphere corrosion for IT-SOFC interconnect applications**”. *International Journal of Hydrogen Energy*, 2024. 58: p. 852-862.

Paper V:

Tomas, M., A. Visibile, J.E. Svensson and J. Froitzheim, “**Novel coatings for protecting solid oxide fuel cell interconnects against the dual-atmosphere effect**”. *International Journal of Hydrogen Energy*, 2023. 48(48): p. 18405-18419.

Contribution report

- Paper I** Principal author with main responsibility for most of the experimental work, data collection, characterisation work and writing. The experimental and analysis work related to the transmission electron microscope results was performed by Dr. Vijayshankar Asokan.
- Paper II** Principal author with main responsibility for the experimental work, data collection, characterisation work and writing.
- Paper III** Principal author with main responsibility for the experimental work, data collection, characterisation work and writing.
- Paper IV** Principal author with main responsibility for the experimental work, data collection, characterisation work and writing.
- Paper V** Principal author with main responsibility for most of the experimental work, data collection, characterisation work and writing. Dr. Alberto Visibile performed parts of the experimental work.

Related papers not included in this thesis

M. Tomas, C. Goebel, J-E. Svensson and J. Froitzheim. **Cu-Based coatings for IT-SOFC applications**. Published in: *ECS Transactions*, 2019 91 (1): p. 2291-2298.

D. Koszelow, M. Makowska, F. Marone, G. Cempura, Matthieu Tomas, Jan Froitzheim, S. Molin. **Pre-oxidation of porous ferritic Fe22Cr alloy for lifespan extension at high-temperature**. Submitted for publication to: *Corrosion Science*.

List of Acronyms

- ASR: Area-Specific Resistance
AWE: Alkaline Water Electrolyser
BIB: Broad Ion Beam
BCC: Body-Centred Cubic
BSE: Back-scattered Electrons
CHP: Combined Heat and Power
CO: Carbon Monoxide
COP: Conference Of the Parties
EDS: Energy Dispersive x-ray Spectroscopy
EU: European Union
FC: Fuel Cell
FCC: Face-Centred Cubic
FSS: Ferritic Stainless Steel
InCF: Intrinsic Chemical Failure
IT-SOFC: Intermediate-Temperature Solid Oxide Fuel Cell
LC: Lanthanum cobaltite, LaCoO_3
 LaCrO_3 : Lanthanum chromite
LSCF: $\text{La}_{1-x}\text{Sr}_x\text{Co}_{1-y}\text{Fe}_y\text{O}_{3-\delta}$
LSM: LaMnO_3
MCO: $(\text{Mn},\text{Co})_3\text{O}_4$
MICF: Mechanical-Induced Chemical Failure
MIEC: Mixed Ionic Electronic Conductor
PEMFC: Polymer Exchange Membrane Fuel Cell
PEMWE: Polymer Exchange Membrane Water Electrolyser
PVD: Physical Vapour Deposition
RE: Reactive Element
SEM: Scanning Electron Microscopy
SMR: Steam Methane Reforming
SOEC: Solid Oxide Electrolysis Cell
SOFC: Solid Oxide Fuel Cell
TEC: Thermal Expansion Coefficient
TEM: Transmission Electron Microscopy
TS: Thermal Spray
YSZ: Yttria-Stabilised Zirconia

Contents

Abstract	i
Acknowledgements	iii
List of Publications	v
List of Acronyms.....	vii
Contents	ix
1. A step closer to a more-sustainable world.....	1
1.1 Transitioning towards Green Energy	1
1.2 Aim of Thesis	4
1.2.1 Coatings: A way to delay the onset of breakaway oxidation	4
1.2.2 Dual-atmosphere effect: A hydrogen conundrum	5
1.3 Relevance of this thesis for the SOEC technology	6
2. Background.....	7
2.1 Fuel Cell	7
2.2 Electrolysis Cell.....	9
2.3 Solid Oxide Fuel Cell	10
2.3.1 Cathode materials.....	11
2.3.2 Electrolyte materials.....	12
2.3.3 Anode materials	13
2.3.4 Interconnect materials	13
2.4 Oxidation of Metals	15
2.4.1 Thermodynamics.....	15
2.4.2 Oxide Scale Growth	17
2.4.3 Kinetics	18
2.4.4 Defects in Oxide Scales.....	21
2.4.5 Chromium Species Evaporation.....	25
3. Corrosion of metallic interconnects	27
3.1 Ferritic Stainless Steels as Interconnects	28
3.1.1 Material Selection	28
3.1.2 Alloying elements	29
3.2 Coatings to Mitigate Cr(VI) Evaporation.....	31
3.2.1 Perovskite-type coating	32
3.2.2 Spinel-type coating.....	32
3.3 Electrical Conductivity of Oxide Scales.....	33

3.3.1	Intrinsic semi-conductors	34
3.3.2	Extrinsic semi-conductors	35
3.3.3	Electrical conductivity of chromia	35
3.3.4	Electrical conductivity of spinels	35
3.4	The Dual-Atmosphere Effect.....	36
4.	Materials and Methods	39
4.1	Materials	39
4.2	Coatings.....	41
4.2.1	Single-atmosphere exposures	41
4.2.2	Dual-atmosphere exposures	42
4.3	Exposures	42
4.3.1	Single-atmosphere conditions	44
4.3.2	Cr(VI) evaporation measurements	44
4.3.3	Gravimetry measurements.....	46
4.3.4	Dual-atmosphere conditions.....	46
4.4	Characterisation Methods	48
4.4.1	UV-VIS spectrophotometry	48
4.4.2	Broad Ion Beam Milling	49
4.4.3	Scanning electron microscopy / Energy-dispersive x-ray spectroscopy	49
4.4.4	Transmission Electron Microscopy.....	51
4.4.5	X-Ray Diffraction	51
4.4.6	Area-specific resistance.....	52
5.	Results & Discussion	55
5.1	Single-Atmosphere Conditions – New Coating Systems to Reduce Cr(VI) Evaporation....	55
5.1.1	Mitigating Cr(VI) evaporation – <i>Efficiency of the coatings</i>	55
5.1.2	Oxidation kinetics – <i>From uncoated to coated steels</i>	58
5.1.3	Microstructural investigation – <i>Uncoated AISI 441</i>	60
5.1.4	Coating composition – <i>A microstructural and chemical investigation</i>	61
5.1.5	Area-specific resistance – <i>Influence of the coating</i>	64
5.2	Dual-Atmosphere Conditions – New Mitigation Strategies.....	66
5.2.1	Uncoated steels – <i>Evaluation of the corrosion behaviour</i>	66
5.2.2	Mitigation of the dual-atmosphere effect – <i>Coatings as hydrogen diffusion barriers</i>	71
5.2.3	ASR evaluation of the coatings – <i>Suitability for interconnect applications</i>	81
6.	Summary & Outlook.....	83
	References.....	87
	List of Figures.....	103

1. A step closer to a more-sustainable world

“Anything capable of being imagined will one day be made reality.”

—Jules Verne

1.1 Transitioning towards Green Energy

Global warming can significantly impact our way of life, the economy, the society and more importantly the environment. The annual levels of CO₂ emitted to the atmosphere (Figure 1.1) are at an all-time high in recorded human history [1]. The first consequences are already being felt around the globe. In the 2020s, environmental disasters, such as the forest fires seen in California and Australia, have led to extensive killing of wild-life and damage to the ecosystems in those regions. Global temperature increases of as little as 2 °C could accelerate dramatically the melting of the glaciers and result in rising sea levels, leading to the disappearance of land masses. If no direct actions are taken, humanity will reach a point of no return after which changes in the climate system become self-perpetuating and have serious consequences [2]. It seems likely that the principal goal of restricting global warming to 1.5°C above the pre-industrial level, as set by the United Nation Climate Change Conference, more commonly referred to as the Conference of the Parties (COP), will not be achieved, as latest estimations indicate that such an increase will be likely be reached already by 2030 [2].

Societies need to switch from using fossil fuels, such as coal, oil and gas, to adopting more-sustainable energy sources, such as solar energy, wind energy, geothermal energy, and hydrogen, to reduce greenhouse gas emissions. The use of fossil fuels is responsible for most of the CO₂ emissions, exceeding 35 GtCO₂ in 2022 [3]. Therefore, reducing these emissions is crucial, even if countries are facing demographic growth and rising living standards, which complicate a rapid transition. The switch relies mainly on advanced renewable energy generation systems, such as solar panels or wind turbines that are rapidly scalable. Since 2010, the amount of primary energy provided by solar and wind power has increased seven-fold [4]. However, such systems are intermittent and face significant challenges, as energy patterns differ significantly depending on factors such as geography, weather, and time. Long-term energy storage is necessary to bridge the gap between peak-hour demand and low-production periods, to ensure a continuous supply of energy to the grid. Although batteries are becoming more efficient, they are only effective and economical in the short term, to meet peak demand and for grid balancing [5].

A promising, long-term energy storage form is chemical storage, whereby the energy produced using renewable energy sources is transformed into chemical energy and stored. One example of this is the electricity generated by solar or wind sources to produce hydrogen via electrolysis, which can then be stored and converted back to electricity when needed, for

example in Solid Oxide Fuel Cells (SOFCs). Hydrogen is a useful energy carrier that can be used to decarbonise hard-to-abate sectors such as steel-making, cement manufacturing, and building material production, which are responsible for 23 % of global annual CO₂ emissions, with China accounting for 30 % of the total emissions [6].

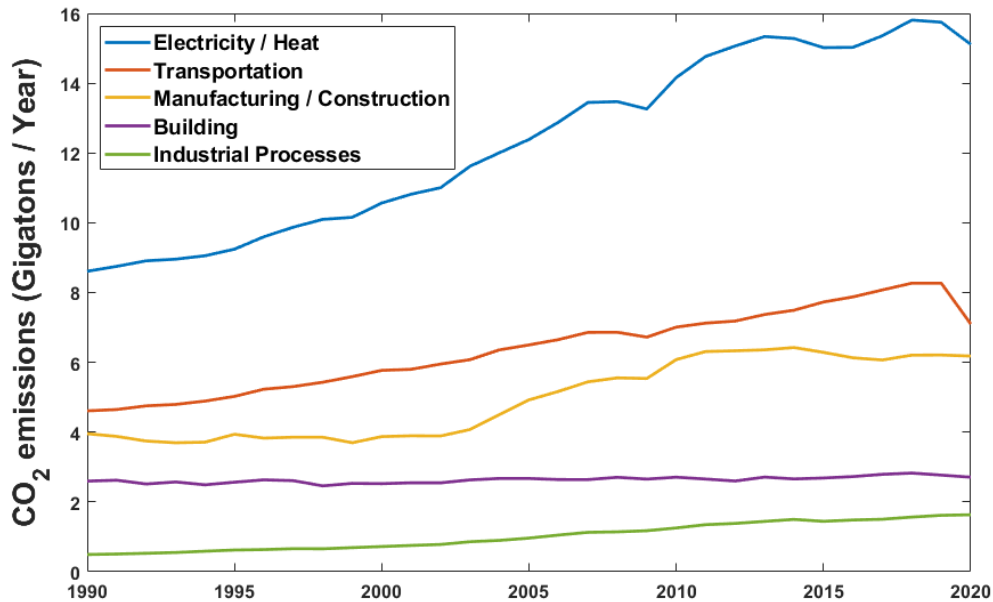


Figure 1.1: Annual CO₂ emissions by sector worldwide for the period of 1990 – 2020. Source: [7].

Nowadays, roughly 95 % of all hydrogen is produced from fossil fuels through the steam methane reformation (SMR) of natural gas, and is mainly used for petroleum refining, and chemical and fertilizer production [8]. While there are other ways to produce hydrogen (see Figure 1.2) so as to reduce CO₂ emissions, they remain controversial or challenging in terms of meeting the demand. The European Union (EU) wants to develop renewable hydrogen and aims at producing up to 10 million tonnes by 2030 [9]. Hydrogen is considered to be renewable when the energy source used to produce it is also regarded as renewable. When generated during periods of ample solar and wind energy resources, renewable hydrogen has the capacity to bolster the EU's electricity sector, providing long-term and large-scale storage. The storage of hydrogen is particularly beneficial for power grids, as it allows for renewable energy to be retained not only in large quantities, but also for long periods of time. This means that renewable hydrogen contributes to enhancing the flexibility of energy systems, addressing imbalances in the supply and demand during periods of excess or insufficient power generation, thereby helping to boost energy efficiency throughout the EU.

Solid Oxide Cells (SOCs), such as SOFCs, and electrolyzers such as Solid Oxide Electrolyser Cells (SOECs) are promising technologies that enable hydrogen ecosystems to be used as potential solutions for climate change. Fuel cells are electrochemical devices that allow conversion of the chemical energy of a fuel to electrical energy. These cells are highly efficient, silent and have very low emissions, making them attractive for mobile applications, back-up power, and power generation. In contrast, electrolyzers work in the opposite way, using electricity to split water molecules to generate hydrogen and oxygen. The hydrogen produced

through electrolysis is considered one of the critical elements for the energy transition and decarbonisation.

Interconnects or bi-polar plates are essential for any fuel cell or electrolyser system. Their primary function is to connect multiple fuel cells in series, so as to form a stack with an acceptable voltage output. Ceramic interconnects have been replaced with interconnects made from Ferritic Stainless Steel as ways to reduce costs and improve performance. In general, FSS account for most of the stack cost [11, 12]. In order to be commercially viable, the price per kWh for SOFCs must be reduced. This involves reducing the costs for materials through the use of commercially available FSS, decreasing the total cost of coating the steel, and reducing the operating temperature [13, 14]. Another challenge that the SOFC system faces is its limited life-time. For stationary systems to be commercially viable, the expected life-time has to be in

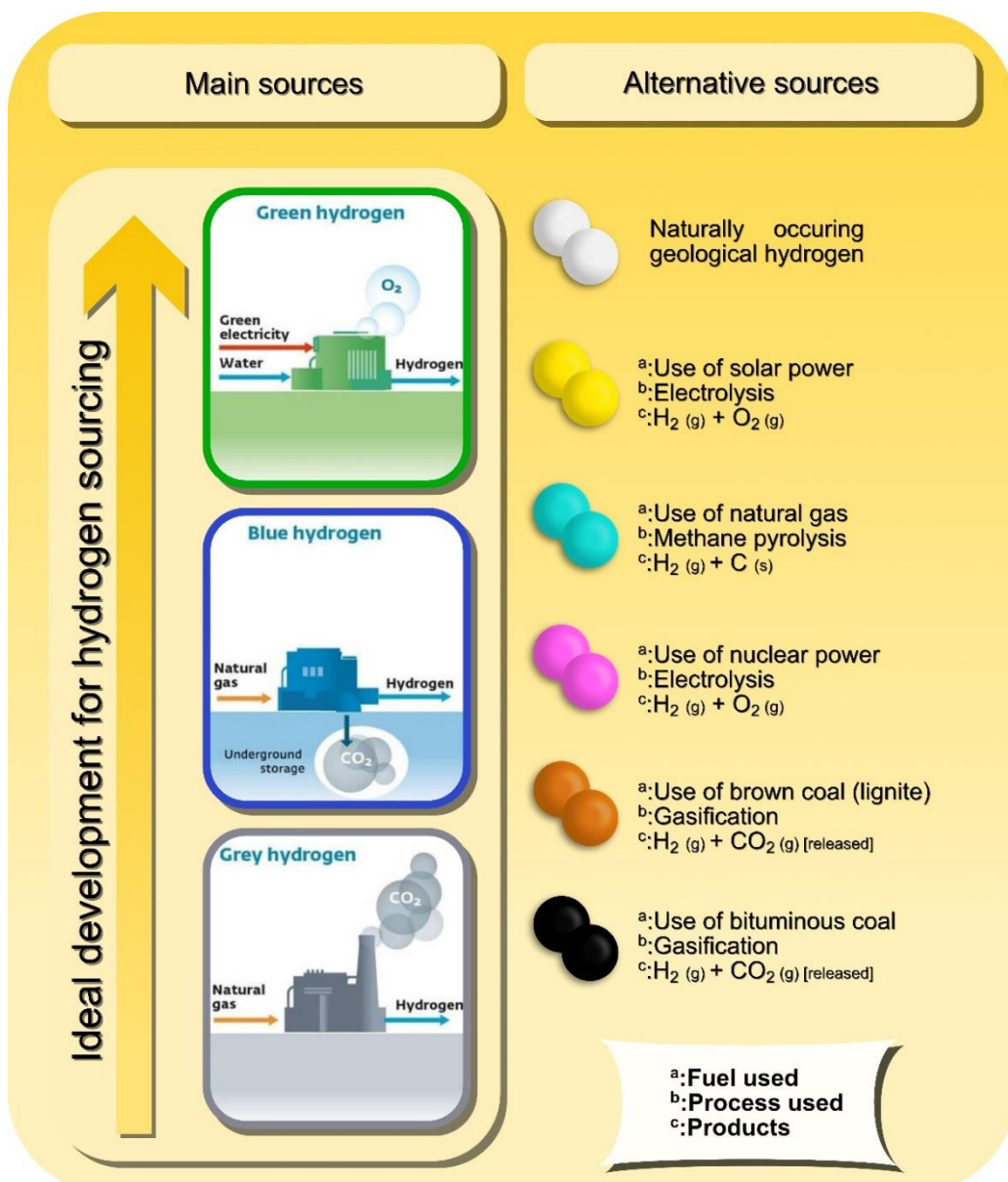


Figure 1.2: Graphical abstract displaying the different colours attributed to hydrogen, and the end-products, depending on the source of energy and production method used. Partially taken from [10].

the range of 40,000 – 80,000 h [15, 16]. Recently, researchers at the Jülich Research Centre [17] tested an SOFC stack for up to 100,000 h, representing a major milestone in SOFC development. However, the use of FSS as interconnects makes attaining long life-time more challenging. FSS interconnects undergo high-temperature corrosion when exposed to temperatures ≥ 600 °C. Phenomena such as increased electrical resistance, Cr(VI) evaporation, and the dual-atmosphere effect strongly impact the life-times of the interconnects and the cells [18-20], degrading overall cell performance. To overcome these barriers, specifically designed steels have been developed for interconnect applications. However, these steels are expensive to produce and drastically increase the overall cost of the system. The preferred strategy to mitigate corrosion of the FSS interconnects is to apply protective coatings. From the economic point-of-view, the use of cheap commercial steel in combination with protective coatings is a viable option. Therefore, it is essential to investigate and compare low-cost and specifically designed steels. Materials development for metallic interconnects to be used in SOFC applications is highly relevant for SOEC systems, as it is based on the same technology and is facing similar issues. Therefore, most of the findings in this thesis can also be applied to the SOEC technology.

1.2 Aim of Thesis

The commercialisation of SOFC technology has been hindered by critical factors such as material costs and service life-time. Although cheaper materials may reduce the overall cost, they must perform as effectively as their more-expensive counterparts. The aim of this thesis is to investigate the degradation mechanisms for the metallic materials used in SOFC systems. In order to render SOFCs more attractive commercially, it is necessary to reduce the costs without reducing the overall performance of the SOFC stack. This work mainly focuses on ways to improve the corrosion resistance of cheaper commercial steels by means of coatings, and on understanding the corrosion mechanism underlying the high-temperature oxidation of metallic interconnect materials.

1.2.1 Coatings: A way to delay the onset of breakaway oxidation

Custom-made steels with protective coatings represent state-of-the-art materials for interconnect applications. Protective coatings are essential to mitigate Cr(VI) evaporation, reduce the growth of the chromia layer or reduce the hydrogen ingress from the fuel-side, thereby improving the overall performance of the fuel cell stack. However, to reduce the overall cost of the SOFC stack, the use of cheaper steels must be investigated. Steels such as AISI 441 can become an interesting candidate once coated. Most state-of-the-art coatings are based on cobalt (Co), which the EU defines as a critical raw material. In **Paper I**, the effectiveness of Cu-based coatings is compared to that of a state-of-the-art Ce/Co coating with regards to Cr(VI) mitigation, oxidation kinetics, and area-specific resistance in a single-atmosphere environment. Interconnects are subject to two different atmospheres in an SOFC stack, with the *air-side* exposed to humid air and the *fuel-side* exposed to fuel. This atmosphere combination leads to a phenomenon called *the dual-atmosphere effect*, which entails increase corrosion on the air-

side of the interconnect due to the presence of hydrogen on the fuel-side of the interconnect. Many studies have focused on trying to understand how the dual-atmosphere effect affects the steel composition. **Papers II** and **III** evaluate different grades of steels and their behaviours under dual-atmosphere conditions in terms of the steel composition and fuel atmosphere.

In the past decade, research has mainly focused on air-side coatings with different combinations of coating types and deposition processes, ignoring the potential impact of the uncoated fuel-side. Therefore, it is relevant to investigate the effects of coatings on the fuel-side of the interconnect. **Paper IV** aims at providing insights into the different potential fuel-side coatings and their levels of effectiveness in terms of corrosion resistance and area-specific resistance. Long-term performance of the coatings is essential, as they have to remain protective over the life-time of the stack. **Paper V** investigates the long-term performance of an Al₂O₃ coating on the fuel-side, both as a stand-alone system and in combination with a Ce/Co coating on the air-side.

1.2.2 Dual-atmosphere effect: A hydrogen conundrum

Finally, the present thesis investigates the dual-atmosphere effect in greater depth. This effect occurs when FSS is exposed to fuel on one side and air on the other side, leading to increased corrosion on the air-facing side of the steel. This does not happen in an air-only atmosphere. The present work examines this effect with regards to the following factors:

- Steel composition, i.e., what impacts do the different alloying elements have, and how do they help against the dual-atmosphere effect?
- Hydrogen concentration, i.e., what impact does a higher hydrogen concentration have on the corrosion properties of specially designed and cheap commercial steels?

The trend towards using cheaper commercial steels to reduce the cost of the fuel cell stack raises issues, given that the steel composition, i.e., the Cr content or the presence of alloying elements, can impact drastically the corrosion properties of the steel. **Paper II** investigates several different grades of uncoated commercial steels and their behaviours towards the dual-atmosphere effect, as well as the effects that intermetallic compounds, such as Laves phases, might have on the severity of the dual-atmosphere effect. Many theories have been proposed regarding the dual-atmosphere effect, but the phenomenon remains incompletely understood. A recent paper [21] has hypothesised that hydrogen is responsible for slowing Cr diffusion to the outer scale, leading to increased corrosion on the air-side of the interconnect. In exploring this hypothesis, **Paper III** investigates interconnects that are exposed to a higher concentration of hydrogen, higher humidity, or a combination of both, to understand the effect of each parameter. Before presenting and discussing the results obtained in this thesis (Chapter 5), Chapters 2 and 3 provide additional insights into the fuel cell system, high-temperature corrosion, and the context of this work. Details of the experimental set-ups employed are outlined in Chapter 4, while a summary of the results and conclusions can be found in Chapter 6.

1.3 Relevance of this thesis for the SOEC technology

While the research on metallic materials and coatings is mainly discussed in the context of SOFC applications, it is also highly applicable to SOEC systems. Indeed, the SOEC technology suffers from similar degradation mechanisms. While in SOFC mode the fuel inlet (H_2) is characterised by a high H_2/H_2O ratio with increasing $p(H_2O)$ towards the outlet, the opposite applies in SOECs. In any case, both SOFC and SOEC interconnects must remain stable over a wide range of H_2/H_2O ratios.

The presence of hydrogen on the fuel-electrode (cathode) induces the dual-atmosphere effect (described in detail in Section 3.4). This phenomenon induces increased corrosion on the O_2 -electrode side (anode) of the interconnect. Therefore, hydrogen ingress through the steel must be hindered to increase the life-span of the interconnect. Since the water vapour concentration is low on the anode side, Cr evaporation should be relatively small. However, the continuous growth of a Cr_2O_3 scale leads to increased Area-specific Resistance (ASR). Therefore, coatings reducing the chromia scale growth are necessary to limiting the increase in electrical resistance.

Therefore, mitigation strategies are needed, and the development of coatings and steel compositions for the SOFC technology becomes relevant for SOEC systems.

2. Background

“I believe that water will one day be employed as fuel, that hydrogen and oxygen which constitute it, use singly or together, will furnish an inexhaustible source of heat and light, of an intensity of which coal is not capable.”

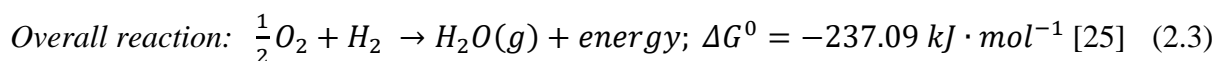
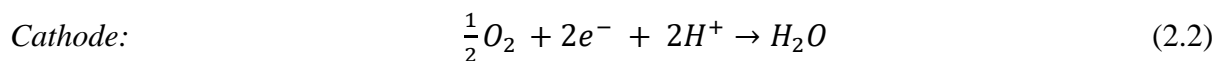
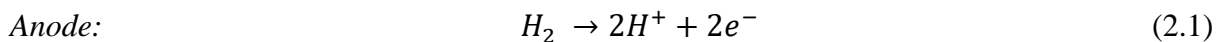
– Jules Verne

Fuel cells that convert chemical energy into electrical energy were independently described in 1838/1839 by two scientists, William Grove [22, 23] and Christian Friedrich Schönbein [24]. They used a *gas battery* to prove that an electrochemical reaction between hydrogen and oxygen could produce an electric current. These discoveries opened the way for new green energies, such as FCs, batteries and electrolysis [25]. In the early 20th Century, Friedrich Wilhelm Ostwald, who is considered to be the founder of physical chemistry, experimentally determined the interconnections between the various components of a FC: electrodes, electrolyte, oxidising and reducing agents, anions, and cations, with his work representing an important contribution to the field.

Fuel cells convert chemical energy into electrical energy through a controlled chemical reaction between a fuel and air. The working principle of FCs is simple: split the electrochemical reaction into two half-reactions while limiting the electrical transfer of electrons, thereby creating a difference in electrical potential. In FCs, the chemical reaction is spontaneous, and produces electricity.

2.1 Fuel Cell

Fuel cells function in a manner similar to batteries. A chemical redox reaction is locally separated into oxidation and reductions reactions. This separation avoids direct reaction and means that the redox reaction is instead controllable, and the electrons are transferred through the external circuit, providing electrical energy. The main difference between a battery and an FC is that a battery releases the stored energy, whereas an FC generates energy from a fuel. The first FCs described by Grove and Schönbein were based on the highly exothermic reaction between hydrogen and oxygen to form water. The redox reactions are expressed by Equations (2.1), (2.2) and (2.3):



where ΔG^0 is the Gibbs free energy under standard conditions (298 K, 10⁵ Pa) for 1 mol of H₂O.

The oxidation of hydrogen occurs at the anode, while at the cathode, the reduction of oxygen occurs. An electrolyte separates the fuel from the air and facilitates the electrochemical reaction by conducting specific ions at a high rate, while limiting electron transfer. The electrons are transmitted through an external circuit [26]. Nowadays, many types of FCs exist, with the main differences being the choice of electrolyte, which influences other parameters, such as the operating temperature, fuel flexibility and fuel cost. While conventional combustion power plant has an efficiency of roughly 30 % [27], FCs can achieve an electrical efficiency of up to 65 % [28]. Fuel cells operate silently and exhibit low levels of wear and tear, which means that they have lower maintenance costs and higher system stabilities. Moreover, their use is associated with low levels of emissions and the absence of pollutant emissions such as NO_x and SO_x, due to the absence of combustion. However, owing to the high cost, this technology has seen limited commercialisation. Furthermore, FCs are sensitive to environmental poisoning because of their complex electrochemical processes and interfaces. There are five main types of FCs:

- Polymer Electrolyte Membrane Fuel Cell (PEMFC)
- Phosphoric Acid Fuel Cell (PAFC)
- Alkaline Fuel Cell (AFC)
- Molten Carbonate Fuel Cell (MCFC)
- Solid Oxide Fuel Cell (SOFC)

Regardless of their differences with respect to electrolytes and mobile ions, all FCs operate according to the same electrochemical principle (for more-detailed information, see Figure 2.1).

One of the most widely used FCs are Polymer Exchange Membrane Fuel Cells (PEMFC). These FCs have the advantage of reaching efficiencies of up to 50 %, have low operating temperatures, in the range of 70 ° – 110 °C, are suitable for mobile applications thanks to quick start-up times, and have good power outputs [29]. However, they require a catalyst, e.g., expensive platinum, for operation. In addition, pure hydrogen must be used as the fuel and it should not be contaminated with carbon monoxide (CO) [30]. This limitation of high-purity H₂ significantly impacts the application of this technology in many cases. In contrast, SOFCs operate according to the same principle but at much higher temperatures (600 ° – 900 °C). The SOFC technology is being considered because of its greater fuel flexibility (using fuels such as methane or ammonia). Thus, SOFCs can operate with hydrocarbons using the existing infrastructure, thereby allowing a smoother energy transition from fossil-based to renewable energy systems. SOFCs have high electrical efficiencies (> 60 %), and by recycling the produced heat, in Combined Heat and Power (CHP) units, the efficiency can be raised to 90 % [31, 32]. SOFCs can be operated in reverse mode, to generate fuel from electricity as Solid Oxide Electrolysis Cells (SOECs). However, SOFCs/SOECs have longer start-up times and are operated at high temperatures, resulting in accelerated material degradation and higher

costs, which are significant obstacles to widespread commercialisation of the technology. An SOEC can produce Green H₂, which is emerging as the new sustainable fuel for the future and attracting increasing interest from different fields world-wide. This work addresses the challenges of using metallic materials in SOFCs, although most of the gathered knowledge could also be applied to the SOEC system [33].

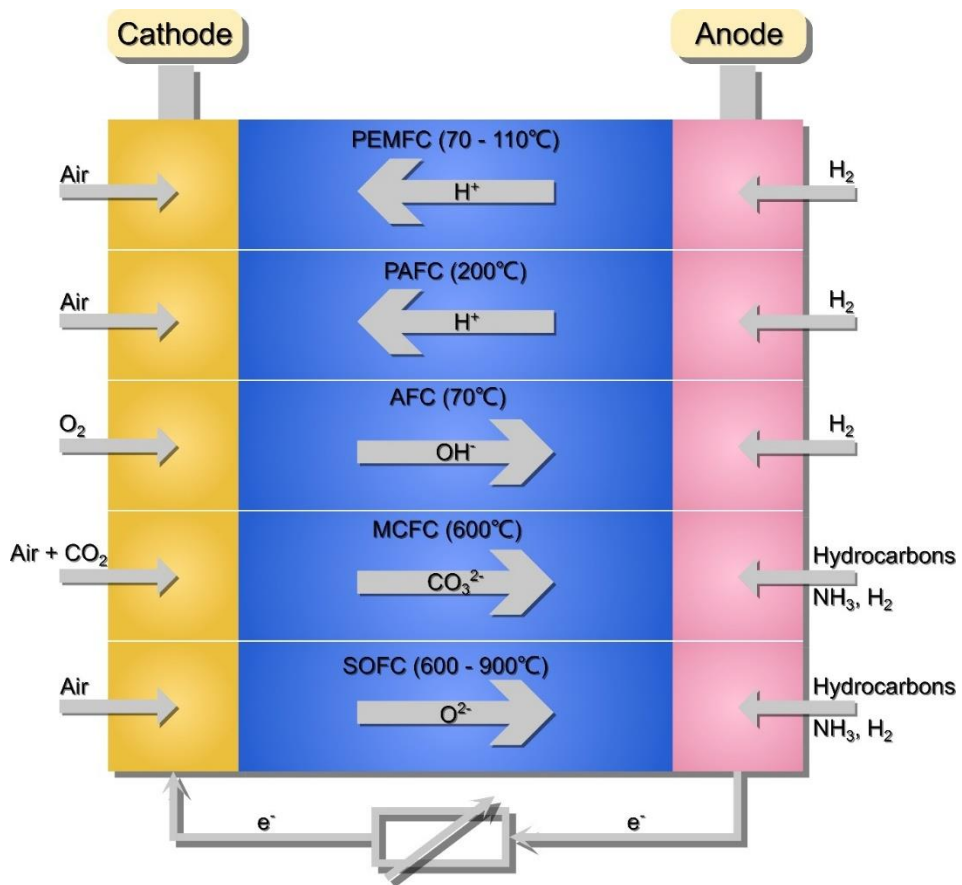
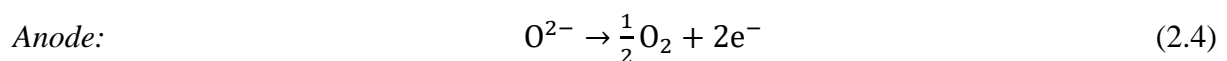
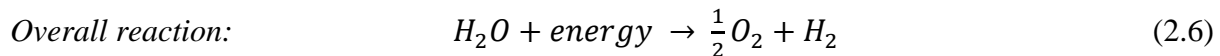
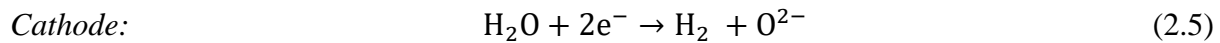


Figure 2.1: Different fuel cell systems. Adapted from [34].

2.2 Electrolysis Cell

An electrolyser is a device that utilises electricity to induce a non-spontaneous chemical reaction known as electrolysis [35]. It typically consists of an electrolyte and two electrodes. In water electrolysis, the electrical current splits the water molecule to generate hydrogen and oxygen at the cathode and anode, respectively. The basic overall reaction that occurs in electrolysis cells is represented by Equation (2.6). The electrolysis of water can be separated into two half-equations: one for oxidation [see Equation (2.4)] and one for reduction [see Equation (2.5)]. This process splits water molecules into hydrogen and oxygen gases, which is crucial for producing hydrogen fuel through renewable resources such as water and renewable electricity.





Electrolysers play a significant role in the advancement of clean energy technologies, offering promising avenues for sustainable hydrogen production and energy storage. Three main types of electrolysis cells are used for hydrogen production, based on the electrolyte type used [35, 36]:

- Alkaline Water Electrolyser (AWE)
- Proton Exchange Membrane Water Electrolyser (PEMWE)
- Solid Oxide Electrolysis Cell (SOEC)

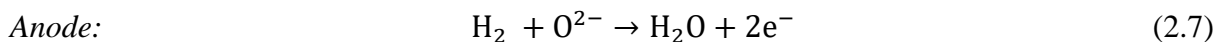
The most-commonly used electrolyser is AWE, which uses hydroxide ions (OH^-) as the ionic carrier and operates in the temperature range of $70^\circ - 90^\circ\text{C}$. Depending on the scale of production, the consumption of electricity can account for up to 75 % of the cost of hydrogen production [35]. Although the enthalpy in Equation (2.6) is increasing with temperature, the change is small compared to the decrease in electrical energy required [37]. Therefore, electrolysis at high temperatures requires a lower applied voltage for the reaction to happen.

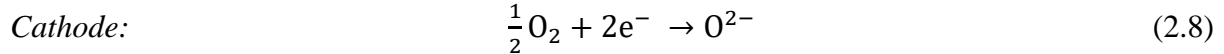
The SOEC technology operates at high temperatures and is based on technology similar to that of SOFC. It represents a promising technology that can contribute to the hydrogen production ecosystem. High-temperature electrolysis presents the following advantages:

- Cheap thermal energy from various sources can be used to reduce electricity consumption, thereby reducing the cost of hydrogen production
- SOECs can be utilised to generate syngas ($\text{H}_2 + \text{CO}$) and/or can be thermally integrated into a wide range of chemical processes

2.3 Solid Oxide Fuel Cell

Solid Oxide Fuel Cells are based on a ceramic electrolyte that is permeable to O^{2-} ions, such that the reduction and oxidation that take place in SOFCs differ from, for example, those in PEMFC. Figure 2.2a shows the working principle of an SOFC that is using H_2 as the fuel. The oxidation of H_2 into H_2O occurs at the anode [see Equation (2.7)]. The electrons that are set free during the oxidation are transferred through an external circuit to the cathode, where O_2 is reduced to O^{2-} [see Equation (2.8)]. The O^{2-} ions can then diffuse through the solid electrolyte to the anode, where the O^{2-} ions react with the protons and form water. When hydrogen is used as fuel, the overall reaction is shown in Equation (2.3).





While a single cell can deliver up to 1.23 V, due to different factors, such as electrochemical and polarisation losses, the applied energy output is typically <1.0 V [38]. This is too low for any application. Therefore, multiple cells have to be stacked and electrically connected in series through interconnects to form an FC stack (see Figure 2.2b). All the components, i.e., the electrodes, the electrolyte, and the interconnect, must fulfil certain requirements. These are discussed in the following section, along with information about the state-of-the-art materials. One requirement that all components must comply with is matching the Thermal Expansion Coefficient (TEC), so as to avoid the build-up of thermal stresses during start-up and shut-down [39].

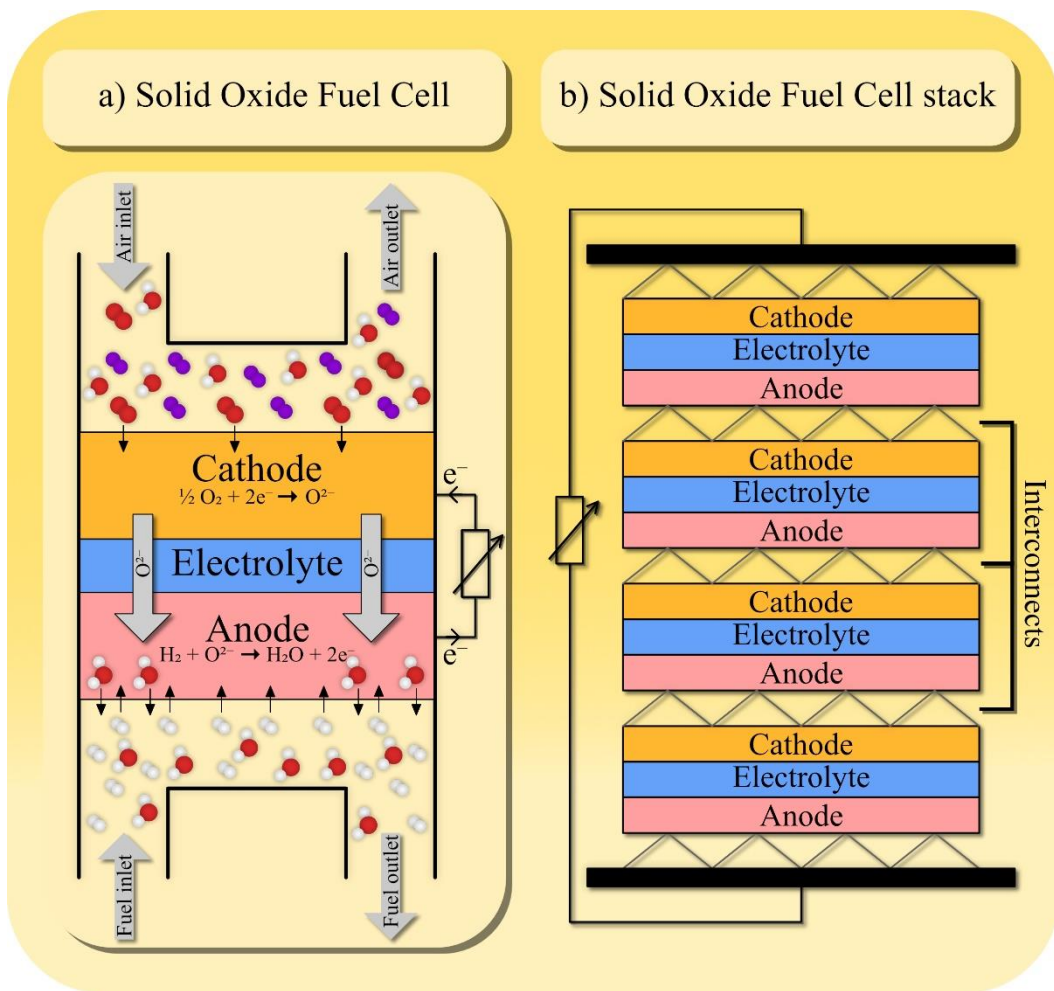


Figure 2.2: Solid oxide fuel cell: a) operating principle; and b) fuel cell stack.

2.3.1 Cathode materials

The cathode plays a crucial role as the location at which the oxygen reduction reaction occurs, thereby significantly influencing the cell performance. Excellent electron conductivity of the cathode material is essential, as electrons are necessary for the reduction of oxygen

molecules. Furthermore, the cathode material should: exhibit minimal or no chemical reactivity with other cell components; be porous, to ensure adequate gas flow; possess a compatible TEC; and demonstrate high catalytic activity for the reduction of oxygen molecules. A frequently used cathode material is Sr-doped LaMnO₃ (LSM). However, its poor oxygen ion conductivity leads to a small Triple-Phase boundary (TPB), which is the air-cathode-electrolyte interface. The addition of Yttria-Stabilised Zirconia (YSZ) increases the oxygen ion conductivity of LSM [40, 41]. LaCoO₃ (LC) is another perovskite oxide with superior electronic conductivity compared to LSM. However, its poor stability poses a challenge. Around 1,000°C, LaCoO₃ dissociates into other phases at $p\text{O}_2$ values $<10^{-7}$ atm (in comparison, LaMnO₃ decomposes at $p\text{O}_2$ of about 10^{-15} atm). The TEC of LaCoO₃, is higher than that of LaMnO₃, which means that it does not meet one of the requirements for SOFC components. In addition, at high temperatures, LaCoO₃, tends to be more reactive with YSZ than LaMnO₃ [42]. These issues have been addressed through strontium (Sr)-doping. This involves partially replacing the La in the structure, resulting in Sr-substituted cobaltite perovskites, known as LSC ($\text{La}_{1-x}\text{Sr}_x\text{CoO}_{3-\delta}$) [43]. LSC, which is characterised as a mixed conductor material, exhibits good ionic conductivity and oxygen reduction catalytic properties [44]. However, LSC has a significant drawback due to its high TEC, which is higher than those of commonly used electrolytes such as YSZ and gadolinia-doped ceria (CGO). To address this issue, researchers have substituted Co with Fe, leading to the development of the advanced cathode material: $\text{La}_{1-x}\text{Sr}_x\text{Co}_{1-y}\text{Fe}_y\text{O}_{3-\delta}$ (LSCF). This material exhibits significant electronic conductivity, ranging from $350 \text{ S}\cdot\text{cm}^{-1}$ to $250 \text{ S}\cdot\text{cm}^{-1}$ within the temperature range of $600^\circ - 800^\circ \text{C}$ [43]. LSCF is the most-commonly used cathode material in Intermediate-Temperature Solid Oxide Fuel Cells (IT-SOFCs).

2.3.2 Electrolyte materials

In SOFCs, the electrolyte materials must meet several criteria, including good ionic conductivity, low electrical conductivity, lack of permeability to gases, and stability in both fuel and oxygen atmospheres [43]. The most commonly used electrolyte material for high operating temperatures (above 700 °C) is YSZ, which is zirconia (ZrO_2) doped with yttria (Y_2O_3). YSZ provides a good balance between ionic properties, mechanical strength, conductivity, and cost. It has been shown that ZrO_2 doped with 8 mol% Y_2O_3 [7] constitutes the optimal option for ion conduction [45, 46].

Another popular electrolyte is gadolinium-doped ceria (CGO) which is ceria (CeO_2) that is doped with approximately 20 % gadolinium oxide (Gd_2O_3) [47]. CGO has a higher electronic conductivity than YSZ, allowing for lower operating temperatures. At temperatures below 800 °C, the ionic conductivity of CGO is two orders of magnitude higher than that of YSZ. However, in CGO electrolytes under anodic conditions at these operating temperatures, Ce^{4+} ions are reduced to Ce^{3+} ions, which are responsible for n-type electronic conduction, and this short-circuits the FC, thereby reducing its performance [43]. Magnesium (Mg)-doped lanthanum gallate, $\text{La}_x\text{Sr}_{1-x}\text{Ga}_y\text{Mg}_{1-y}\text{O}_{3-\delta}$ (LSGM), has gained attention for its good ionic conductivity, positioning it as a promising electrolyte.

This material exhibits exceptional oxide-ion conductivity within the intermediate temperature range, making it highly suitable for the development of materials for IT-SOFCs. The excellent ionic conductivity of LSGM is attributed to the vacancies introduced into the perovskite structure of lanthanum gallate (LaGaO_3) by Sr-doping and Mg-doping [43].

2.3.3 Anode materials

The primary role of the anode material in the FC is to catalyse fuel oxidation and thereafter, conduct the electrons generated by oxidation of the fuel to the external circuit. Similar to the cathode, an efficient anode material should possess favourable catalytic properties and electronic conductivity, so that it can fulfil its primary functions of catalysing fuel oxidation, conducting the electrons to the external circuit, and acting as a porous material to allow sufficient gas flow [43, 48]. In contrast to the cathode material, the stability of the anode material must be able to sustain reducing atmospheres. Nickel (Ni), which is a good electronic conductor is commonly used in anodes [43, 48]. However, its high TEC makes it mechanically incompatible with electrolytes such as YSZ. Therefore, Ni is often utilised in composite forms. There has been a trend in anode material development towards the employment of Mixed Ionic Electronic Conductor (MIEC) materials with porous structures. A commonly used anode material is a cermet (ceramic-metallic composite), which consists of a mixture of Ni and YSZ, forming Ni-YSZ [43, 48]. This mixture of an electrolyte material and a material with high electron conductivity allows for a good TEC match between the anode and electrolyte and ensures pore formation, although reports have suggested that a cermet of Ni with ceria doped with gadolinia, known as Ni-CGO, can outperform Ni-YSZ anodes [43, 48]. Despite its efficiency, Ni-YSZ faces challenges such as carbon deposition and sulphur poisoning, which affect its performance. Nevertheless, it remains the state-of-the-art anode for high-temperature SOFCs due to its high electrochemical activity and mechanical stability. For IT-SOFCs, Ni-CGO is emerging as a popular anode material. While CGO lacks electronic conductivity on its own, when Ni is added as a compensatory element the CGO exhibits high ionic conductivity [43, 48].

2.3.4 Interconnect materials

To achieve higher voltages, multiple cells are electrically connected in series with the help of interconnects, to form a stack (see Figure 2.2). The interconnect distributes the electrical current to the cell and separates the anode and cathode atmospheres from one cell to another. The basic requirements for an interconnect are similar to those for the electrolyte. However, while the electrolyte is a good ionic conductor and poor electronic conductor, the interconnect must be a good electronic conductor and a poor ionic conductor [49]. Thus, the interconnect material of an SOFC needs to have certain properties, such as:

- High electronic conductivity and low ionic conductivity
- Thermal stability in the cathode- and anode-side environments at high temperatures (600 ° – 900 °C) over a prolonged period of time

- Thermal expansion coefficient that is aligned with that of the ceramic electro-active components
- Impermeable to gases
- Sufficient mechanical strength
- Easy to manufacture and low cost

2.3.4.1 Ceramic interconnects

Ceramic materials with the perovskite structure, specifically those derived from LaCrO_3 , have the desired properties for interconnect materials [49]. However, the main limitations of these ceramics include their brittleness, high cost, labour intensiveness, and challenging shaping processes. This is particularly problematic in certain planar stack configurations, where the interconnector serves as both the mechanical support for delicate ceramic components and as the gas-tight barrier that separates the fuel gas and oxidant. Competitive materials, such as yttrium chromites [42, 50], neodymium chromites, and strontium titanates, have yielded promising outcomes [51, 52]. Nevertheless, the high material costs associated with rare earth-containing perovskites make their use in ceramic interconnects suitable only for situations in which the stack design mandates minimal quantities of material [53]. Consequently, the interest in advanced ceramic interconnects has waned in recent years, with the focus shifting towards the development of metallic interconnect materials.

2.3.4.2 Metallic interconnects

Due to the decrease in operating temperature to $600^\circ - 800^\circ\text{C}$ brought about by improvements in electrolyte and electrode materials, research is nowadays focused on metallic interconnects rather than ceramic interconnects. The primary disadvantage of using metals and alloys in SOFC systems is their susceptibility to react with the environments on both the anode and cathode sides at high operating temperatures. This reactivity gives rise to high-temperature corrosion phenomena and dimensional changes, as well as the development of surface oxide scales, which typically exhibit poor electrical conductivities [54-56]. Noble metals have been considered as potential interconnect materials. However, apart from problems with high cost, limited availability, and large-scale production, the main technical inconvenience of using a metal such as silver is its ability to dissolve large amounts of oxygen and hydrogen, leading to the formation of voids through the nucleation of water vapour bubbles when exposed to dual-atmosphere conditions [57]. In early studies of metallic interconnects, conventional high-temperature alloys were considered as possible candidates. A key characteristic of these high-temperature alloys is their capacity to grow protective surface oxide scales at rates that are slow enough to maintain the corrosion at a reasonable level [49, 58].

Among the oxides that may develop on commercially available materials exposed to high temperatures, only Al_2O_3 , SiO_2 , and Cr_2O_3 offer the potential to achieve low rates of material degradation [54]. If one were to prioritise oxidation rates at high temperatures as the primary selection criterion for interconnector applications, alloys classified as alumina formers, such as Ni-Cr-Al, Co-Cr-Al, and especially Fe-Cr-Al, would be the preferred materials [59]. These

alloys exhibit excellent resistance to oxidation/corrosion owing to the formation of an alumina scale that grows extremely slowly on the material surface at high temperatures. However, the extremely low electronic conductivity of alumina renders these alloys unsuitable for interconnect applications [60-62]. Also, alloys that form silica are excluded from use as interconnect materials due to their low electrical conductivity of SiO_2 . As a result, most studies have focused on the qualification and/or development of metallic, high-temperature materials for interconnect applications, with efforts centred around chromia-forming alloys. While chromia provides weaker oxidation/corrosion protection than alumina, its electronic conductivity in the SOFC operational temperature range ($600^\circ\text{C} - 900^\circ\text{C}$) is orders of magnitude higher than that of alumina or silica [63].

Stainless steels fulfil most of the requirements for interconnect materials listed above. They are good thermal and electronic conductors, easy to shape, and much cheaper than ceramics. Ferritic stainless steels have TECs that are similar to those of other cell components (electrodes and electrolytes) and, therefore, they are the main choice as interconnect materials [49, 64]. More details about the properties of metallic interconnects, related corrosion degradation mechanisms, and mitigation strategies are presented in Chapter 3.

2.4 Oxidation of Metals

Corrosion is the gradual degradation of a material (often metallic) through a reaction with its environment. When exposed to conditions under which they are not thermodynamically stable, metallic materials form more-stable phases, such as oxides, hydroxides or sulphides. Under ambient conditions, the most thermodynamically favourable form for most metals, with the exceptions of noble metals, is the oxidised form, which comes about through the reaction of the metal (M) with air, according to Equation (2.9):



The metallic surface is immediately covered by an oxide layer (metal oxide), which prevents to a certain extent direct metal-oxygen contact. For further metal oxidation to occur, one of the reactants, metal or oxygen, must diffuse through the oxide scale. Usually, both phenomena happen simultaneously, although one will be dominant. How rapidly a metal can oxidise is determined by the rate at which ions can diffuse through the oxide scale. The reaction rates for oxide scale growth are low at ambient temperatures under dry conditions, so most metals do not seem to be affected by oxidation. However, as the temperature rises, the reaction rates increase significantly, posing a challenge for metallic materials employed in high-temperature environments. The oxidation behaviour of the metal is influenced by thermodynamics and kinetics, which are discussed in the following sections [54, 65].

2.4.1 Thermodynamics

Thermodynamics predicts if a metal is stable under certain atmospheric conditions, e.g., temperature, atmosphere, etc. The Gibbs free energy of a system can be calculated according

Chapter 2

to Equation (2.10), which helps to determine the stability of the metal or oxide at a constant temperature and pressure.

$$G = H - TS \quad (2.10)$$

where G stands for the Gibbs free energy, H is the enthalpy, T is the temperature, and S is the entropy.

The driving force for reaction depicted by Equation (2.9) is related to the change in Gibbs free energy associated with the conversion of the metal to an oxide. If the change in Gibbs free energy (ΔG) is [54, 65, 66]:

- $\Delta G < 0$, the reaction is spontaneous
- $\Delta G = 0$, the reaction is in equilibrium
- $\Delta G > 0$, the reaction is thermodynamically impossible

Regarding metal oxidation, three phases are essential: the metal, the metal oxide, and the gas phase. To predict if a metal will oxidise, Equation (2.11) can be used:

$$\Delta G = \Delta G^0 + RT \ln \frac{a_{(M_xO_y)(s)}^y}{a_{M(s)}^x \times a_{O_2(g)}^z} \quad (2.11)$$

where ΔG^0 is the change in Gibbs free energy under standard conditions, R is the gas constant, T is the absolute temperature, and a_z is the thermodynamic activity of a species z . The activity for a solid can be approximated to 1, while for a gas, the activity can be assumed to be equivalent to the pO_2 . Thus, the Gibbs free energy at a specific temperature can be expressed as a function of pO_2 , according to Equation (2.12) [54]:

$$\Delta G = \Delta G^0 + RT \ln \frac{1}{pO_2^2} \quad (2.12)$$

As per Equation (2.11), two parameters allow one to determine whether or not a metal or an oxide is stable under certain conditions: temperature (T) and pO_2 . The pO_2 value at which the oxide is in equilibrium with the metal is called the dissociation pressure. For oxidation to occur, the pO_2 in the atmosphere must be higher than the dissociation pressure.

The domains of stability of metal oxides at different temperatures and different partial pressures are shown in the Ellingham diagram (Figure 2.3) [67].

Thermodynamics reveals if the formation of corrosion products is energetically favoured, following the chemical reaction: A (in alloy) + BO \rightarrow AO + B (in alloy). Thermodynamics can be considered as the driving force for the degradation of metals and alloys in corrosive atmospheres. In general, alloys are composed of more than one metal or mixes of a metal and other non-metallic elements (carbon in the case of steels) that are not stable in a reactive gaseous atmosphere [54, 68].

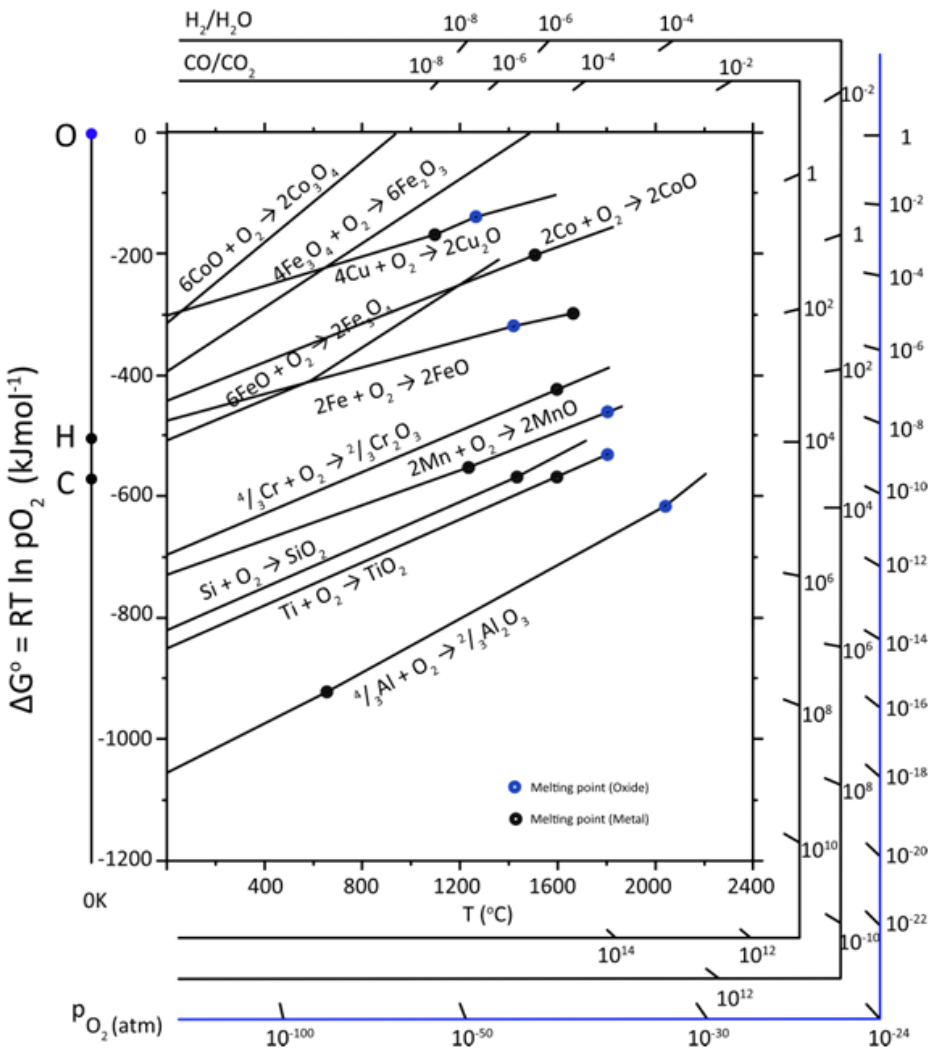


Figure 2.3: Ellingham diagram of the selected oxides. Shown are the standard free energies of formation for selected oxides vs. temperature [67].

2.4.2 Oxide Scale Growth

The growth of an oxide layer follows three distinct steps, as depicted in Figure 2.4. In Step 1, oxygen or water vapour molecules from the atmosphere are adsorbed onto the metal surface, creating a charge transfer, and forming O^{2-} and M^{n+} . In Step 2, the metal oxide nucleates at the metal-gas interface and growth of the metal oxide proceeds until a continuous layer covers the entire surface (Step 3). Steps 1 and 2 depend on the surface orientation, crystal defects on the surface, surface preparation, and impurities in the metal and gas. After the continuous layer has formed, solid-state diffusion through the oxide scale is required for further oxidation [54]. At high temperatures, Steps 1 and 2 happen very rapidly, and Step 3 is often considered to be the rate-determining step for continued scale growth. If the diffusion of ions is the rate-determining step in an oxidation reaction, then the rate of oxidation decreases as the oxide becomes thicker. Such oxide scales, which are distinguished by their high density, low porosity, and low ion diffusivity, are called *protective oxide scales*, e.g., Cr_2O_3 . However, if the oxide scale is porous, then gas transport through the oxide scale becomes easier, resulting in a higher oxidation rate, forming a so-called *non-protective oxide* [54, 69].

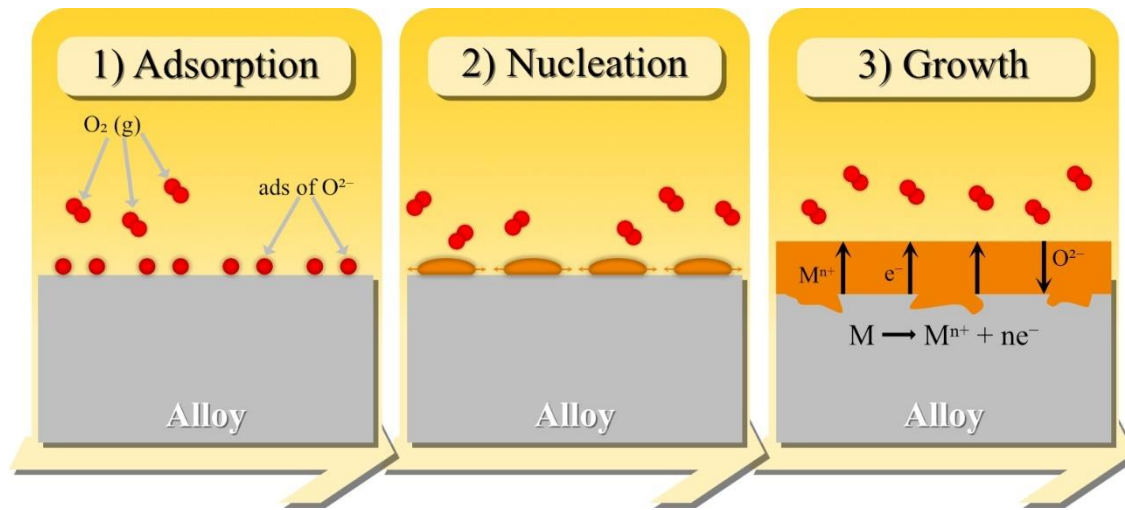


Figure 2.4: Steps in the process of the oxide layer growth on a metal substrate [54]: 1) O_2 adsorption; 2) Oxide nucleation; and 3) Continuous oxide scale growth.

2.4.3 Kinetics

Oxidation kinetics describes the evolution of the oxidation scale over time. It is a critical factor for predicting the life-spans of components exposed to high temperatures. Kinetics analyses are used to understand the reaction mechanism and determine the rate-limiting step of the reaction. There are three different ways to analyse the rate:

- How much metal was consumed
- How much oxygen was consumed; and
- How much oxide was formed

The latter is the most commonly used technique as it is experimentally easy to achieve by measuring the mass gain of the sample. However, this method does not accurately represent the oxidation kinetics in cases of oxide spallation or oxide evaporation. Other methods, such as microscopy and chemical analysis, allow for a more in-depth analysis of oxidation behaviours [54]. To evaluate the kinetics, different rate laws can be formulated. The three most widely used are:

- Linear law
- Logarithmic law
- Parabolic law

The different laws are represented in Figure 2.5. However, not all reactions follow these laws, and deviations from these rate laws or mixtures of different rate laws are common. Nevertheless, the rate laws can provide some information about the protective behaviour of an oxide layer [54, 70].

2.4.3.1 Linear Rate Law

When the mass gain as a function of time is increasing linearly, it can be described according to Equation (2.13):

$$\Delta m = k_l \cdot t + C \quad (2.13)$$

where Δm is the mass change, k_l is the linear rate constant, t is the exposure time, and C is an integer. This behaviour is commonly seen under conditions where surface or phase-boundary processes are the rate-determining steps. This phenomenon is observed if the oxide scale is porous or very thin. Linear mass gain behaviour can also be observed if the thickness of the protective layer is constant [54].

2.4.3.2 Logarithmic Rate Law

When the mass gain as a function of time is behaving logarithmically, it can be described according to Equation (2.14):

$$\Delta m = k_{log} \cdot \log(t + t_0) + C \quad (2.14)$$

where Δm is the mass change, k_{log} is the logarithmic rate constant, t is the exposure time, and C is an integer. The initial oxidation rate is rapid and is followed by a negligible rate. This rate law is observed at low temperatures ($300^\circ - 400^\circ\text{C}$) and for very thin oxide layers (up to 4 nm in thickness). The rate-determining step for this rate law is not yet fully understood. While different hypotheses have been proposed, such as chemisorption and transport of electrons from the metal to the oxide-gas interface due to the electrical field, consensus remains elusive [54].

2.4.3.3 Parabolic Rate Law

Parabolic behaviour is usually associated with Carl Wagner's oxidation model for parabolic rate growth [71]. When the mass gain as a function of the time is parabolic, it can be described using Equation (2.15):

$$\Delta m^2 = k_p \cdot t + C \quad (2.15)$$

where Δm is the mass gain, k_p is the parabolic rate constant, t is the exposure time, and C is an integer. This behaviour is observed when solid-state diffusion transport of the reactants or electrons through the oxide scale (lattice transport) is the rate-determining step. Carl Wagner made the assumptions that:

- The scale is continuous, dense, and well-adherent
- The composition of the oxide is constant throughout the scale
- The scale growth is driven by solid-state diffusion

- Thermodynamic equilibrium exists at the oxide/gas interface and the metal/oxide interface; and
- Oxygen solubility in the metal is negligible

Since the rate-determining step is the diffusion of ions, the oxidation rates of metals that follow the parabolic rate law decrease as the thickness of the oxide increases. The resulting oxide scales are often described as protective oxide scales [54].

2.4.3.4 Breakaway oxidation

Alloys that are designed for high-temperature applications rely on the formation of a compact and well-adherent protective oxide scale that contains elements such as Cr or Al on the alloy surface. The gradual decrease in the amount of such element(s) may eventually lead to failure of the protective oxide scale after prolonged exposure to high temperatures. Breakaway oxidation is frequently observed when a protective oxide scale is transformed into a non-protective oxide scale. There are two main reasons why this happens:

- Mechanically induced chemical failure (MICF)
- Intrinsic chemical failure (InCF)

In the case of MICF, the oxide scale reaches a critical thickness at which the cracking, the rupturing of the oxide, or even spallation leads to direct contact being established between the substrate and the oxygen [54]. Three scenarios may be observed:

- If crack and rupture formation remains below a critical value and the protecting oxide-forming element, e.g., Cr or Al, is not depleted, a continuous protective oxide scale forms (self-healing) [54].
- If the substrate is locally depleted from the protecting oxide-forming element, e.g., Cr or Al, a non-protective, fast-growing Fe-rich oxide forms [54].
- If the rate of crack and rupture formation is high, a non-protective oxide scale can form even if the substrate does not suffer depletion of the protecting oxide-forming elements.

In the case of intrinsic chemical failure, an element that is crucial for the formation of the protective oxide scale in the alloy, such as Cr, is depleted. As a result, thermodynamic conditions become less-favourable for the formation of a protective oxide, potentially leading to the development of a non-protective, rapidly growing oxide, such as an Fe-rich oxide [54, 72].

2.4.3.5 Paralinear oxidation

Chromia-forming alloys that are exposed to an O_2+H_2O environment at high temperatures undergo oxidation and oxide evaporation simultaneously. Oxidation leads to the formation of the oxide scale, while evaporation leads to loss of the oxide scale (see Section 2.4.5). In the

initial stage, the oxide scale growth rate is higher than the oxide scale evaporation rate, resulting in a positive mass gain. As the oxide scale increases in thickness, the oxidation rate decreases. Eventually, the oxide scale growth due to oxidation is equal to the oxide scale lost due to Cr(VI) evaporation. At this point, the critical thickness of the oxide scale is reached [73]. Once the critical thickness is reached, mass loss is observed due to continuous loss of Cr species by evaporation. The combination of parabolic oxidation and linear evaporation is termed *Paralinear oxidation*, as described by Tedmon et al. [73].

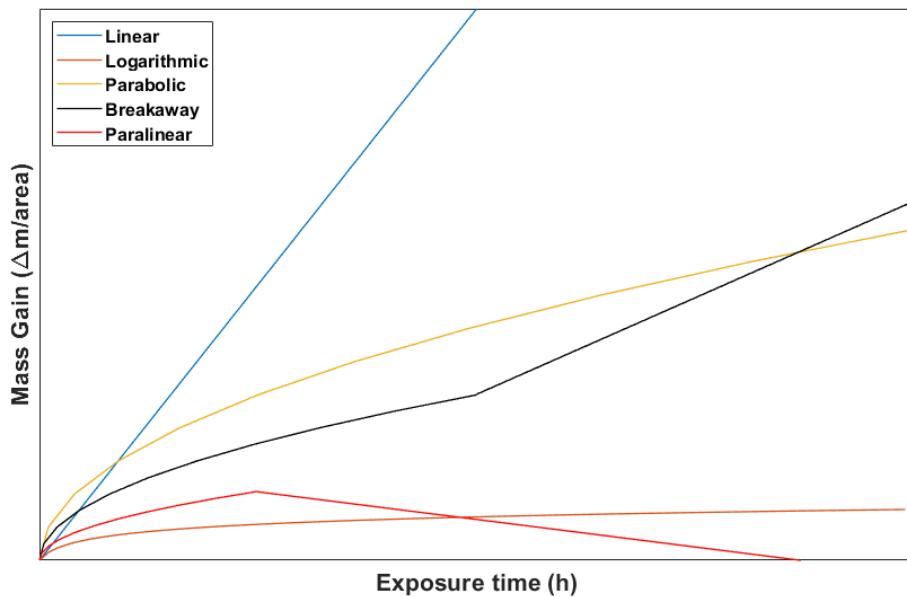


Figure 2.5: Typical metal oxidation kinetics.

2.4.4 Defects in Oxide Scales

The growth mechanism of oxides is highly dependent upon the solid-state diffusion of metal cations, oxygen anions or electrons and electron holes through the oxide scale. Defects must be present in the scale for solid-state diffusion to happen. Even highly stoichiometric oxides, such as Al_2O_3 and Cr_2O_3 , contain defects. Defects can be classified into three different classes:

- Point defects
- Line defects
- Plane defects

Line defects or dislocations are characterised by displacements in the periodic structure in certain directions, while planar defects occur mainly at the grain boundaries or in a stacking fault [54, 74]. Point defects can be divided in two groups:

- Stoichiometric defects (e.g., *Schottky and Frenkel defects*), also called intrinsic defects; and
- Non-stoichiometric defects, also called extrinsic defects (doping of an oxide with another element)

The two most-common intrinsic defects in oxides are Schottky and Frenkel defects, which are depicted in Figure 2.6 for a basic crystal structure, such as the rock-salt structures of NaCl and AgCl, respectively. Schottky defects (Figure 2.6a) constitute a cation vacancy that is charge-compensated by an anion vacancy, whereas Frenkel defects (Figure 2.6b) entail charge compensation of a cation or anion vacancy by an interstitial cation or anion, respectively.

2.4.4.1 Kröger – Vink notation

In a crystal lattice, point defects can occur, such as vacancies (missing atoms), interstitials (extra atoms inserted into the lattice), or substitutions (where one type of atom is replaced by another type of atom). The Kröger – Vink notation provides a concise way to represent these defects and their charge states. The system describes crystals in terms of structural elements, with an imperfection being indicated by a major symbol and the site that it occupies indicated by a subscript [54].

Schottky defect in NaCl:

$$Null = V'_{Na} + V^\bullet_{Cl} \quad (2.16)$$

This notation indicates that a sodium vacancy (V'_{Na}) is formed and a chlorine (V^\bullet_{Cl}) vacancy is created to charge-balance the crystal lattice.

Frenkel defect in AgCl:

$$Ag_{Ag}^X + Cl_{Cl}^X = Ag'_i + V_{Ag}^\bullet + Cl_{Cl}^X \quad (2.17)$$

This notation indicates that a silver interstitial (Ag'_i) is formed due to the displacement of a silver ion, and a chlorine vacancy (V_{Ag}^\bullet) is created. The term Ag_{Ag}^X indicates a neutral silver site.

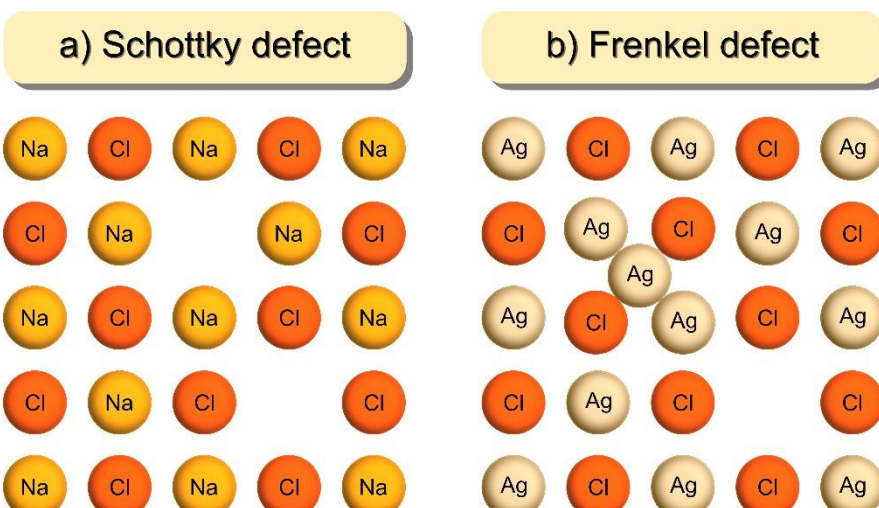


Figure 2.6: Schematic of Schottky and Frenkel point defects common to stoichiometric oxides. The ratio of the ion diameter is not representative of the actual ratio [74].

The structures of the defects depend on the temperature, the pO_2 , and the energy of formation for a specific defect in a lattice [74]. Oxides are classified according to the electrical charge that is transported. If an oxide carries an electrical charge through electrons in the conduction band, it is an n-type oxide. Conversely, if an oxide carries an electrical charge through electron holes in the valence band, it is a p-type oxide [75]. Ions or electrons diffuse through oxide defects, with the diffusion rate being influenced by the specific defect and the exposure temperature. Lattice diffusion, utilising point defects, is the slowest form, while diffusion along grain boundaries, known as *short-circuit diffusion* proceeds considerably faster [48]. The significant activation energy for lattice diffusion and the low activation energy for grain boundary diffusion make the latter more prevalent at lower temperatures and the former more dominant at higher temperatures [48, 63].

Depending on the type of ionic diffusion process occurring in the scale, the direction of oxide growth will be either inwards or outwards. If the diffusion is dominated by oxygen diffusion, the oxide will grow inwards. However, if the diffusion is dominated by metal ion transport, the scale will grow outwards. The different ways in which an oxide can grow are depicted in Figure 2.7. The types of defects in oxide crystals determine the dominant mode of transportation, i.e., anionic or cationic. Depending on their predominant defect, the oxides can be classified in a manner similar to semi-conductors: n-type and p-type. The n-type oxides conduct electrons along the conduction band, and the p-type oxides conduct electron holes along the valence band [76].

- The n-type oxides are divided into two groups:
 - Metal excess oxides, which contain interstitial cations in the lattice, balanced out by electrons in the conduction band. Cations are transported through the lattice by hopping from interstitial sites.
 - Oxygen vacancy oxides, which contain anion vacancies, resulting in positive charges that are compensated by conduction band electrons [54, 69].
- The p-type oxides are also divided into two groups:
 - Oxygen excess oxides, which contain interstitial anions in the lattice that are balanced out by electron holes in the valence band. Excess ions can diffuse through the oxide by changing interstitial sites.
 - Metal vacancy oxides, which contain cation vacancies that result in negative charges, which are compensated by electron holes in the valence band. Ion vacancies can also diffuse in the lattice, leading to conduction of the vacant ions species [54, 69].

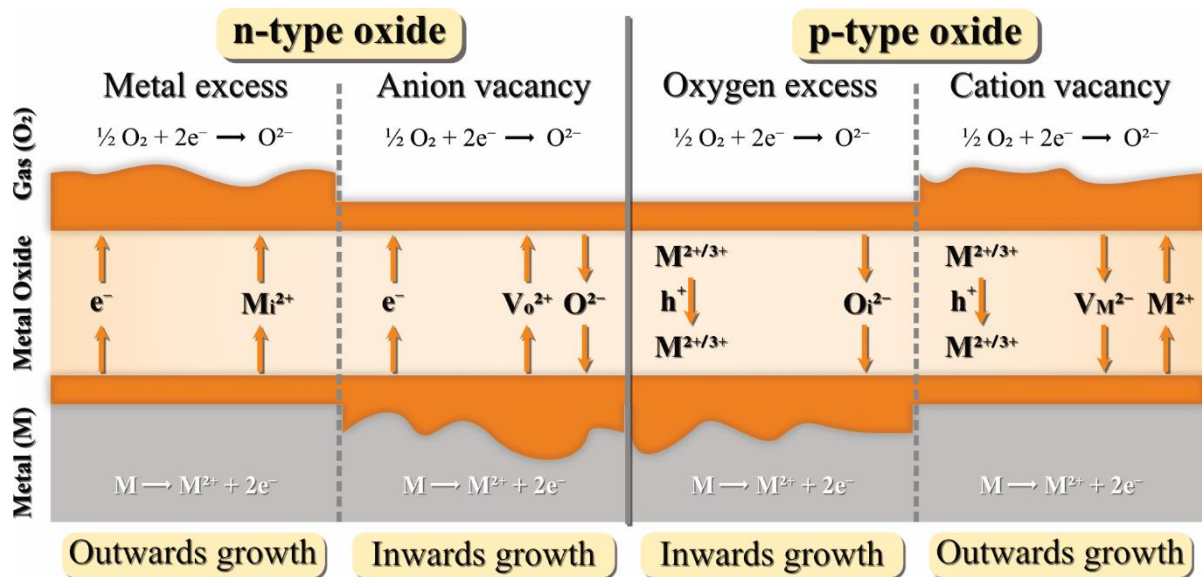


Figure 2.7: Simplified model of diffusion-controlled oxidation in a metal oxide during oxidation. Adapted from [75].

2.4.4.2 Defects in Cr_2O_3

At high $p\text{O}_2$, chromium oxide is a p-type semi-conductor at temperatures below 1,000 °C [63]. All the oxidation experiments in this work were performed at temperatures <1,000 °C, so it is most relevant to consider the defect structure of Cr_2O_3 below this temperature. At lower $p\text{O}_2$, chromia is found to be an n-type semi-conductor [63, 77]. In an oxidation experiment, Cr_2O_3 is subjected to low $p\text{O}_2$ near the metal-oxide interface and high $p\text{O}_2$ at the oxide-gas interface, which will change the dominating defect equilibria.

At low oxygen activities, undoped Cr_2O_3 is dominated by Cr interstitials ($\text{Cr}_i^{\bullet\bullet\bullet}$) and electrons, according to Equation (2.18) [54]:



Meanwhile at higher oxygen activities, Cr vacancies ($V_{\text{Cr}}^{/\!/\!/}$) and electron holes (h^\bullet) are likely to dominate, according to Equation (2.19) [54]:



The concentration of all the defects is dependent upon the $p\text{O}_2$, and a “gradient” of defects is most likely present with the concentration of Cr vacancies being equal to the concentration of Cr interstitials in the mid- $p\text{O}_2$ region [77]. Therefore, in the inner region of the chromia scale, the oxide will have the n-type semi-conductor behaviour, while towards the outer part of the oxide scale, it will gradually change to the p-type behaviour [54].

However, the above observations refer to undoped chromia. It seems unlikely that pure Cr₂O₃ will form on a Cr₂O₃-forming alloy at high temperatures, and various elements from the alloy may dissolve in the Cr₂O₃ scale. The addition of a dopant (such as Mn, Ti or Fe) will affect the types of defects present in the Cr₂O₃ scale. A low valent dopant (such as Mn) will increase the hole concentration at high *p*O₂, whereas a higher valent dopant (such as Ti) will increase the concentration of electrons or Cr vacancies at both low and high *p*O₂ values [78]. Extrinsic impurities play an important role in the defect-structure of Cr₂O₃, thereby affecting its electrical conductivity under a specific atmosphere.

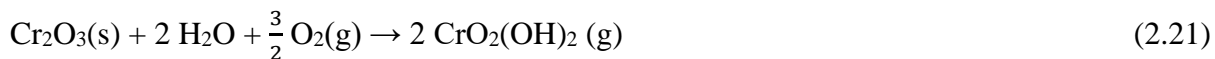
2.4.5 Chromium Species Evaporation

Some oxides, such as Cr₂O₃, WO₃ and MoO₃, react with their environment to form volatile metal oxide species [54, 79]. This phenomenon leads to a higher rate of consumption of the protective oxide-forming element in the alloy, possibly leading to catastrophic corrosion and breakaway oxidation. Cr-containing alloys form a protective, slow-growing, and dense Cr₂O₃ layer when exposed to high temperatures. However, Cr evaporation, which has been extensively studied [80-83], limits the use of Cr₂O₃-forming alloys at high temperatures. Moreover, Cr evaporation causes poisoning of the cathode in SOFCs. Under certain atmospheres, specific volatile Cr species may be formed. In a dry atmosphere, gaseous CrO₃ will be formed according to Equation (2.20):



The requirements for such an oxide to evaporate are: high temperature (*T* ≈ 1,000 °C); and high *p*O₂ [54].

Another volatile Cr species, CrO₂(OH)₂, will form in water vapour-containing atmospheres. Several authors [84, 85] have shown that CrO₂(OH)₂ is the most-abundant volatile Cr species in air when water vapour is present. CrO₂(OH)₂ is formed according to Equation (2.21):



Since CrO₂(OH)₂ has a low activation energy, it will form at lower temperatures than CrO₃, which has a higher activation energy and is more temperature dependent [86].

Furthermore, the rate of Cr(VI) evaporation is dependent upon the gas flow. Figure 2.8 shows the effect of the gas flow on the Cr(VI) evaporation of a 21 wt% Cr FSS (Sanergy HT) exposed at 850 °C in air that contains 3 % H₂O vapour. At low flow rates, the rate of Cr(VI) evaporation is proportional to the flow rate, whereas a plateau appears at a higher flow rate (~6,000 sml·min⁻¹). In this range, the Cr(VI) evaporation is independent of the airflow rate [87].

In the present work, the dominating Cr-species evaluated is CrO₂(OH)₂. In **Papers I** and **II**, the samples were exposed in humid air at between 600 ° – 650 °C. In **Papers II–V**, the samples

were exposed to dual-atmosphere conditions, with humid atmospheres on both sides.

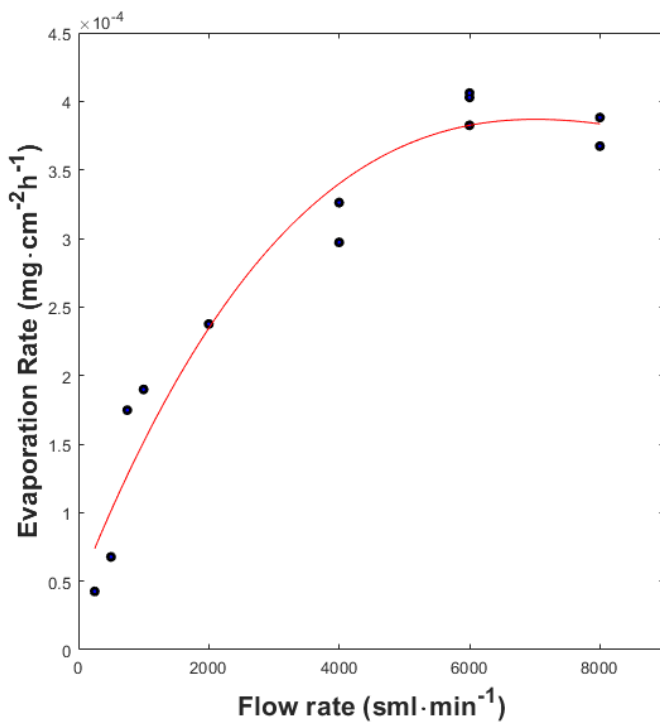


Figure 2.8: Rate of Cr vaporisation as a function of gas flow rate at 850 °C in air + 3 % H₂O on Sanergy HT substrate. Data used with permission from [87].

3. Corrosion of metallic interconnects

[...] Nature, in conformity with her usual benevolence, has limited the power of iron, by inflicting upon it the punishment of rust [...]”

– Pliny the Elder

Interconnects are an essential part of every FC, as they electrically connect the cells within a stack. When exposed to high temperatures ($600^{\circ} - 900^{\circ}\text{C}$), the metallic materials are expected to form a passive oxide layer, i.e., SiO_2 , Al_2O_3 or Cr_2O_3 , which protects them from rapid corrosion. The metallic materials used must have good resistances to high-temperature corrosion and be good electronic conductors, although constraints such as the design, applications and cost also play major role in the selection of materials. While alloys that form either an SiO_2 layer or an Al_2O_3 layer would be the best candidates because of their well-adherent and dense oxides, their insulating properties exclude them from being used. On the other hand, Cr-containing alloys form a protective, dense Cr_2O_3 scale that is a much better electronic conductor. Most researchers are, therefore, focusing on chromia-forming steels, which are also called stainless steels. However, Cr_2O_3 -forming alloys suffer from Cr evaporation, which leads to cathode poisoning. These stainless steels are classified according to crystalline structure. Research has focused mainly on two crystalline structures [88]:

- Ferritic stainless steels , which have a crystalline body-centred cubic (BCC) structure (Figure 3.1a); and
- Austenitic stainless steels, which have a crystalline, face-centred cubic (FCC) structure (Figure 3.1b)

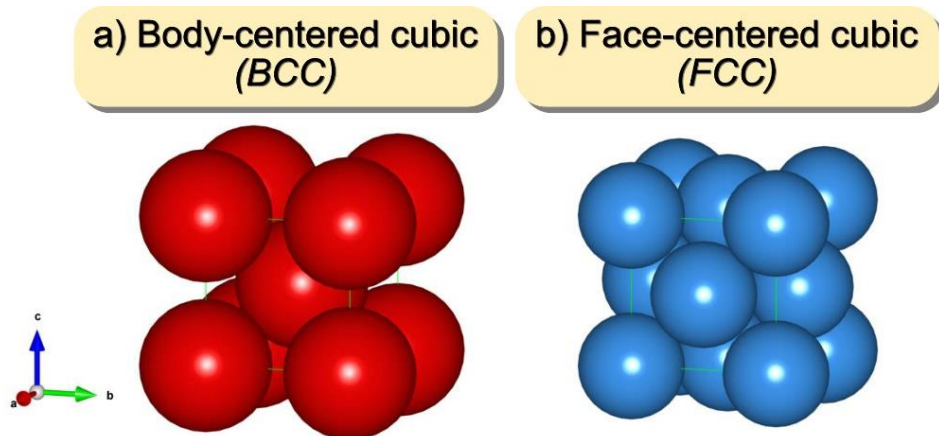


Figure 3.1: Space-filling representation of; a) body-centred cubic; and b) faced-centred cubic crystalline structures.

Nowadays, state-of-the-art interconnects materials are FSS. Yet, the interconnects deteriorate over time due to the harsh conditions experienced during FC operation.

3.1 Ferritic Stainless Steels as Interconnects

Currently, alloys such as Fe-Cr-containing alloys are the materials in focus for SOFC interconnects. Steels have a wide range of alloying elements available to achieve specific properties depending on the application. FSS contain at least 10 % Cr and are the materials of choice for high-temperature applications. To ensure the ferritic structure at all temperatures, the Cr content has to be 13 % (see Figure 3.2). The most-common choice for an interconnect material is FSS due to its TEC, which lies between $11.5 \cdot 10^{-6} \text{ K}^{-1}$ and $14 \cdot 10^{-6} \text{ K}^{-1}$ for ferrites and between $18 \cdot 10^{-6} \text{ K}^{-1}$ and $20 \cdot 10^{-6} \text{ K}^{-1}$ for austenites [49, 64], matching more closely the other cell components ($\text{TEC}_{\text{SOFC}} = 10.5 \cdot 10^{-6} \text{ K}^{-1}$ to $12.5 \cdot 10^{-6} \text{ K}^{-1}$ [64]). The most-suitable FSS are steels that contain more than 16 at% Cr. A higher Cr content in the alloy is detrimental, as it allows for the formation of a brittle σ -phase [89].

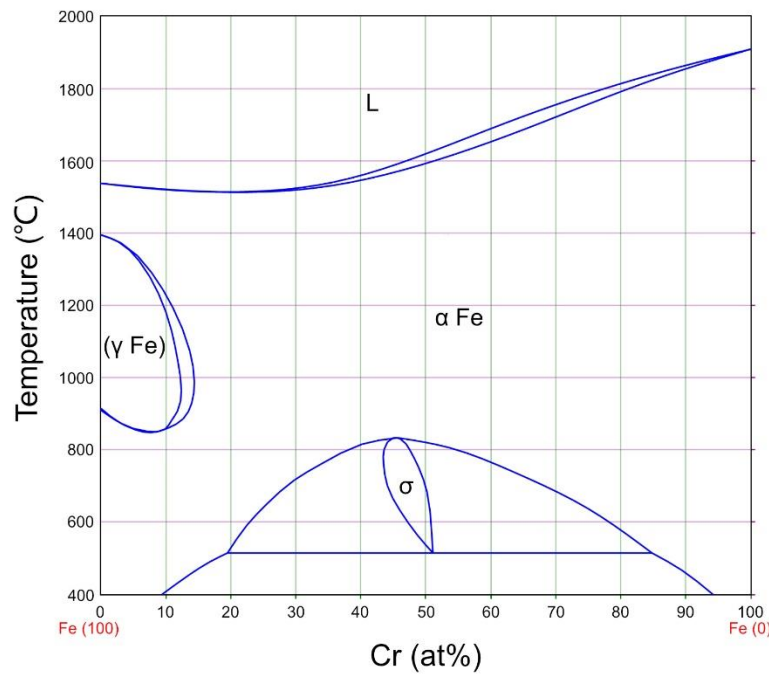


Figure 3.2: Binary Fe-Cr phase diagram, adapted from [90]. α -Fe has a BCC crystalline structure, i.e., ferritic phase, and γ -Fe has an FCC crystalline structure, i.e., austenitic phase.

3.1.1 Material Selection

FSS are associated with challenges regarding their life-times. Cr evaporation (see Section 2.4.5) is a major issue for an FC stack. Apart from the continuous consumption of Cr, which can lead to Cr depletion, the evaporation of the hexavalent gaseous Cr species Cr(VI) [see Equation (2.19)] may poison the cathode by blocking the TPB, thereby reducing FC performance [91]. A second major issue related to Cr is the growth of a chromia scale over

time, which leads to a gradual increase in the electrical resistance of the interconnect. These two main corrosion issues have been studied extensively. However, other degradation mechanisms exist, one of which is the dual-atmosphere environment to which the interconnect is exposed, inducing breakaway oxidation.

Specific alloys have been developed to be used as interconnects, such as Crofer 22 APU, Crofer 22 H, and Sanergy HT. These alloys have a Cr-content of at least 21 % and other alloying elements such as Mn and REs, both of which are added to mitigate the afore-mentioned problems. These alloys are specifically designed to be used as interconnects in FCs, so they are relatively expensive. Therefore, cheaper materials are being investigated, for example, AISI 441 and AISI 430 with Cr-contents in the range of 16 % – 20 % [92-95]. These alloys are highly suitable for IT-SOFC operating temperatures (around 600 ° – 700 °C) because at higher temperatures, the Cr-content might not be sufficient [96]. Minor alloying elements, such as Mn, Ti or Ce, can have strong positive effects on the steel properties.

3.1.2 Alloying elements

Alloying elements are intentionally added to improve the properties of the steel or are remnants from the steel-making process but that are too expensive to remove. The most-common alloying elements and their benefits are discussed below.

3.1.2.1 *Chromium*

Chromium is widely added as an alloying element to improve the corrosion properties of alloys. Adding Cr to alloys significantly enhances their corrosion resistance. The high reactivity of Cr is crucial for its effectiveness as an alloying element in stainless steels. The abilities of these alloys to withstand the chemical effects of corrosive agents rely on their capacities to form a protective Cr_2O_3 film, which shields the metal substrate from both uniform and localised attacks. For a continuous Cr_2O_3 layer to form and persist, it is commonly suggested that the Fe-Cr alloy must contain a minimum Cr content of around 10 wt% although this depends on experimental conditions; below this threshold, internal oxidation of Cr is more likely, as described by Wagner [97]. As the Cr content increases, the corrosion resistance of Fe-Cr alloys generally improve as an external Cr_2O_3 layer is formed [98, 99].

3.1.2.2 *Manganese*

Two significant issues arise during FC operation, which are due to Cr evaporating from the interconnect:

- Cr-deficiency in the interconnect; and
- Cr-poisoning of the cathode

Adding small amounts of manganese (up to 0.5 wt%) as an alloying element results in the formation of a $(\text{Cr}, \text{Mn})_3\text{O}_4$ top layer with a continuously growing Cr_2O_3 layer underneath [80,

88]. It has been shown that the addition of Mn helps to reduce Cr(VI) evaporation by a factor of 2–3 [80, 81]. However, in the long-run for an SOFC system, the level of Cr evaporation remains high and different mitigation methods must be used.

3.1.2.3 Silicon and Aluminium

Silicon (Si) and aluminium (Al) are commonly present in stainless steels due to the manufacturing process, in which they are used as oxygen traps (de-oxidation) [100]. Due to their high affinities for oxygen and low concentrations, Si and Al oxidise internally underneath the chromia scale. However, when there is formation of a continuous Si- or Al-oxide sub-layer, this is detrimental to the properties of the steel, as SiO_2 and Al_2O_3 are known to be electrical insulators [60, 101]. It has been reported that a SiO_2 sub-scale reduces the adhesion of the oxide scale to the metal, due to the TEC mismatch between the oxide and the alloy, and this causes the Cr_2O_3 layer to spall off during thermal cycling [19, 102]. Therefore, alloys that are specifically designed to be used as interconnects either employ a specific vacuum induction melting process to avoid Si contamination or add other alloying elements to bind Si. Crofer 22 APU employs the first method, while Crofer 22 H and Sanergy HT apply the latter solution. For the latter technique, alloying elements such as Nb, W or Mo are added. Their effects are discussed in the next section.

3.1.2.4 Titanium

The presence of Ti in the alloy will result in internal oxidation. This phenomenon can have a beneficial effect, as the internal oxide zone can strengthen the near-oxide scale area and prevent the oxide scale from buckling [78]. Ti is added to the steel to increase the stability of the ferrite structure at high temperatures. Ti increases the conductivity of the oxide scale due to doping, which also increases the rate of Cr diffusion, resulting in a higher growth rate of the chromia scale [103]. A too-high concentration of titanium could lead to spallation of the scale [78].

3.1.2.5 Other alloying elements (Nb, Mo or W)

Nb, Mo or W are added to the melt to form Laves phases such as $(\text{Fe,Cr})_2(\text{Nb,W,Mo})$, to bind Si and hinder the formation of an insulating SiO_2 layer [104]. Laves phases have the positive side-effect of increasing the creep strength of the steel [105, 106]. A high concentration of Nb can have a detrimental effect, as it increases the oxidation rate of the steel due to doping of the Cr_2O_3 scale [107].

3.1.2.6 Reactive elements (Ce, Hf, La, and Y)

Leonard Bessemer Pfeil discovered in the late 1930s that adding a small quantity of rare-earth elements, such as Y, Sc, Ce or La, to Cr_2O_3 -forming alloys improved dramatically the oxidation resistance of the alloys [108]. The addition of elements belonging to the rare-earth

element group, such as Ce, Hf, La, and Y, and their beneficial effects on the oxidation properties of the alloys are well-established in the literature [109-112]. Those elements are referred to as Reactive Elements (REs) and the effect is termed the RE effect. The most-common effects manifested by the REs are to:

- Increase oxide-scale adhesion and resistance to spallation;
- Decrease oxide scale growth;
- Modify the growth mechanism of the oxide scale; and
- Promote selective oxidation of the alloy

These effects are evident for small additions (0.01 – 0.5 wt%) [113]. However, the mechanism through which REs work are not yet fully understood. Nevertheless, researchers are in agreement that the addition of REs changes the growth mechanism of the oxide scale. The most-common theory suggests that undoped Cr_2O_3 growth is due to the predominant metal outward diffusion. However, when the Cr_2O_3 scale is doped with REs, the outward diffusion of the metal cations is inhibited by the segregation of REs at the grain boundaries. Consequently, the small flux of oxygen ions becomes the predominant mechanism. The growth mechanism shifts from predominantly outward diffusion of Cr ions to predominantly inward diffusion of oxygen ions, thereby slowing oxide scale growth and improving oxide scale adhesion [109-112]. Reactive elements prevent the detrimental effect of sulphur on the alloy by trapping the sulphur impurity, preventing it from segregating to the metal–oxide interface so as to weaken the inter-facial bonding [114, 115].

Specifically designed commercial alloys, such as Crofer 22 H, Crofer 22 APU, and ZMG™ 232, undergo incorporation of REs during the manufacturing process. However, this increases the overall production cost. An alternative way of adding REs is by applying coatings [92, 116]. Although coatings that contain REs improve the oxidation resistance of the steel, the rate of Cr evaporation is not reduced. Therefore, RE coatings must be combined with a second coating, which mitigates Cr evaporation, such as the Mn-Co oxide coating (MCO) or metallic Co [117, 118].

3.2 Coatings to Mitigate Cr(VI) Evaporation

Improvements in steel chemistry have proven effective to a certain extent in reducing Cr(VI) evaporation, although high oxidation rates are still a limiting factor when it comes to using uncoated FSS as interconnect materials. The expected life-time for an SOFC system is in the range of 40,000 – 80,000 h [15, 16]. Two main mechanisms can lead to the degradation of a FC over a long life-time:

- Cr poisoning of the cathode due to Cr(VI) evaporation; and
- Increased electrical resistance due to the continuously growing Cr_2O_3 scale

Incorporating additional alloying elements into the steel has only a limited effect on these degradation mechanisms. Therefore, additional protection is needed. Nowadays, coatings are the norm in terms of improving oxidation resistance. Certain coatings have been proven to be effective at reducing Cr(VI) evaporation and chromia scale growth [119, 120]. Coatings must respect the same criteria as for the interconnects, i.e., TECs similar to those of the other cell components, good electrical conductivities, ease of manufacturing, chemical compatibility with adjacent components, good adhesion to the substrate, and low cost. Several studies have investigated coating compositions, deposition techniques, and their constituent elements. Most of the coatings that have been developed for interconnect applications can be divided into two groups: Perovskite-type and Spinel-type coatings.

3.2.1 Perovskite-type coating

The general formula for perovskite is ABO_3 , where the A sites are occupied by low-valence cations such as La, Sr, Ca and Pb, and the B sites are occupied by higher-valence transition metal cations such as Ti, Co, Fe etc. (Figure 3.3a). Perovskite coatings exhibit p-type behaviours under oxidising conditions and are stable at low $p\text{O}_2$ [18, 121]. Research in this area has focused mainly on lanthanum chromite (LaCrO_3), lanthanum strontium chromate ($\text{La}_{1-x}\text{Sr}_x\text{CrO}_3$), lanthanum strontium manganate ($\text{La}_{1-x}\text{Sr}_x\text{MnO}_3$), lanthanum strontium cobaltite ($\text{La}_{1-x}\text{Sr}_x\text{CoO}_3$), and lanthanum strontium ferrite ($\text{La}_{1-x}\text{Sr}_x\text{FeO}_3$). They possess high electrical conductivity and strong compatibility with the other cell parts [122]. However, a thick coating is commonly required to decrease significantly the oxidation rate, and adhesion of the coating to the substrate is often poor. In addition, the mitigation of Cr evaporation by a perovskite-type coating is limited [18, 81].

3.2.2 Spinel-type coating

The general formula for a spinel is AB_2O_4 , where A and B are usually divalent, and trivalent cations occupying the octahedral and tetrahedral sites in the FCC oxygen anion lattice (see Figure 3.3b) [120]. By adjusting the chemical composition (ratio of A to B cations), the spinel properties, such as thermal and electrical conductivities, can be adapted to a specific application [123]. Spinel coatings are of interest because of their high efficiency in mitigating Cr evaporation. The spinel coating $(\text{Co},\text{Mn})_3\text{O}_4$ (MCO) offers good Cr retention and high electrical conductivity [123-127]. The conductivity of the MCO coating is in the range of $6.4 - 60 \text{ S}\cdot\text{cm}^{-1}$ at 800°C , and it has a TEC in the range of $11.5 - 14.4\cdot10^{-6} \text{ K}^{-1}$ in the temperature range of $25^\circ - 800^\circ\text{C}$ [123]. Several studies [119, 120, 128] have attempted to enhance the conductivity of the MCO coating by doping it with Co, Cu and Fe. This coating can be applied to the steel using different techniques, such as spray drying, dip-coating, screen printing, aerosol spray deposition, plasma spraying, and physical vapour deposition (PVD).

Besides applying the oxide coating directly, a conversion coating route can also be utilised [127]. For this technique, the alloy is coated with a metal, such as Co or Cu, which is then oxidised at high temperature to form the corresponding metal oxide. As an example, to achieve

MCO coating via the conversion coating route, Co is first oxidised to Co_3O_4 and then enriched with Mn through outward diffusion of Mn from the steel substrate [92, 127]. The advantages of conversion coatings are that thin and dense coatings can be achieved. The process is highly cost-effective because large-scale, roll-to-roll coating applications are possible [129]. It has been shown that REs can also be used as coating materials, since they decrease the oxide scale growth rate and improve scale adherence [110, 130]. Ce/Co coating combines the positive effects of both coatings, MCO conversion coatings, and RE coatings. Currently, a 10-nm-thick Ce coating beneath a 600-nm-thick Co coating is considered to be the state-of-the-art coating [118, 131, 132].

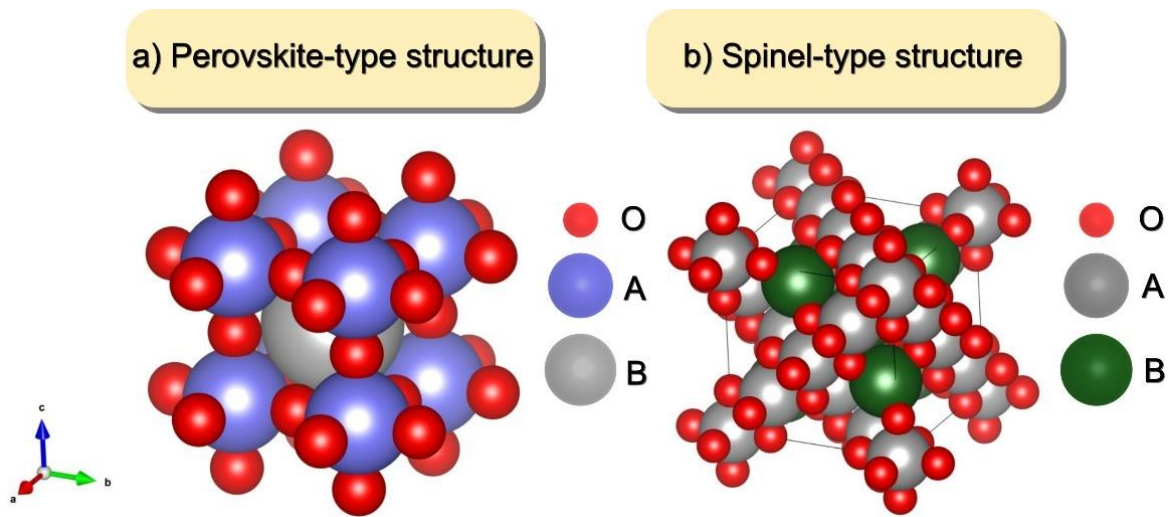


Figure 3.3: Space-filling representation of: a) a Perovskite-type structure; and b) a Spinel-type structure.

3.3 Electrical Conductivity of Oxide Scales

The main role of an interconnect is to connect electrically the cells within an FC stack. The growth of an oxide scale during high-temperature operation drastically increases the overall resistance. The electrical conductivity of the oxide is several orders of magnitude lower than that of the steel. Therefore, growth of the oxide scale is reducing the efficiency of the FC. To describe the electrical conductivity of an oxide, the sum of the conductivities of the electronic and ionic charge carriers is calculated according to Equation (3.1):

$$\sigma_{total} = \sigma_{ionic} + \sigma_{electronic} \quad (3.1)$$

where σ_{total} is the electrical conductivity, and $\sigma_{electronic}$ and σ_{ionic} are the respective conductivities, which are defined in Equations (3.2) and (3.3), respectively [54].

$$\sigma_{electronic} = \sigma_e + \sigma_h = e(nv_e + pv_h) \quad (3.2)$$

where $\sigma_{electronic}$ is defined as the sum of the conductivity of the electrons σ_e and holes σ_h , n and p are the concentrations of electrons and holes, respectively, and v_e and v_h are the mobilities of the electrons and holes, respectively [54]. By the same reasoning, σ_{ionic} is the sum of the anion and cation conductivities according to Equation (3.3):

$$\sigma_{ionic} = \sigma_a + \sigma_c \quad (3.3)$$

Both the mobility and the concentration terms are temperature-dependent. In oxides, the increased charge carrier concentration and increased mobility of the ions supersede the decreased mobility of the electrons. This leads to a positive temperature dependency for the oxide. However, in metals, the decreased mobility of electrons supersedes the increased charge carrier concentration, resulting in a negative effect on metallic conductors, such that the conductivity decreases with increasing temperature. Oxides that exhibit this phenomenon, such as Cr₂O₃ or Co₃O₄, are classified as semi-conductors [54]. The temperature-dependence of the conductivity of oxide scales can also be expressed using the Arrhenius Equation (3.4):

$$\sigma = \sigma_0 \cdot \exp\left(\frac{-E_a}{R \cdot T}\right) \quad (3.4)$$

where σ_0 is a pre-exponential factor, R is the ideal gas constant, T is the absolute temperature, and E_a is the activation energy.

Owing to the complexity of the oxide scales, the overall resistance is measured, which is commonly expressed as the Area-Specific Resistance (ASR) and can be described according to the Equation (3.5):

$$ASR = R \cdot A \quad (3.5)$$

where R is the resistance, and A is the area. R can also be expressed according to Equation (3.6):

$$R = \frac{1}{\sigma} \cdot \frac{L}{A} \quad (3.6)$$

where σ is the conductivity, L is the oxide thickness, and A is the area.

3.3.1 Intrinsic semi-conductors

A semi-conductor is said to be intrinsic if most of its free charge carriers, i.e., electrons and holes, originate from the semi-conductor atoms themselves. If an electron receives sufficient thermal energy to jump from the valence band to the conduction band, it leaves a hole in the valence band. Thus, every hole in the valence band corresponds to an electron in the conduction band and vice versa. When the temperature increases, more electrons gather sufficient energy to leave the semi-conductor atoms and become free to move in the conduction band. These are called *free electrons*, and they can move freely in the crystal to contribute to the overall electrical current. An equal number of free holes can move freely in the crystal and contribute to the current. The conductivity of a material is directly dependent upon the number of charge carriers (i.e., free electrons and holes) that it contains. The larger the quantity, the higher the conductivity. Thus, the conductivity of a semi-conductor is temperature-dependent [133, 134].

3.3.2 Extrinsic semi-conductors

A semi-conductor is said to be extrinsic when the intrinsic, i.e., intrinsic semi-conductor, material that forms its basis has been “doped” by introducing a minor amount of impurities. An extrinsic semi-conductor has a higher conductivity than its intrinsic form. In an extrinsic semi-conductor, the electron density or the hole density is higher than in the corresponding intrinsic material [133, 134]. There are two types of extrinsic semi-conductors, as described in Section 2.4.4.

3.3.3 Electrical conductivity of chromia

Since interconnects are mainly made of FSS, the electrical properties of the growing chromia scale have a major impact on the overall conductivity of the interconnect. Cr_2O_3 is known to be an intrinsic semi-conductor at high temperatures ($> 1,000 \text{ }^\circ\text{C}$). However, it exhibits an extrinsic semi-conductor behaviour below this temperature and relies mainly on dopants [63, 135]. At temperatures lower than $1,000 \text{ }^\circ\text{C}$, chromia is a p-type semi-conductor, and its conductivity depends on the $p\text{O}_2$ and is dominated by dopants and impurities [63]. Even though the primary doping mechanism for Cr_2O_3 is unclear, it has been shown to have a dual semi-conductor behaviour, with an n-type and p-type semiconducting behaviour depending on the type of defects present [136]. Researchers [136, 137] have attributed this dual semiconducting behaviour to the presence of an n-type internal subscale and n-type or p-type outer scale above $800 \text{ }^\circ\text{C}$, depending on the $p\text{O}_2$. The thermally grown Cr_2O_3 is doped with several elements, such as Ti, Ni, Fe, Mn and Nb, present in the steel [63, 78, 138], usually improving its electrical conductivity. The electrical conductivity of chromia varies between $0.001 \text{ S}\cdot\text{cm}^{-1}$ and $0.05 \text{ S}\cdot\text{cm}^{-1}$ at $800 \text{ }^\circ\text{C}$ [43, 63, 139-141].

3.3.4 Electrical conductivity of spinels

As stated in Section 3.2, spinels are the primary coatings used in interconnects to reduce Cr(VI) evaporation. Therefore, it is crucial to understand the electrical properties of the various spinels that have been proposed as interconnect coating systems. It is commonly believed that electrons jump from one octahedral site to another, and that if cations of mixed-valence occupy the sites, electrical conductivity is enhanced [123, 142]. The $(\text{Cr},\text{Mn})_3\text{O}_4$ spinel has a higher conductivity than Cr_2O_3 , whereas it has a much lower conductivity than $(\text{Co},\text{Mn})_3\text{O}_4$ spinel. This explains why Cr-containing spinels often exhibit high resistance, since in the spinel structure, the only possible valence of Cr is Cr^{3+} , which tends to occupy the octahedral sites [143]. Petric et al. [123] have conducted an extensive study of the conductivity of different spinels and discovered that spinels that contain Mn, Co, and Cu have the highest conductivities. However, spinels that contain Cr exhibit very low conductivities, which is in accordance with the previous statement. A recent study [55] has shown that highly conductive spinel coatings have a minimal negligible effect on the ASR, as the electrical conductivity of the thermally grown chromia scale is orders of magnitude lower, making it the main contributor to the overall resistance.

Table 3.1: Specific conductivity values (in S·cm⁻¹) for the different spinels measured at 800 °C, except where noted. Data are taken from [123].

	Mg	Mn	Co	Ni	Cu	Zn
Al	MgAl ₂ O ₄ $\sigma = 10^{-6}$	MnAl ₂ O ₄ $\sigma = 10^{-3}$	CoAl ₂ O ₄ $\sigma = 10^{-5}$	NiAl ₂ O ₄ $\sigma = 10^{-4}$	CuAl ₂ O ₄ $\sigma = 0.05$	ZnAl ₂ O ₄ $\sigma = 10^{-6}$
Cr	MgCr ₂ O ₄ $\sigma = 0.02$	Mn_{1.2}Cr_{1.8}O₄ $\sigma = 0.02$	CoCr ₂ O ₄ $\sigma = 7.4$	NiCr ₂ O ₄ $\sigma = 0.73$	CuCr ₂ O ₄ $\sigma = 0.40$	ZnCr ₂ O ₄ $\sigma = 0.01$
Mn	MgMn ₂ O ₄ $\sigma = 0.97$	Mn ₃ O ₄ $\sigma = 0.10$	CoMn ₂ O ₄ $\sigma = 6.4$	NiMn ₂ O ₄ $\sigma = 1.4$	Cu_{1.3}Mn_{1.7}O₄ $\sigma = 225$ (750 °C)	ZnMn ₂ O ₄
Fe	MgFe ₂ O ₄ $\sigma = 0.08$	MnFe ₂ O ₄ $\sigma = 8.0$	CoFe ₂ O ₄ $\sigma = 0.93$	NiFe ₂ O ₄ $\sigma = 0.26$	CuFe ₂ O ₄ $\sigma = 9.1$	ZnFe ₂ O ₄ $\sigma = 0.07$
Co		MnCo₂O₄ $\sigma = 60$	Co₃O₄ $\sigma = 6.7$			

3.4 The Dual-Atmosphere Effect

To date, research on corrosion phenomena has focused primarily on simplified conditions (i.e., single-atmosphere conditions either in air or fuel). However, interconnects in SOFCs are exposed to dual-atmosphere conditions, with low and high pO_2 on either side. One side of the interconnect is exposed to air (air-side), while the other side is exposed to H₂ (fuel-side) (Figure 3.4). The influence of the dual-atmosphere effect on FSS interconnects has been studied by several groups in the past decades [20, 21, 94, 95, 144-148]. Different observations have been reported in the literature: from increased corrosion on the air-side of the sample on the one hand, to no observed detrimental effect on the other hand.

The effect of hydrogen is still unclear, and many discrepancies exist in the literature. Previous research, conducted at temperatures around and above 800 °C [149, 150] found no evidence of significant breakaway oxidation on samples that were exposed under dual-atmosphere conditions. Ardigo et al. [149] did not find Fe in the oxide scales after 100 h of exposure at 800 °C in an O₂-H₂O atmosphere; instead, they observed a (Cr,Mn)₃O₄ spinel on top of a chromia scale. Kurokawa et al. [151] detected small quantities of Fe in the scale, but did not observe breakaway corrosion. Skilbred et al. [148] have reported minor changes to the oxide scale, without any change to the structure. Conversely, Gunduz et al. [21] have reported a severe dual-atmosphere effect at 800 °C on non-pre-oxidised AISI 411, although they found no increased corrosion on pre-oxidised AISI 411 samples at 800 °C. Yang et al. [152, 153] have shown detrimental effects of dual-atmosphere conditions on the air-side of an FSS sample exposed at 800 °C. They have demonstrated the formation of an Fe-rich oxides on the air-sides of AISI 430 and Crofer 22 APU, with significant changes in oxide thickness, which were not observed upon simple air exposures. Similar observations have been reported by Gannon et al. [154] for AISI 441 exposed at 800 °C under dual-atmosphere conditions. The discrepancies in the literature regarding the intensity of the corrosion induced by dual-atmosphere conditions

reflect differences in sample preparation and exposure conditions, i.e., surface conditions, heat treatment, hydrogen concentrations, humidity, etc., especially on the fuel-side.

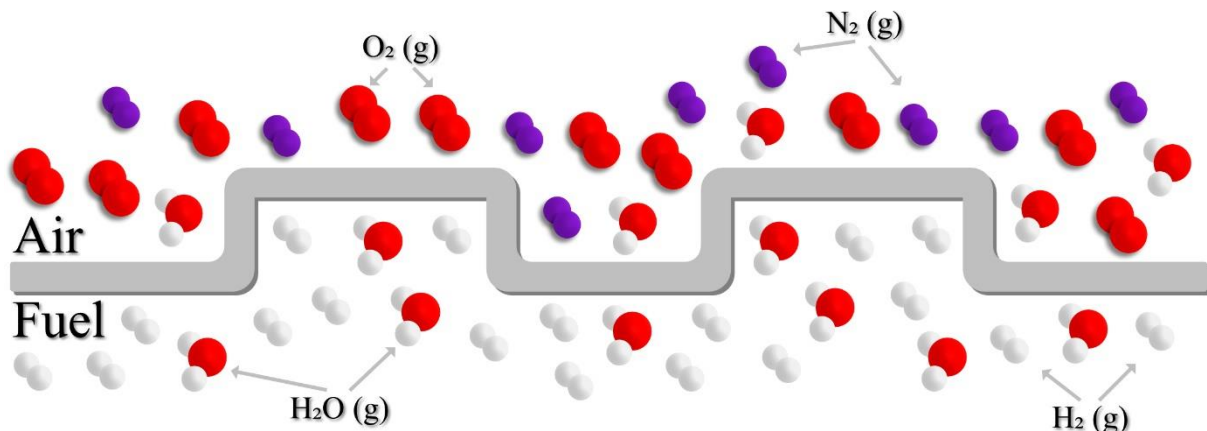


Figure 3.4: Schematic of an interconnect exposed under dual-atmosphere conditions. The ratio of the atom diameter is not representative of the actual ratio.

Most of the studies discussed above were performed at temperatures $\geq 800\text{ }^{\circ}\text{C}$. In the past decade, the trend has been to lower the SOFC operating temperature, which means that more research on SOFCs needs to be carried out in the temperature range of $600\text{ }^{\circ}\text{--}800\text{ }^{\circ}\text{C}$. Moreover, the availability of cheaper materials could lead to cost reductions. However, recent research has shown that the dual-atmosphere effect is more severe at lower temperatures. Alnegren et al. [20, 147] have shown a clear dual-atmosphere effect on pre-oxidised samples exposed at $600\text{ }^{\circ}\text{C}$. The samples were covered with Fe-rich nodules, while samples exposed at higher temperatures were protective. Young et al. [155] have reported higher levels of corrosion at lower temperatures, i.e., $500\text{ }^{\circ}\text{C}$ and $600\text{ }^{\circ}\text{C}$, than at higher temperatures ($650\text{ }^{\circ}\text{C}$ to $800\text{ }^{\circ}\text{C}$) in an anode atmosphere. Other groups, such as Nakagawa et al. [156], have described a dramatic increase in the corrosion rates of the FSS on the air-sides of the samples exposed under dual steam/air conditions at $600\text{ }^{\circ}\text{C}$. Niewolak et al. [88] have described the formation of Fe-based oxide scales on austenitic stainless steels at $600\text{ }^{\circ}\text{C}$ in a simulated anode atmosphere. These results indicate an inverse temperature effect, described by Alnegren et al. [26], i.e., a more-pronounced effect is observed at lower temperatures than at high temperatures. They have suggested that the inverse temperature effect is due to a reduction in Cr diffusion in the steel, which causes a decrease in the amount of Cr at the metal/oxide interface and leads to the formation of breakaway oxidation. Reisert et al. [144] have observed accelerated corrosion due to the dual-atmosphere effect on both chromia-forming and alumina-forming alloys, as well as a reverse temperature effect with more-severe corrosion at lower temperatures ($\sim 500\text{ }^{\circ}\text{C}$).

It is widely accepted that hydrogen diffuses from the fuel-side through the steel substrate and interferes with the oxidation process on the air-side. It has been shown that hydrogen has a high diffusivity in the BCC structure ($\sim 10^{-9}\text{ m}^2\cdot\text{s}^{-1}$) [157, 158]. Various hypotheses have been put forward to explain the mechanism leading to breakaway oxidation. Some authors [152, 153] have suggested that the formation of hydroxides in the oxide scale leads to the formation of hematite nodules (Figure 3.5) through accelerated diffusion of Fe ions. They assume that

metal vacancies can form to balance the positive charge created by substituting an oxygen anion with a hydroxide. This would increase the cation diffusivity. Another possible explanation is deformation of the surface (during cold work), which is known to trigger the nucleation and growth of oxide phases and increase the outward diffusion of cations [159-161]. Rufner et al. [94] have suggested that alteration of the oxygen activity by hydrogen could be a reason for the dual-atmosphere effect. The formation of steam within the oxide scale, which creates pores at high pressure, could increase scale growth and increase inward diffusion of oxygen. This hypothesis has also been proposed by Holcomb et al. [162].

Gunduz et al. [29] have focused on grain boundary diffusion as a means for hydrogen to mitigate Cr diffusion, leading to breakaway of the oxide scale. These authors studied three parameters: a) oxygen permeability; b) Cr_2O_3 growth rate; and c) Cr diffusion. Oxygen permeability is not reasonable because of the high Cr concentration needed to overcome the inward oxygen ingress by outward Cr diffusion, to prevent internal oxidation. Recently, Chyrkin et al. [163] have demonstrated that hydrogen has no effect on alloy lattice oxygen permeability in Fe-Cr within the SOFC/SOEC-relevant temperature range of $700^\circ - 900^\circ\text{C}$, thereby contradicting previous statements made by Essuman et al. [164] who suggested an acceleration of inward oxygen transport by dissolved hydrogen into the metal as an interstitial, leading to breakaway corrosion. Studies based on the work of Alnegren et al. [20] and Skilbred et al. [148] indicate that there is no significant increase in scale thickness between dual- and single-atmosphere conditions, after 500 h at 800°C . This excludes the idea of an increased chromia growth rate. According to these findings, the last parameter, Cr diffusion, seems to be the most-valid one. Hydrogen is believed to mitigate Cr diffusion at the grain boundaries, decreasing the Cr supply to the scale, thereby leading to the breakaway. Yang et al. [152] have further shown that increasing the Cr content (from 17 wt% to 23 wt%) decreases the severity of the dual-atmosphere effect.

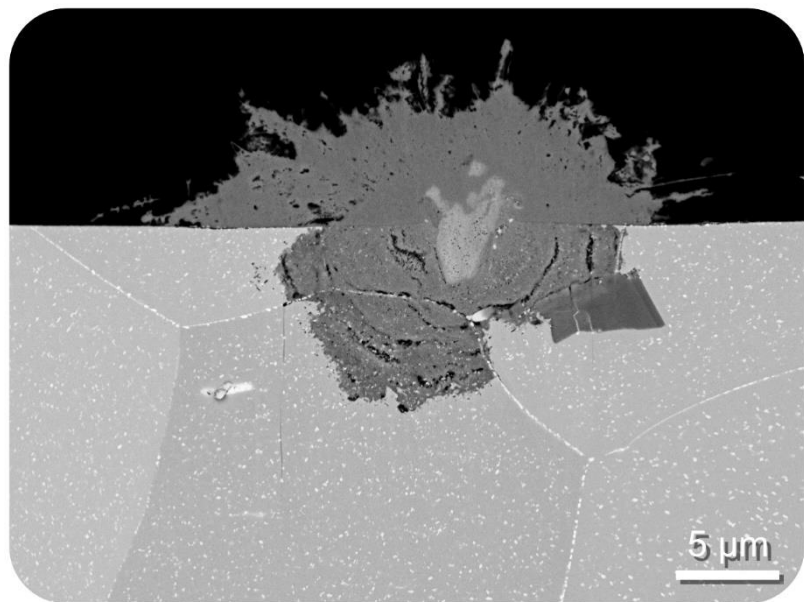


Figure 3.5: Cross-section of a hematite nodule formed on the air-side of a Crofer 22 H foil after exposure in dual-atmosphere conditions (i.e. Ar – 4.8 % H_2 – 3 % $\text{H}_2\text{O} // \text{air} – 3 \% \text{H}_2\text{O}$) at 600°C for 336 h.

4. Materials and Methods

4.1 Materials

Seven FSS with thicknesses in the range of 0.2 – 0.5 mm are investigated in this work for interconnect applications. Six of these are Cr₂O₃-forming steels and one is an Al₂O₃-forming steel. AISI 441, AISI 444, AISI 430 and EN 1.4622 are cheap commercial FSS, while Crofer 22 APU and Crofer 22 H are more-expensive, specifically designed FSS for interconnect applications. Kanthal EF 101 is an Al₂O₃-former. The chemical compositions of the studied materials are listed in Table 4.1.

Table 4.1: Compositions of the substrates (in wt%, as specified by the manufacturer) used in this work.

Materials	Fe	Cr	C	Mn	Si	Ni	Ti	Nb	Al	Cu	La	Mo	W	CIC ²
Crofer 22 APU (EN 1.4760) Batch A ¹	Bal.	22.92	0.004	0.38	0.01	/	0.06	/	/	0.01	0.09	/	/	[JU]
Crofer 22 APU (EN 1.4760) Batch B ¹	Bal.	22.8	0.004	0.4	0.02	/	0.06	/	/	0.01	0.1	/	/	[DK]
Crofer 22 APU (EN 1.4760) Batch C ¹	Bal.	22.74	0.002	0.45	0.02	0.01	0.06	<0.01	/	/	/	/	/	[FU]
Crofer 22 H (EN 1.4755) Batch A ¹	Bal.	22.61	0.018	0.42	0.35	0.46	0.09	0.49	/	0.02	0.07	/	1.94	[TQ]
Crofer 22 H (EN 1.4755) Batch B ¹	Bal.	22.93	0.008	0.46	0.22	0.26	0.06	0.5	/	0.02	0.07	/	2.12	[TR]
Crofer 22 H (EN 1.4755) Batch C ¹	Bal.	22.56	0.009	0.43	0.24	/	0.06	0.49	/	0.02	0.05	/	1.97	[TS]
AISI 441 (EN 1.4509)	Bal.	17.53	0.016	0.40	0.59	0.15	0.172	0.41	0.007	/	/	/	/	[KA]
EN 1.4622 (EN 1.4622)	Bal.	20.8	0.019	0.38	0.45	0.2	0.173	0.25	/	0.38	/	/	/	[KE]
AISI 444 (EN 1.4521)	Bal.	19.03	0.015	0.35	0.40	0.18	0.005	0.60	0.002	0.092	/	1.86	/	[MU]
AISI 430 (EN 1.4016)	Bal.	16.20	0.040	0.49	0.34	/	/	/	/	/	/	/	/	[OK]
Kanthal EF 101	Bal.	12.4	0.02	0.10	1.25	/	/	/	3.7	/	/	/	/	/

¹ Refers to the material investigation in **Paper II**, where different batches of Crofer 22 APU and Crofer 22 H were studied. In all of the other papers in which Crofer 22 APU and Crofer 22 H were investigated, the corresponding Batch A was used.

² Refer to the Chalmers Internal Code (CIC) used for materials classification.

Chapter 4

Depending on the type of experiment performed, the shapes, thicknesses, surface conditions and pre-treatment of the samples were different, as summarised in Table 4.2.

- For the single-atmosphere exposures performed in **Papers I, II, IV and V**, square-shaped samples (15 mm × 15 mm) were cut-out of a steel sheet and exposed as-received.
- For the dual-atmosphere exposures, coin-shaped samples (\varnothing 21 mm) were stamped out of a metal sheet using a hydraulic press. The pre-oxidation procedure used in **Papers II, III and IV** was at $800\text{ }^{\circ}\text{C} \pm 5\text{ }^{\circ}\text{C}$ for 20 min in air + 3 % H₂O. In **Papers II and III**, the samples were polished down to $\frac{1}{4}\text{ }\mu\text{m}$. In **Papers IV and V**, the samples were exposed as-received. In **Paper V**, the pre-oxidation procedure was at $800\text{ }^{\circ}\text{C} \pm 5\text{ }^{\circ}\text{C}$ for 20 min in air + 3 % H₂O with a ramp rate of $1\text{ }^{\circ}\text{C}\cdot\text{min}^{-1}$ up and down, under a flow rate of $280\text{ mL}\cdot\text{min}^{-1}$

Table 4.2: Details of the materials and conditions before exposure.

Parameter	Single-atmosphere	Dual-atmosphere
Thickness	0.3 – 0.5 mm	0.2 mm
Geometry	Square-shaped (15 mm × 15 mm)	Coin-shaped (\varnothing 21 mm)
Surface state	As-received	<ul style="list-style-type: none"> ▪ Polished ¹ down to $\frac{1}{4}\text{ }\mu\text{m}$ for uncoated samples. ▪ As-received for coated samples.
Pre-oxidation ²	No	Yes
Procedure	/	<ul style="list-style-type: none"> ▪ $800\text{ }^{\circ}\text{C} \pm 5\text{ }^{\circ}\text{C}$ for 20 min in air + 3 % H₂O with a flow rate of $280\text{ sml}\cdot\text{min}^{-1}$. In Paper V, a <u>ramp rate of $1\text{ }^{\circ}\text{C}\cdot\text{min}^{-1}$ up and down</u> was used.
Papers	I, II, IV & V	II–V

¹ If the samples were polished, SiC grinding papers with grits ranging from P800 to P4000 were used and, subsequently, diamond-polishing suspensions with grain sizes ranging from $3\text{ }\mu\text{m}$ to $\frac{1}{4}\text{ }\mu\text{m}$ were used for the final polishing.

² Pre-oxidation step simulates the temperature to that often occurring during the sintering process of a fuel cell stack, and a low flow rate and humidity were used to achieve a well-defined and easy procedure that was not dependent upon the outside weather conditions.

Further details as to why certain exposure conditions were chosen and how exposures and Cr(VI) evaporation measurements were conducted are provided below and in the following chapters.

4.2 Coatings

Depending on the experiment, specific sample geometries were required, and different coatings were studied. All of the coatings produced by Physical Vapor Deposition (PVD) were coated by Alleima AB [129]. Prior to deposition, the materials were cleaned in a 10 % solution of AK 13 (NaOH with tensides) for 10 min at 60 °C, followed by rinsing with tap water and deionised water. The Thermal Spray (TS) coatings were produced by Kuopion Konepaja Oy. The coating compositions, thicknesses and locations are specified in Table 4.3 for the single-atmosphere exposures, and in Table 4.4 for the dual-atmosphere exposures.

4.2.1 Single-atmosphere exposures

The coated samples investigated in the single-atmosphere condition were coated on both sides with the same coating thickness and composition. Unless stated otherwise, the investigated coatings exposed under the single-atmosphere condition did not have coated edges. For more details about the state of the samples before exposure, see Table 4.2.

Table 4.3: Characteristics of the materials and coatings used in **Paper I** under single-atmosphere conditions. The coatings were applied to sheets of the substrate, and the samples were cut out of the steel sheets in the form of 15 mm × 15 mm coupons.

Material	Thickness (mm)	Deposition process	Coating (thickness)	
			Inner	Outer
AISI 441	0.3	PVD	Ce (~20 nm)	Cu (~600 nm)
		PVD	Ce (~20 nm)	Mn/Cu (~600 nm)
		PVD	Ce (~20 nm)	Co (~600 nm)
AISI 441	0.3	TS	Cu oxide (~10 µm)	
		TS	Mn/Cu oxide (~10 µm)	
		TS	Mn/Co oxide (~10 µm)	

PVD, Physical vapour deposition; TS, thermal spray.

4.2.2 Dual-atmosphere exposures

Coated samples exposed under dual-atmosphere conditions did not undergo mechanical grinding or polishing and were heat-treated according to the procedure described in Section 4.1. For more details about the state of the samples before exposure, see Table 4.2. All of the samples were coated using the PVD process (Alleima AB) [129].

Table 4.4: Characteristics of the materials and coatings used in **Papers IV** and **V** under dual-atmosphere conditions. The coatings were applied, using a PVD deposition process, to sheets of the substrate, and the samples were stamped out of the steel sheets in the form of coin-shaped coupons (\varnothing 21 mm).

Material	Thickness (mm)	Coating (thickness)		Paper
		Fuel-side	Air-side	
AISI 441	0.2	Cr_2O_3 (~200 nm)	Uncoated	IV
		CeO_2 (~50 & 200 nm)	Uncoated	
		YSZ (~50 & 200 nm)	Uncoated	
		Al_2O_3 (~30 – 600 nm) ¹	Uncoated	
AISI 441	0.2	Al_2O_3 (~500 nm)	Uncoated	V
		Al (~1,000 nm)	Uncoated	
		Al (~1,000 nm)	Ce (~10 nm) / Co (~600 nm)	
		Uncoated	Ce (~10 nm) / Co (~600 nm)	

¹ In **Paper IV**, four different fuel-side Al_2O_3 coatings with thicknesses of 30 nm, 100 nm, 300 nm and 600 nm were investigated.

4.3 Exposures

The exposure conditions in all the experiments conducted within the scope of this work are listed in Table 4.5. For exposures where no heating rate is specified, no heating or cooling steps were applied; instead, the samples were directly inserted into the furnace at the exposure temperature and removed in the same manner. After exposure, all the samples were analysed using different analytical techniques, as described in the following sections.

Table 4.5: Detailed experimental matrix for all the conducted experiments included in the present work.

Paper	Geometry	Sample modification	Exposure conditions	Exposure time (h)	Ramp rate
I	Square-shaped (15 mm × 15 mm)	As-received	Single-atmosphere 650 °C in air + 3 % H ₂ O	1,000	Fast
		Pre-oxidised ³			
II	Square-shaped (15 mm × 15 mm)	As-received	Single-atmosphere 650 °C in air + 3 % H ₂ O	1,000	Fast
	Coin-shaped (Ø 21 mm)	Polished ¹ Pre-oxidised ¹	Dual-atmosphere 600 °C Atmosphere 1 ²	500	5 °C·min ⁻¹
III	Coin-shaped (Ø 21 mm)	Polished ¹ Pre-oxidised ¹	Dual-atmosphere 600 °C Atmosphere 1 & 2 ²	168	5 °C·min ⁻¹
IV	Square-shaped (15 mm × 15 mm)	As-received	Single-atmosphere 600 °C in Ar – 4.8 % H ₂ + 3 % H ₂ O	500	Fast
	Coin-shaped (Ø 21 mm)	Polished ¹ Pre-oxidised ¹	Dual-atmosphere 600 °C Atmosphere 1 ²	1,000 – 3,000	5 °C·min ⁻¹
V	Square-shaped (15 mm × 15 mm)	As-received	Single-atmosphere 600 °C in Ar – 4.8 % H ₂ + 3 % H ₂ O	168	Fast
	Coin-shaped (Ø 21 mm)	Polished ¹ Pre-oxidised ¹	Dual-atmosphere 600 °C Atmosphere 1 ²	3,000 – 7,000	1 °C·min ⁻¹

¹ According to the procedure detailed in Table 4.2.

² Refers to the different atmosphere compositions used in the present work. A detailed description of the composition of each atmosphere is provided in Table 4.7.

³ Pre-oxidation was performed on AISI 430 only, according to the procedure detailed in Table 4.2.

4.3.1 Single-atmosphere conditions

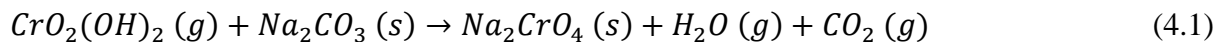
Single-atmosphere exposures were carried out in tubular furnaces (Figure 4.1). The experimental set-up used for tubular furnaces is shown in Figure 4.3. For **Papers I, II, IV and V**, the Cr(VI) evaporation, exposures in a fuel atmosphere (4.8 % H₂+3 % H₂O), and the mass gain measurements were carried out in tubular furnaces with a humid air flow that ranged from 120 sml·min⁻¹ to 6,000 sml·min⁻¹.



Figure 4.1: Tubular furnace used for the single-atmosphere exposures and Cr(VI) evaporation measurements.

4.3.2 Cr(VI) evaporation measurements

Cr(VI) evaporation is a major issue in relation to the life-spans of SOFCs. The emissions of Cr⁶⁺ species poison the cathode, thereby reducing its catalytic properties. Therefore, it is necessary to quantify the Cr(VI) evaporation during the exposure. Froitzheim et al. [87] have developed a technique to measure Cr evaporation in-situ. In this system, a denuder tube coated with Na₂CO₃ is placed downstream of the samples. The CrO₂(OH)₂ species that are evaporating from the samples will react with the Na₂CO₃ in the denuder, to form the thermally stable Na₂CrO₄. The chromate is then dissolved in water and the concentration of Cr(VI) species is determined by UV-VIS measurement at a wavelength of 370 nm. The chemical reaction upon which this measurement is based is shown in Equation (4.1):



The coated denuders (see Figure 4.3) were exchanged regularly during the exposure and rinsed with distilled water.

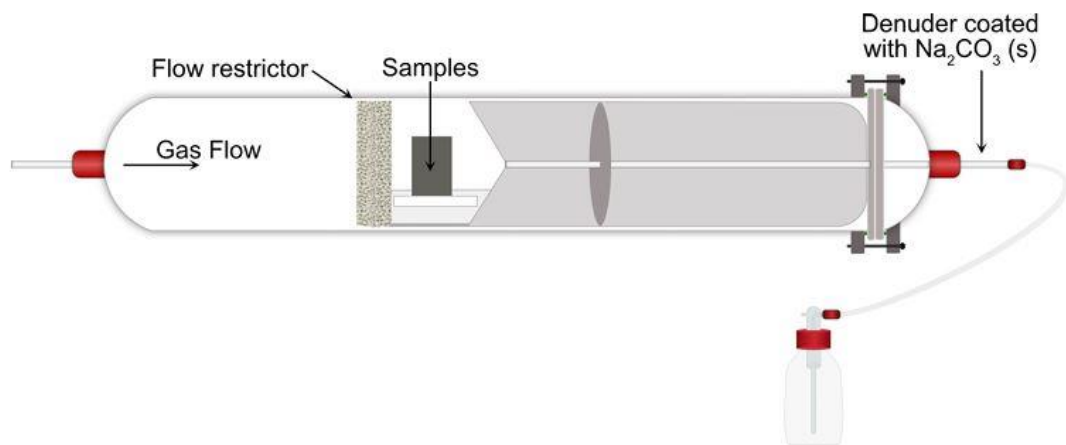


Figure 4.2: Schematic representation of the Cr evaporation technique. Courtesy of [125].

The absorbance of the resulting solution is measured by UV-VIS spectrophotometry using the EVOLUTION 60S UV-Visible spectrophotometer. As described in Section 2.4.5, the formation of $\text{CrO}_2(\text{OH})_2$ is dependent upon the water vapour concentration in the air. Therefore, all the experiments were carried out in an air atmosphere that contained 3 % H_2O vapour with a high air-flow rate ($6,000 \text{ sml}\cdot\text{min}^{-1}$), so as to ensure flow-independent Cr(VI) evaporation (Figure 2.8).

A more-detailed overview of the Cr(VI) evaporation measurement system is shown in Figure 4.3. Humidification was achieved by bubbling the gas (air or Ar-H₂) through heated water (30 °C) and subsequently, cooling the humidified gas to 24.4 °C, which corresponds to a humidity of 3 %. The humidity was verified using the Michell Instruments Optidew Vision™ chilled mirror dewpoint meter. For each set of Cr(VI) evaporation measurements and mass gain measurements, three samples were placed in the furnace (Figure 4.2).

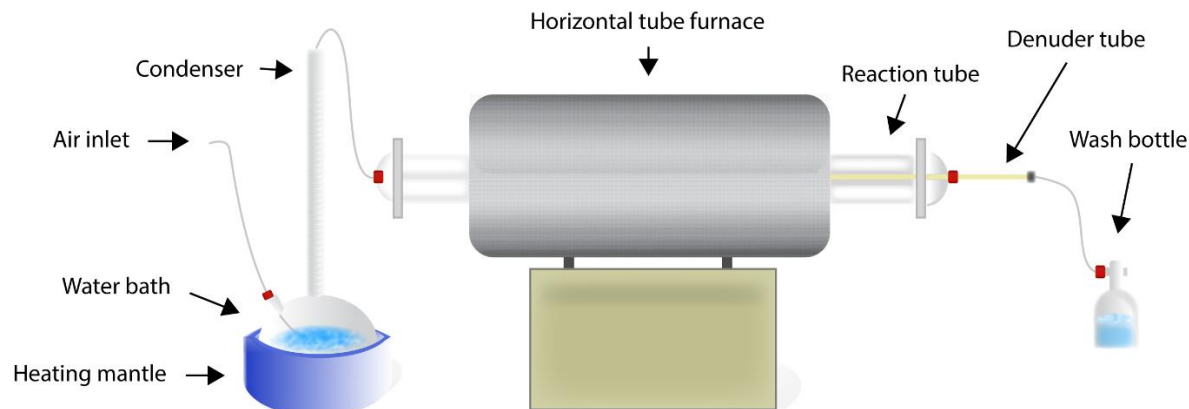


Figure 4.3: Experimental set-up for the tube furnace exposures and Cr(VI) evaporation measurements based on Froitzheim et al. [87]. Courtesy of [165].

4.3.3 Gravimetry measurements

The oxidation kinetics of the exposed steels were investigated in discontinuous mass gain experiments. For this, coupons were removed at regular intervals and cooled to room temperature. The mass gains were measured using a METTLER TOLEDO XP6 scale accurate to one-tenth of a microgram (Figure 4.4). After recording the mass, the coupons were placed back into the furnace. The mass gains from discontinuous measurements (non-isothermal) were compared to those obtained after Cr(VI) evaporation measurements (isothermal). The recorded mass gains are the sums of the oxygen intake and mass loss due to Cr(VI) evaporation. Therefore, the measured mass gains are not fully representative of the extents of oxidation and Cr consumption in the steel. Mass gain measurements should be compensated for the mass loss due to Cr(VI) evaporation. More-detailed information regarding the calculations can found in **Paper II**.



Figure 4.4: METTLER TOLEDO XP6 scale used for the mass gain measurements.

4.3.4 Dual-atmosphere conditions

A custom-made sample holder was used for the dual-atmosphere exposures described in **Papers II, IV and V** (see Figure 4.5). The design is based on work carried out at Montana State University. More details about the sample holder can be found elsewhere [94, 154, 162]. It is composed of 253 MA, which is an austenitic stainless steel with roughly 21 wt% Cr and 11 wt% Ni, in addition to other alloying elements.

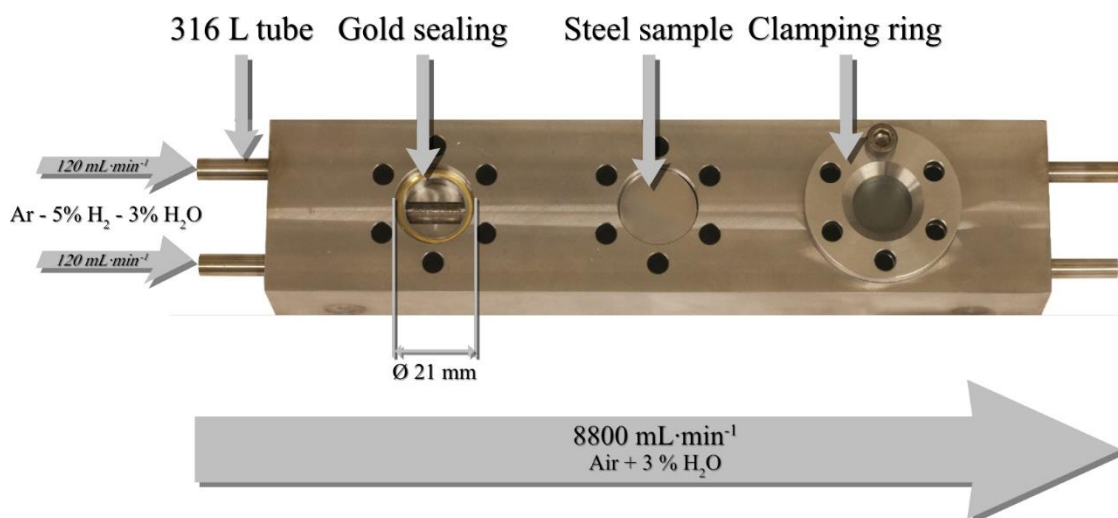


Figure 4.5: Sample holder used for the dual-atmosphere experiments described in **Papers II, IV and V**.

The sample holder contains six slots, three on each side. Gold rings are used to ensure gas tightness, which is controlled before and after exposure. The gas flow rates and compositions are described in Table 4.6 and Table 4.7.

The dual-atmosphere exposures performed in **Paper III** employed a different custom-made sample holder (see Figure 4.6) for safety reasons, as high concentrations (~97 %) of hydrogen were used. This sample holder is composed of SS316L steel and consists of an inner tube (OD: 6 mm; ID: 4 mm) that drives the fuel gas close to the sample, and an outer tube (OD: 10 mm; ID: 8 mm) that allows the fuel gas to back-flow to the exhaust. A check valve (6,000 psig) is installed at the fuel inlet, to stop the gas flow in case of ignition, for exposures involving high concentrations of hydrogen. More information can be found in **Paper III**.

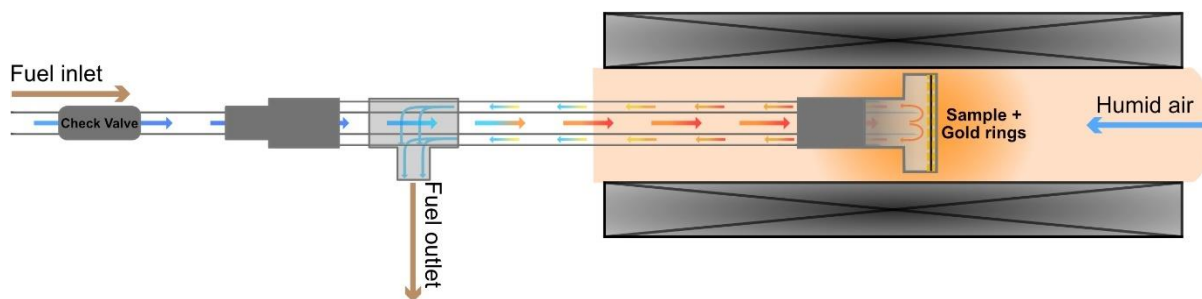


Figure 4.6: Schematic and operating principle of the dual-atmosphere sample holder used for the exposures involving high hydrogen concentrations in Paper III.

The humidity of the gas stream on the air-side was attained by bubbling the gas through water that was heated to 30 °C and, subsequently, cooling the humidified gas to 24.4 °C, which corresponds to a humidity of 3 % (see Figure 4.3). The humidity on the fuel-side was achieved by bubbling the gas through water that was heated to 37.3 °C, corresponding to 6 % humidity, and subsequently mixing with a similar dry gas with identical flow rate to reduce the humidity to 3 % (see **Paper III**).

All of the dual-atmosphere exposures were conducted at 600 °C. Pre-oxidation was implemented for all dual-atmosphere exposures according to the procedure described in Table 4.2. Optical images of the air-facing side of the samples were taken, using a Nikon SMZ800 camera equipped with a ring light, after exposure, or in some cases during exposure if the exposure had been interrupted. Electron microscopy, energy-dispersive x-ray spectroscopy (EDS), and ion beam milling were performed after dismounting the sample for further analysis of the corrosion products and oxide morphology.

Table 4.6: Flow rates for the different dual-atmosphere exposures performed in this thesis.

	Fuel-side	Air-side
Atmosphere 1	100 – 120 sml·min ⁻¹	6,000 – 8,800 sml·min ⁻¹
Atmosphere 2	100 sml·min ⁻¹	6,000 sml·min ⁻¹

Table 4.7: Details of the calculated gas compositions used for the dual-atmosphere experiments in the present work.

	Ar (%)		H ₂ (%)		H ₂ O (%)	
	Fuel-side	Air-side	Fuel-side	Air-side	Fuel-side	Air-side
Atmosphere 1						
pO_2 (fuel-side) = $7 \cdot 10^{-25}$ bars	92	/	4.85	/	3	Air + 3
Atmosphere 2						
pO_2 (fuel-side) = $1.7 \cdot 10^{-27}$ bars	/	/	97	/	3	Air + 3

4.4 Characterisation Methods

Different analytical methods were used to examine and characterise the samples and to evaluate the corrosion behaviours. Those techniques are described in the following sections.

4.4.1 UV-VIS spectrophotometry

The Cr evaporation technique described in Section 4.3.2 results in a solution that contains hexavalent chromate, which exists in seven different forms: CrO_4^{2-} , $\text{Cr}_2\text{O}_7^{2-}$, HCrO_4^- , H_2CrO_4 , HCr_2O_7^- , $\text{Cr}_4\text{O}_{13}^{2-}$ and $\text{Cr}_3\text{O}_{10}^{2-}$. Depending on the pH of the solution, different species are preferentially formed. At pH levels > 9 , CrO_4^{2-} is almost exclusively ($\geq 99.6\%$) formed [166]. Therefore, the solutions obtained from the denuders and wash bottles underwent pH testing. In cases where the pH was > 9 , a drop of a 0.1 M solution of NaOH was introduced to adjust the pH level. To quantify the chromium that evaporated during high-temperature exposure, UV-VIS spectrophotometry was used. If a solution contains light-absorbing materials (in this work, Cr^{6+}), the intensity of the light passing through the solution will decrease. The Beer-Lambert law [see Equation (4.2)] describes the relationship between absorbance A and the concentration of the light-absorbing species in the solution c :

$$A = \log \frac{I_0}{I} = \varepsilon_\lambda \cdot c \cdot l \quad (4.2)$$

where I_0 is the initial light intensity, I is the light intensity after passing through the cuvette, ε_λ is the wavelength-dependent molar absorption coefficient, and l is the path length through the sample (thickness of the cuvette). The highest level of light absorption by chromate ions in a water solution occurs at a wavelength of 370 nm. Consequently, all the concentration measurements were conducted using mono-chromatic light at 370 nm.

4.4.2 Broad Ion Beam Milling

To obtain well-defined cross-sections without affecting negatively the samples (and especially the thin oxide scales), a Broad Ion Beam [43] mill was used. The BIB bombards the sample with heavy ions, such as Ga^+ or Ar^+ . This removes the sample's surface in a layer-by-layer process (Figure 4.7), while smoothing it out. This technique avoids any mechanical issues that might occur when using the classical polishing method, and it allows for a broad cross-section that can be up to 2 mm in width, thus providing a better overview of the sample as compared to Focused Ion Beam (FIB) milling. Prior to milling, the samples are prepared in three steps. First, the samples are cut in the middle, perpendicular to the rolling direction, to ensure that the cross-section is representative of the entire sample. Second, the sections need to be gold-coated to provide better contrast for the SEM examination. In the third step, a silicon wafer is glued on top of the sample, to protect the oxide layer from the milling process. The Leica EM TIC 3X system was used for BIB milling, at a voltage of 8 keV.

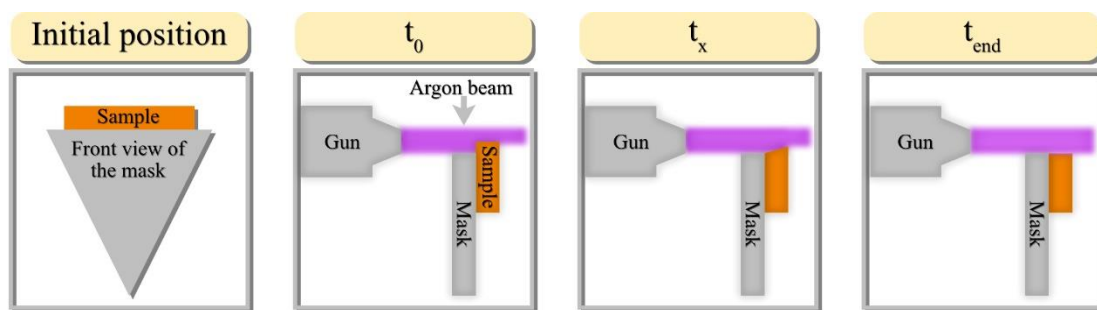


Figure 4.7: Schematic of the operating principle of the BIB milling process at different times. The ion source is Ar^+ .

4.4.3 Scanning electron microscopy / Energy-dispersive x-ray spectroscopy

SEM is a valuable tool for micro-structural and morphological examinations. Compared to optical microscopy, SEM has a resolution up to the nanometre range, which allows for detailed analyses of the thin oxide layers that form on steel substrates during high-temperature exposures. In SEM, accelerated electrons interact with the sample's surface. The nature of the resulting emissions depends on the energy released when the electrons of the sample are excited by an incoming electron beam (Figure 4.8). Different types of emissions can be analysed using various detectors. The three most commonly analysed emissions are:

- Secondary electrons
- Back-scattered electrons
- X-ray radiation

Since these emissions have different energies, they can easily be detected separately by different detectors. The signals that the detectors record can be used to generate an image of the sample surface. To understand the differences between the images created by the different detectors, it is essential to consider the interaction volume of each emission type (Figure 4.8d) [167, 168]. All the listed signals were used in this work and are described in greater detail below.

4.4.3.1 Secondary electrons

Secondary electrons (SE) are generated by the inelastic scattering of an incoming electron beam on a weakly bound electron. The incoming accelerated electron ejects an electron from one shell of an atom (usually the K shell). The ejected electron is called a secondary electron (Figure 4.8a). Due to their low energy (ranging from 1 eV to 20 eV), only the SE that are generated at the surface or close to the surface can be ejected from the material and be detected. As a consequence, SE are highly surface-sensitive and, therefore, can resolve the surface structure down to the order of 1 nm [167, 168].

4.4.3.2 Back-scattered electrons

Back-scattered electrons (BSE) provide both compositional and topographic information. They are generated by elastic scattering between an electron and an atomic nucleus (Figure 4.8b). Since these electrons are scattered at the nucleus, and heavier atoms have a larger nucleus, the number of BSE for heavier atoms is higher. Therefore, for heavy atoms, the signal is brighter in comparison to that for lighter atoms. The acceleration voltage for BSE is higher (between 15 kV and 20 kV), than that of SE, leading to a larger interaction volume (Figure 4.8d). Therefore, BSE have poorer spatial resolution and, thus, generate images with lower resolution [169].

4.4.3.3 Energy-dispersive x-ray spectroscopy

To acquire more-exact chemical information, EDS is used. For x-ray generation, the primary electron ejects an electron from the inner shell of an atom. An electron from the outer shell relaxes into the void. This relaxation of the atom to the ground state leads to the emission of x-ray photons (Figure 4.8c). The energy of the released x-ray photon is characteristic for each element. The x-ray radiation is emitted from much deeper in the sample than the SE or BSE, and the interaction volume for x-ray photons is larger. Thus, the resolution is drastically reduced (Figure 4.8d) [170, 171]. This can be an issue in cases where only the surface is being analysed. Consequently, other methods, such as Transmission Electron Microscopy (TEM) should be used to acquire high-resolution chemical and structural information.

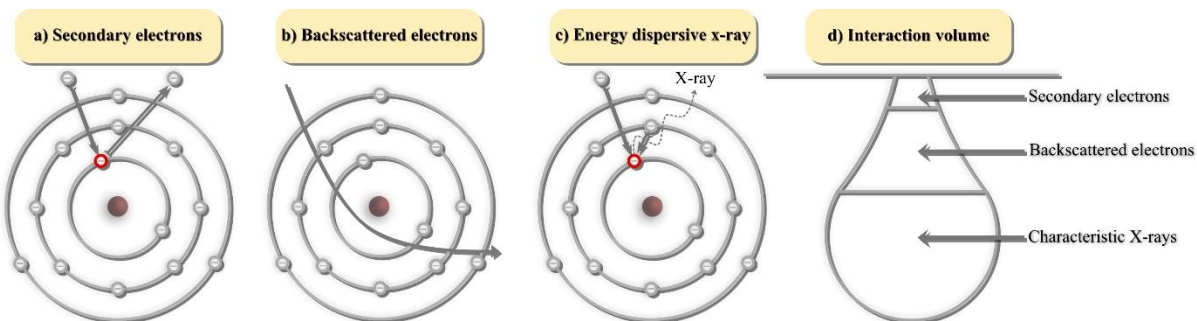


Figure 4.8: Schematic of the different SEM signals produced (a-c) and their interaction volumes (d) [167, 168].

4.4.4 Transmission Electron Microscopy

TEM is a tool that allows for higher-resolution characterisations of the microstructure, chemical composition, and crystal structure, as compared to SEM. In contrast to SEM, the electrons pass through the sample in TEM. Therefore, the sample must be extremely thin (usually 20 – 200 nm in thickness) in order to be transparent to electrons. TEM samples are prepared using Focused Ion Beam (FIB) milling to generate extremely thin lamellas for further TEM analysis. The reduced thickness of the lamellas artificially results in a reduced interaction volume, thereby avoiding interference with the EDX signal generated deeper in the sample. More information about the FIB procedure can be found elsewhere [172]. TEM operates at a very high acceleration voltage (usually 200 – 300 kV). If the sample is crystalline, the incoming electrons are diffracted by planes of atoms inside the material, forming a diffraction pattern that can be analysed to derive the crystal structure of the sample. Thus, the crystalline structure of a compound can be identified [173]. The TEM analysis was performed by Dr. Vijayshankar Asokan using the FEI Titan 80-300 TEM, which was equipped with an Oxford x-sight EDS detector. The images were acquired in scanning TEM mode using a High-Angle Annular Dark-field (HAADF) detector.

4.4.5 X-Ray Diffraction

XRD techniques are based on the ability of crystals to diffract X-rays in a characteristic manner allowing a precise study of the structure of crystalline phases. Diffractograms contain contributions of several micro- and macro-structural features of a sample. With the peak position, information such as: lattice parameters, space group, chemical composition, or qualitative phase analysis, can be obtained [174].

An incoming monochromatic X-rays beam is generated and oriented towards the sample where the beam is diffracted by interacting with the crystal structure of the sample (Figure 4.9a). Due to the periodic nature of the crystalline structure, constructive or destructive scattered radiation will result, leading to characteristic diffraction phenomena which can be studied to investigate the crystal structure of materials. The diffraction of the incident beam occurs only at specific angles and only if constructive interferences are achieved. These conditions are given when the Bragg equation is fulfilled [see Equation (4.3)] [174, 175].

$$n\lambda = 2d_{hkl} \cdot \sin\theta \quad (4.3)$$

where n is the order of diffraction, λ is the wavelength of the incident beam in nm, hkl are the Miller's indices, d_{hkl} is the lattice spacing in nm, and θ the angle of the diffracted beam in degree.

As the wavelength of the monochromatic beam X-rays is fixed, the incident angle θ is the varying parameter during measurements. In general, Bragg-Brentano geometry is used, which means that the distance between the sample and the detector is constant for all θ angles. (Figure

4.9b). However, it is possible to adjust the different parameters for a specific purpose, e.g. grazing-incidence. Grazing-incidence is used to acquire information for very thin oxide scales (~ 100 nm in this work). The primary beam is reaching the sample by a constant and very flat angle (usually 1° to 5°) while only the detector is scanning. This method is applied for the investigation of thin films in order to reduce the penetration depth of the X-ray beam inside the sample [174].

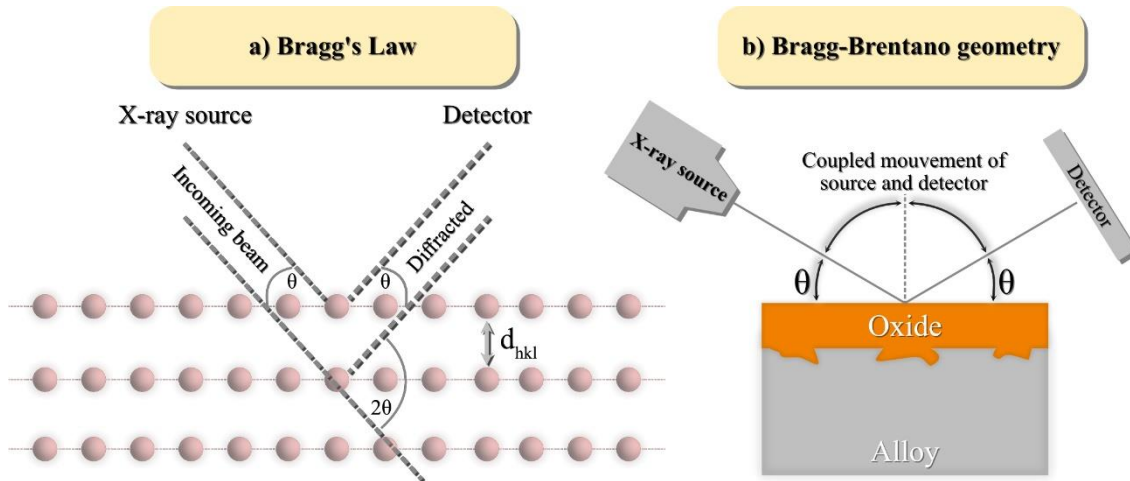


Figure 4.9: Schematic of: a) Bragg's law; and b) Bragg-Brentano geometry.

4.4.6 Area-specific resistance

ASR measurements were carried out in **Papers I, II, IV** and **V** to measure the resistances of the coated oxide scale and uncoated samples, both in humid air (**Papers I** and **II**) and humid H₂ (**Papers IV** and **V**). The measurements were exclusively done ex-situ, as in-situ measurements exhibit issues due to an effect from the Pt electrode on the overall resistance of the sample, as shown by Grolig et al. [176]. The ASR is the measured resistance I multiplied by the contact area (A). The standard procedure to measure the ASR values of the exposed samples is to sputter a Pt electrode of 1 cm^2 , using a sputter mask with an opening of $10 \times 10 \text{ mm}^2$ placed on the sample (Figure 4.10), and using a Quorom 150 sputter coater. The operation is repeated for the reverse side of the sample. Thereafter, the sputtered area is painted with a Pt-paste (Metalor M-9875), dried at 150°C for 15 min, and sintered at the exposure temperature for 1 h, as described for procedure **a** in Figure 4.10.

- In **Paper I**, due to poor adhesion of Pt to the Cu-oxide scales, an Au electrode was sputtered according to procedure **b** in Figure 4.10. To ensure optimal contact between the Pt electrode of the experimental set-up and the sample, a roughly 400-nm Au electrode was sputtered onto the sample.
- **Papers II, IV and V** followed procedure **c**. The sputtered electrode was made of Au. To ensure optimal contact between the Pt electrodes of the experimental set-up and the sample, Au paste was painted and sintered onto the Au-sputtered area.

A ProboStat (NORECS AS, Oslo, Norway) combined with a Keithley 2400 source meter was used for four-point probe measurements in DC mode (see Figure 4.11). The applied current was set to $100 \text{ mA} \cdot \text{cm}^{-2}$. The resistance was measured by the 2-points, 4-wires method for all measurements. ASR was measured at the exposure temperature and during the cooling period to verify the semi-conductive behaviour. For the exposures in fuel atmospheres described in **Papers IV** and **V**, the uncoated side of the sample was ground using SiC paper with P1200 grit, to remove the oxide layer, so as to minimise the contribution of that surface; as a consequence, the obtained values were not divided by two. More details on the procedure and experimental set-up can be found in [176].

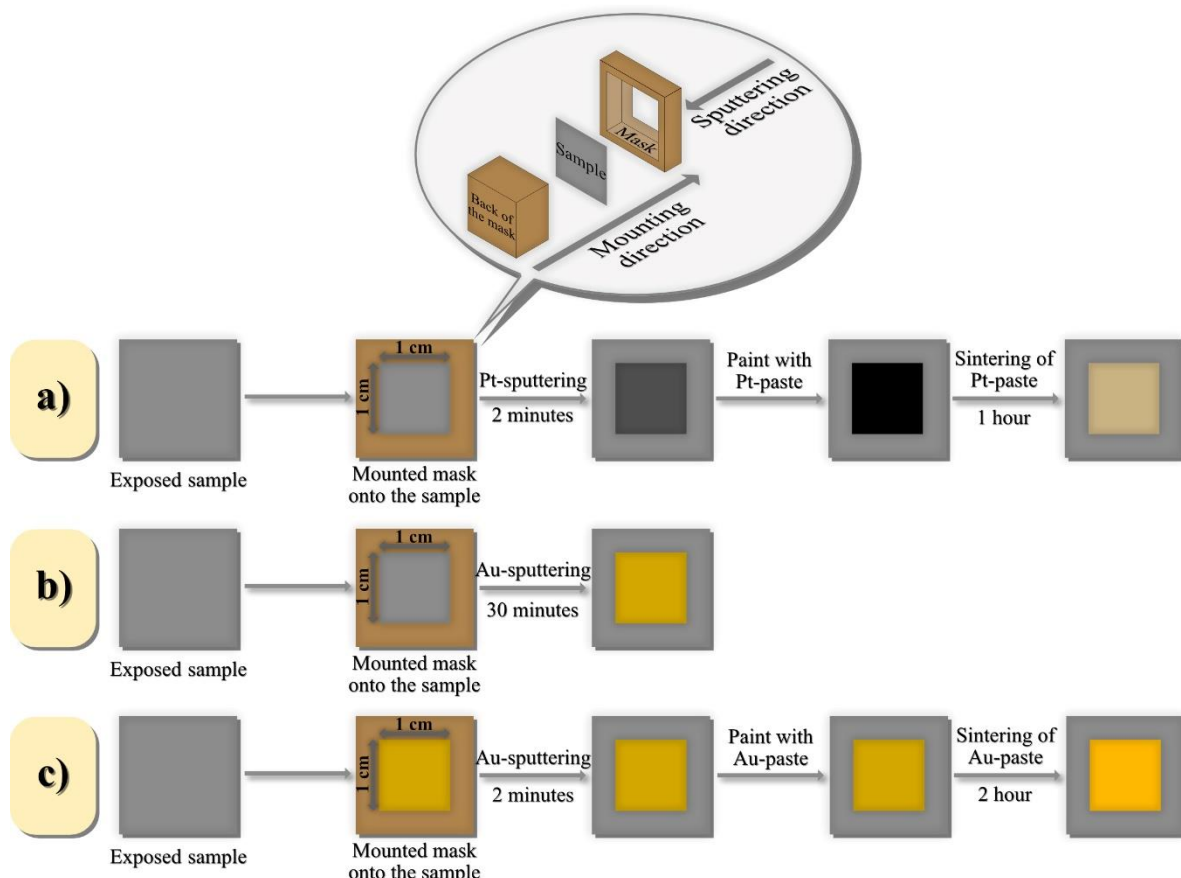


Figure 4.10: Schematic of the electrode preparation process.

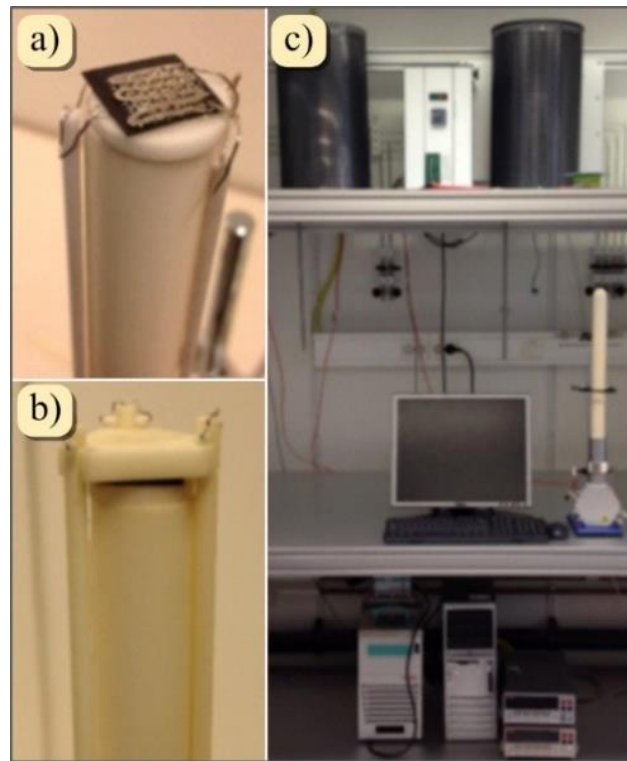


Figure 4.11: ASR experimental set-up showing: a) the mounted sample; b) the Probostat top; and c) the entire set-up

5. Results & Discussion

“If we knew what we were doing, it would not be called research, would it?”

– Albert Einstein

This thesis presents the results of experimental research on various metallic materials that are considered for use in SOFC technologies. Different FSS and coatings, under both single- and dual-atmosphere conditions are investigated, with respect to their suitability for interconnect applications. The experiments include assessment of Cr(VI) evaporation, oxidation kinetics, and ASR measurements, coupled with in-depth material characterisations with XRD, SEM, EDS and TEM. The results suggest potential strategies for mitigating high-temperature corrosion-related problems.

5.1 Single-Atmosphere Conditions – New Coating Systems to Reduce Cr(VI) Evaporation

The use of cheaper stainless steels, such as AISI 441 or AISI 430, potentially leads to shorter life-spans and more severe corrosion, as compared with specifically designed commercial steels such as Crofer 22 APU or ZMG™ 232, when exposed to high temperatures and humid atmospheres, although they are more cost-effective. Therefore, new mitigation strategies need to be identified to increase the life-spans of the interconnects. In Section 2.4.5, we stressed the importance of coatings in this respect, and discussed which corrosion phenomena can be mitigated by which coatings. Currently, one of the state-of-the-art coatings is the PVD Ce/Co coating [118, 125, 127, 132, 177], which consists of a very thin layer of Ce (\sim 10 nm) underneath a thin Co layer (\sim 600 nm). However, Co has been classified as a critical raw material by the EU [178], and Co mining is often associated with exploitation and child labour [179]. Furthermore, Cu is less toxic than Co (in dust form), entailing a lower risk for health issues [180]. The oxidation behaviours of uncoated, Co-coated and Cu-based coated interconnects exposed under a single-atmosphere and the resulting properties are discussed in the following sections.

5.1.1 Mitigating Cr(VI) evaporation – *Efficiency of the coatings*

Six uncoated chromia-forming steels (Crofer 22 APU, Crofer 22 H, AISI 441, AISI 444, AISI 430, EN 1.4622) and one alumina-forming steel (Kanthal EF 101) were exposed at 600 °C for 500 h. Their cumulative Cr(VI) evaporation are plotted as a function of time in Figure 5.1. Despite their different chemical compositions, the Cr₂O₃-forming steels display approximately similar levels of Cr(VI) evaporation, with a mean of $0.017 \pm 0.005 \text{ mg}\cdot\text{cm}^{-2}$ after 500 h of exposure at 600 °C. The slight difference in Cr(VI) evaporation observed between the different

Cr_2O_3 -forming steels is attributed to the concentrations of Cr in the outermost layer of the oxide scale. It has been shown previously that at lower temperatures, such as 600 °C, more Fe is incorporated into the Cr_2O_3 layer than at higher temperatures [181]. Reddy et al. [182] have reported higher Cr(VI) evaporation values (~3-fold higher) for AISI 441 and AISI 444 exposed at 650 °C for 500 h under similar conditions. This discrepancy is attributed to the lower purity level of the Cr_2O_3 layer formed at 600 °C.

AISI 430 was investigated under two different conditions: Condition A (as-received); and Condition B (pre-oxidised). The as-received AISI 430 (A) exhibits the lowest Cr(VI) evaporation (~10-fold lower) compared with its pre-oxidised version. This is attributed to breakaway oxidation leading to the formation of Fe oxide. Once it is pre-oxidised, AISI 430 (B) exhibits slightly higher levels of Cr(VI) evaporation compared with the other steel grades. This is attributed to the higher purity of the Cr_2O_3 cap layer (i.e., it contains fewer impurities, such as Fe), as compared with those formed at lower temperatures. The Al_2O_3 -forming steel (Kanthal EF 101) displays the lowest Cr(VI) evaporation among the uncoated steels. Similar results were found in previous studies [183]. Previous work [183, 184] have suggested a beneficial influence of Si on FeCrAl alloys in terms of further reducing Cr(VI) evaporation. In addition, they have proposed that the transport of Cr across the scale to the oxide/gas interface is impeded by the silicon-rich scale formed in humid air.

Compared to most uncoated samples, coated samples show a substantial reduction of Cr(VI) evaporation (Figure 5.2). Decreasing the exposure temperature by 50 °C resulted in an approximately 2.5-fold reduction in Cr(VI) evaporation for uncoated AISI 441. Previous research [83] has shown that a 100 °C decrease in temperature lowers the Cr(VI) evaporation by a factor of 2–3. The larger effect observed in this work is currently not understood.

In the present work, AISI 441 samples exposed at 600 °C and 650 °C exhibited a chromium evaporation of $0.021 \text{ mg}\cdot\text{cm}^{-2}$ and $0.05 \text{ mg}\cdot\text{cm}^{-2}$, respectively after 500 h of exposure. However, once coated, with either PVD or TS coatings, the Cr(VI) evaporation is approximately one order of magnitude lower on average. This trend persists even after 1,000 h of exposure, revealing the beneficial effects of coatings in terms of chromium evaporation mitigation.

Overall, all the coated samples display similar Cr(VI) evaporation (Figure 5.2). A slight difference is observed between PVD-coated and TS-coated samples. TS-coated samples display slightly lower Cr(VI) evaporation that could be attributed to coated edges. Previous research [132] has shown a noticeable effect of coated edges on Cr(VI) evaporation. Due to the sample preparation procedure, the edges of the PVD-coated samples are not coated while the edges of the TS-coated samples are coated. To compare PVD coatings with TS coatings, PVD Ce/Co-coated samples with coated edges were exposed to the same experimental conditions. After 1,000 h of exposure at 650 °C in humid air, they display similar Cr(VI) evaporation to the TS-coated samples. PVD coatings seem to be as efficient as TS coatings when the edges are coated, while the coating thickness is 10-times lower for PVD coatings (~1 μm for PVD vs. ~10 μm for TS). The use of Cu instead of Co shows promising results with respect to reducing Cr(VI) evaporation.

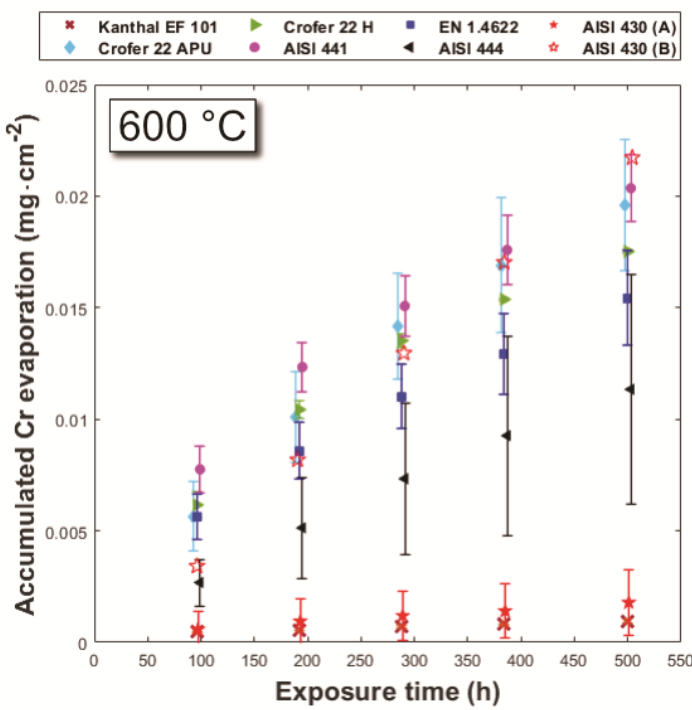


Figure 5.1: Cumulative Cr(VI) evaporation as a function of time for the Cr_2O_3 - and Al_2O_3 -forming steels exposed at 600 °C for 500 h in air that contained 3 % water vapour. The error bars represent the standard deviation. For Crofer 22 APU and Crofer 22 H, samples from Batch A were used, respectively. The symbols are slightly shifted (± 1 h) to enhance readability.

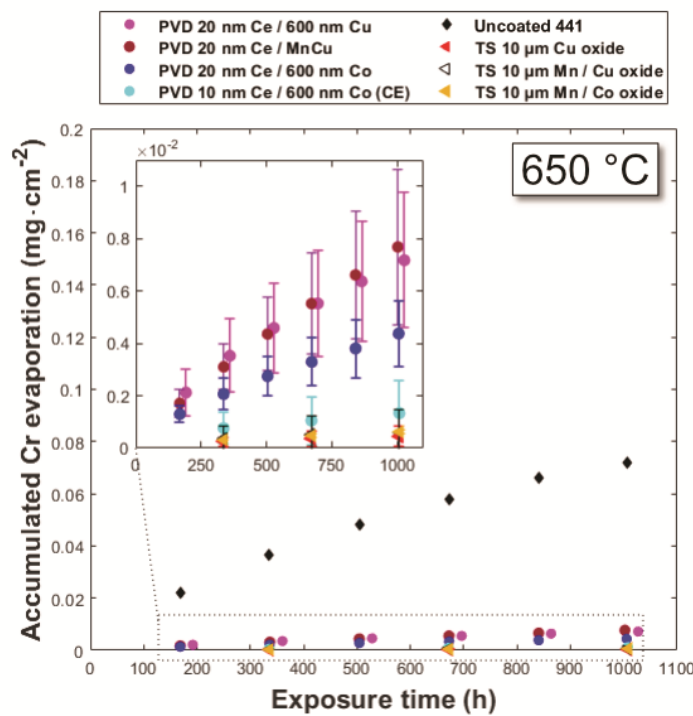


Figure 5.2: Cumulative Cr(VI) evaporation as a function of time for uncoated and coated AISI 441 samples exposed for 1,000 h at 650 °C in air that contained 3 % water vapor. Error bars indicate the standard deviation.

5.1.2 Oxidation kinetics – *From uncoated to coated steels*

Following exposure at 600 °C for 500 h, the mass changes are very small for all the exposed steels, with the exception of AISI 430 (A) (see Figure 5.3). Negative net mass gains are observed for Crofer 22 APU, Crofer 22 H and AISI 441 after 500 h of exposure, while positive net mass gains are observed for the remainder of the steels. Similar results are observed for AISI 441 samples exposed at 650 °C (Figure 5.4), as after 500 h of exposure, a small mass loss is observed. In this region, the mass loss through Cr evaporation ($\text{CrO}_2(\text{OH})_2$ species) dominated, leading to a net mass loss. Continuous Cr evaporation depletes the alloy of Cr, leading to the formation of less-protective oxide scales, such as iron oxides, and promoting rapid oxidation, a phenomenon that is termed *breakaway oxidation* [185]. The higher mass losses observed for Crofer 22 H, Crofer 22 APU and AISI 441 are attributed to the inter-play between the oxidation rate and Cr(VI) evaporation. Crofer 22 H has a slower oxidation rate and lower Cr(VI) vaporisation than Crofer 22 APU and AISI 441. A similar trend was observed in previous work conducted at 650 °C [182]. Once they are compensated for the mass loss due to Cr(VI) evaporation, all the samples show positive gross mass gains.

As stated previously, AISI 430 was investigated under two different conditions. Under the first condition (A), breakaway oxidation results in a high net mass gain and an almost equivalent gross mass gain, due to the growth of an Fe oxide that covers almost the entire surface, effectively lowering the Cr(VI) evaporation. Under the second condition (B), a protective behaviour is observed with a low net mass gain, similar of that seen for AISI 441, which is attributed to the pre-oxidation step that formed a protective Cr_2O_3 cap layer. AISI 430 (B) exhibits the highest gross mass gain, and this is attributed to a purer Cr_2O_3 layer being formed during pre-oxidation at 800 °C. Kanthal EF 101 shows similar net and gross mass gains, due to its low Cr(VI) evaporation. Similar values were found by Sand et al. [183] for Kanthal EF 101 (denominated A197) in humid air at 600 °C after 200 h of exposure.

When coated, all the samples exhibit a protective behaviour throughout the exposure (Figure 5.4). The rapid mass gains observed during the first 24 h for the PVD Ce/Co-coated and Ce/Cu-coated samples, as well as for the TS Mn/Co-coated samples, are attributed to oxidation of the coating. In the other cases, the mass gains are due to a combination of oxidation of the coating and the formation of fast-growing oxides, and the two phenomena cannot be differentiated. In the cases of the TS Cu and TS Mn/Cu coatings, the high mass gains observed during the first week of exposure are attributed to the deposition process, whereby the coating was not fully oxidised, such that a fraction remained in the metallic state. When exposed to a high temperature, the metallic part become oxidised, inducing a rapid mass gain. PVD Ce/Cu-coated samples seem to behave equally well as PVD Ce/Co-coated samples, providing an interesting coating alternative for IT-SOFC applications.

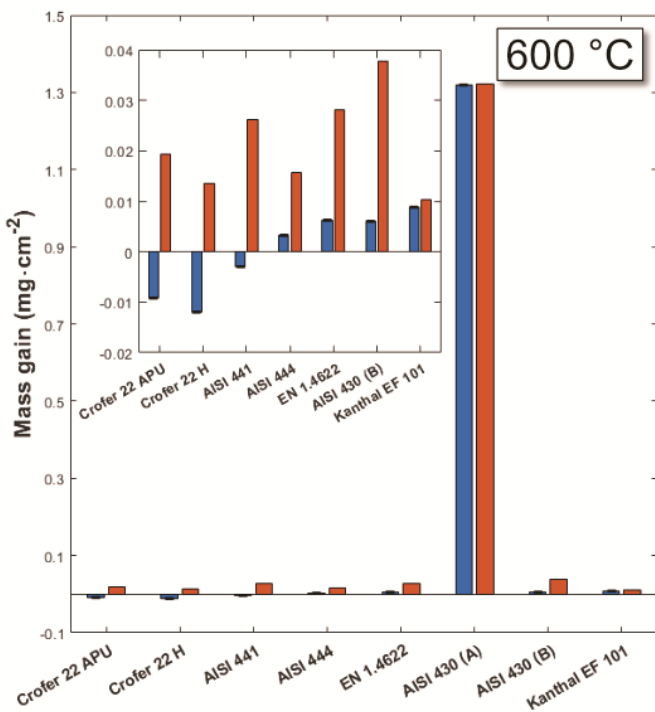


Figure 5.3: Mass gains of the different grades of steels exposed for 500 h at 600 °C in air that contained 3 % water vapour. The blue bars represent the net average mass gains, and the orange bars represent the gross average mass gains (corrected for the Cr evaporation). For Crofer 22 APU and Crofer 22 H, samples from Batch A were used, respectively.

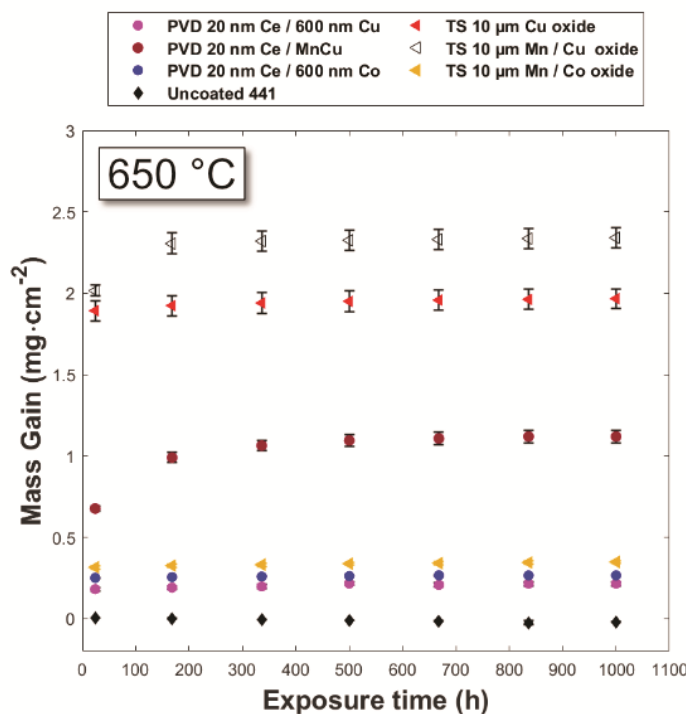


Figure 5.4: Average mass as a function of time for the PVD-coated, TS-coated, and uncoated samples, all of which were exposed for 1,000 h at 650 °C in air that contained 3 % water vapour. Error bars indicate the standard deviation.

5.1.3 Microstructural investigation – *Uncoated AISI 441*

Figure 5.5 shows a grazing-incidence X-ray diffractogram of AISI 441 exposed under single-atmosphere (air + 3 % H₂O) conditions for 500 h. Cr₂O₃ and (Cr, Mn)₃O₄ spinel were detected on the sample. Previous research [186] has shown the presence of the same phases on AISI 441 after exposure in humid air for 250 h at 650 °C. The presence of (Cr,Mn,Fe)₃O₄ is due to the presence of Mn and Fe in the alloy, which can diffuse through the Cr₂O₃ layer, forming a spinel at the outer oxide surface. All Cr₂O₃-forming alloys investigated in this work, are expected to form the same phases, except for AISI 430 (A).

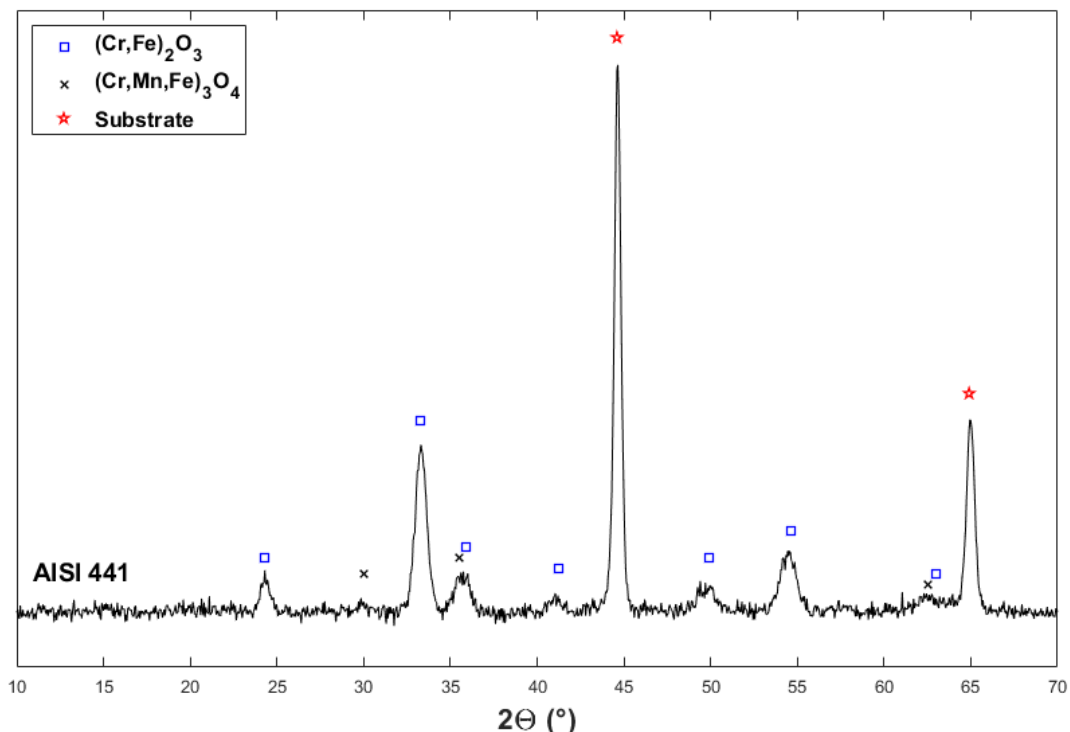


Figure 5.5: Grazing-incidence diffractogram performed for 20 h on an AISI 441 sample exposed under single-atmosphere (air + 3 % H₂O) conditions for 500 h at 600 °C.

5.1.4 Coating composition – A microstructural and chemical investigation

In this thesis, two coating deposition processes are investigated. Section 5.1.1 and Section 5.1.2 describe the efficiencies of the coatings in terms of Cr(VI) evaporation and mass gain. It is important to study the microstructures of the coatings and the natures of the oxides formed. The PVD process allows for the sputtering of thin multi-layered coatings [129], while the TS-deposited coatings exhibit much greater thicknesses. The microstructures of the latter is highly dependent upon the operating parameters, and the coatings tend to have higher porosity [187].

5.1.4.1 PVD-deposited coatings

The PVD Ce/Co-coated (Figure 5.6a) samples show a homogeneous $(\text{Co}, \text{Mn})_3\text{O}_4$ spinel top layer. A Cr_2O_3 layer is present closest to the metal, and is approximately 100 nm in thickness. At the $(\text{Co}, \text{Mn})_3\text{O}_4 / \text{Cr}_2\text{O}_3$ interface, a very thin CeO_2 layer is observed. A similar microstructure has been observed in a previous work [118]. If Co is substituted by Cu, a different microstructure appears. The PVD Ce/Cu-coated samples (Figure 5.6b) show two different microstructures: a homogeneous area, and a nodular area. The homogeneous area is composed a CuO top layer followed by a $(\text{Cu}, \text{Cr}, \text{Mn}, \text{Fe})_3\text{O}_4$ intermediate spinel, and closest to the metal, a thin Cr_2O_3 (~ 100 nm) layer. This microstructure is highly similar to that of the PVD Ce/Co coating. However, the oxide scale exhibits more pores than the PVD Ce/Co coating, possibly hindering adherence of the oxide scale. High-resolution imaging and EDS analysis of the homogeneous area were performed using TEM, to obtain a more-accurate elemental composition (refer to **Paper I**). In contrast, the nodules exhibit an Fe-rich phase that is located between the $(\text{Cu}, \text{Cr}, \text{Mn}, \text{Fe})_3\text{O}_4$ and the Cr_2O_3 (Figure 5.7b). The presence of an Fe-rich phase is typical of breakaway oxidation [72]. Figure 5.6c shows a cross-section of the PVD Ce-Mn/Cu-coated sample. In similarity to the PVD Ce/Cu-coating, two distinct microstructures are present: a homogeneous area, and a nodular area. The homogeneous area exhibits a top layer that is composed of $(\text{Cu}, \text{Mn}, \text{Fe})_3\text{O}_4$, and at the oxide/metal interface there is a thin chromia layer (~ 300 nm). A thin CeO_2 layer is visible at the spinel/chromia interface. EDS analysis shows a higher concentration of Cu at the Cr_2O_3 scale interface. Similar results are observed for the PVD Ce/Cu coatings. This is in line with the previous work of Talic et al. [188], in which they have suggested that faster diffusion of Cr takes place when Cu is present. The nodules contain a cap layer that is similar in composition to the homogeneous area. Underneath the $(\text{Cu}, \text{Mn}, \text{Fe})_3\text{O}_4$ cap layer, there is an Fe-rich oxide. The EDS analysis (Figure 5.7c) shows that Cu has diffused through the oxide scale during the exposure.

The switch from Co to Cu seems to induce some diffusion of Fe. The PVD Ce/Cu coating has Cr(VI) evaporation and oxidation kinetics comparable to those of the PVD Ce/Co coating within the studied temperature range. The PVD Ce-Mn/Cu-coated samples exhibit higher Cr(VI) evaporation than both previous coatings and display extensive formation of Fe-rich nodules.

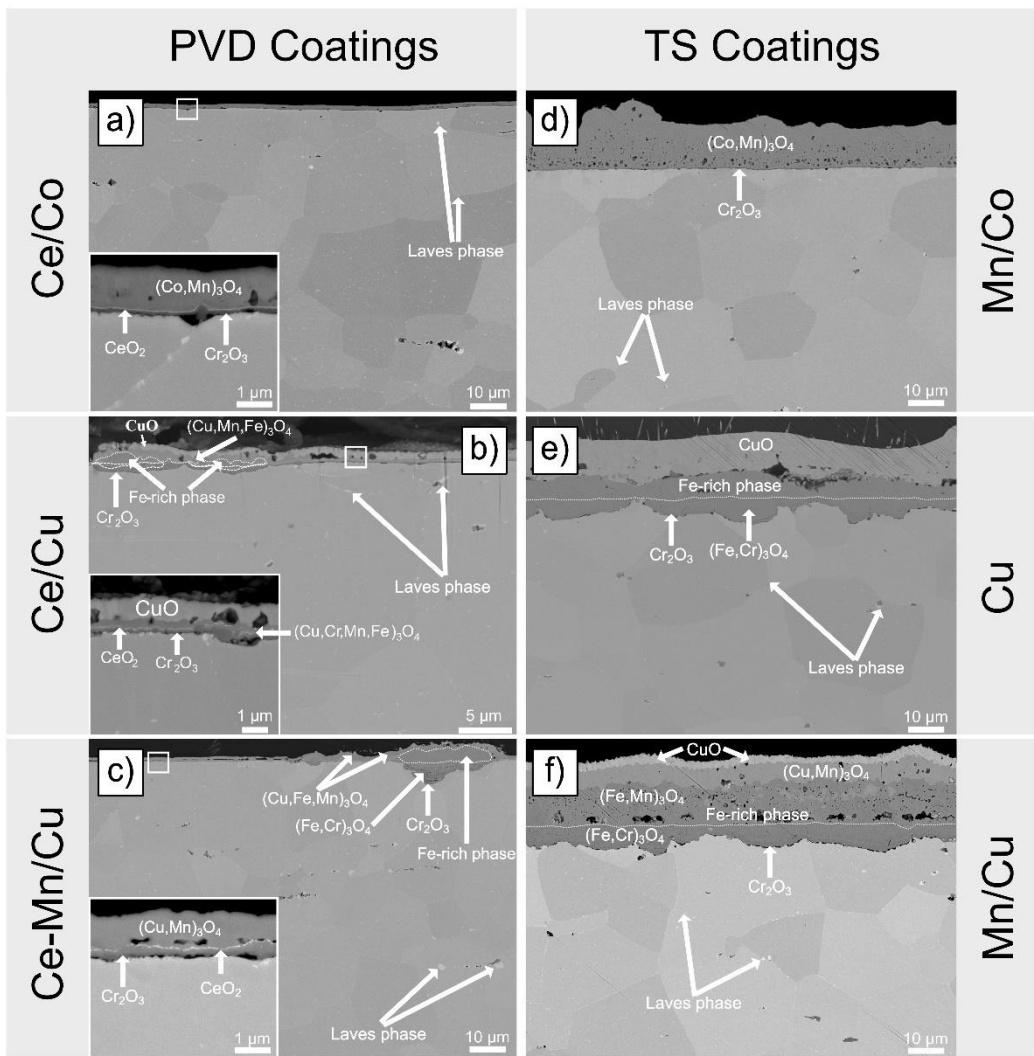


Figure 5.6: SEM Back-scattered Electron (BSE) image of BIB milled cross-section of the investigated PVD and TS coatings exposed to air + 3 % H_2O at 650 °C for 1,000 h.

5.1.4.2 TS-deposited coatings

The cross-sectional images of the TS-coated samples are depicted in Figure 5.6d-f. The TS Mn/Co-coated samples (Figure 5.6d) show a roughly 10 µm-thick $(Mn, Co)_3O_4$ spinel top layer, corresponding to the initial thickness and composition of the coating after deposition onto the sample. A thin chromia layer (~200 nm) is present closest to the metal (Figure 5.7d). Molin et al. [189] observed a similar microstructure for Crofer 22 APU. However, a thick Cr_2O_3 scale is present, most likely due to the higher porosity of the coating. The TS Cu-coated samples (Figure 5.6e) have a thick CuO cap layer (~10 µm), underneath which is a 5-µm-thick Fe-rich phase, followed by an $(Fe, Cr)_3O_4$ spinel. A Cr_2O_3 layer is observed at the metal/oxide interface. Clearly, Fe has diffused into the scale throughout the exposure. The PVD Ce/Cu-coated samples also exhibit Fe diffusion, albeit to a lesser extent, and it is mainly localised in the intermediate spinel. The TS Mn/Cu-coated samples show a six-layers microstructure. The top layer comprises a CuO-oxide layer, and beneath this is a $(Cu, Mn)_3O_4$ layer and an Mn-rich layer. These three phases may be due to the deposition process, i.e., the TS powder precursor,

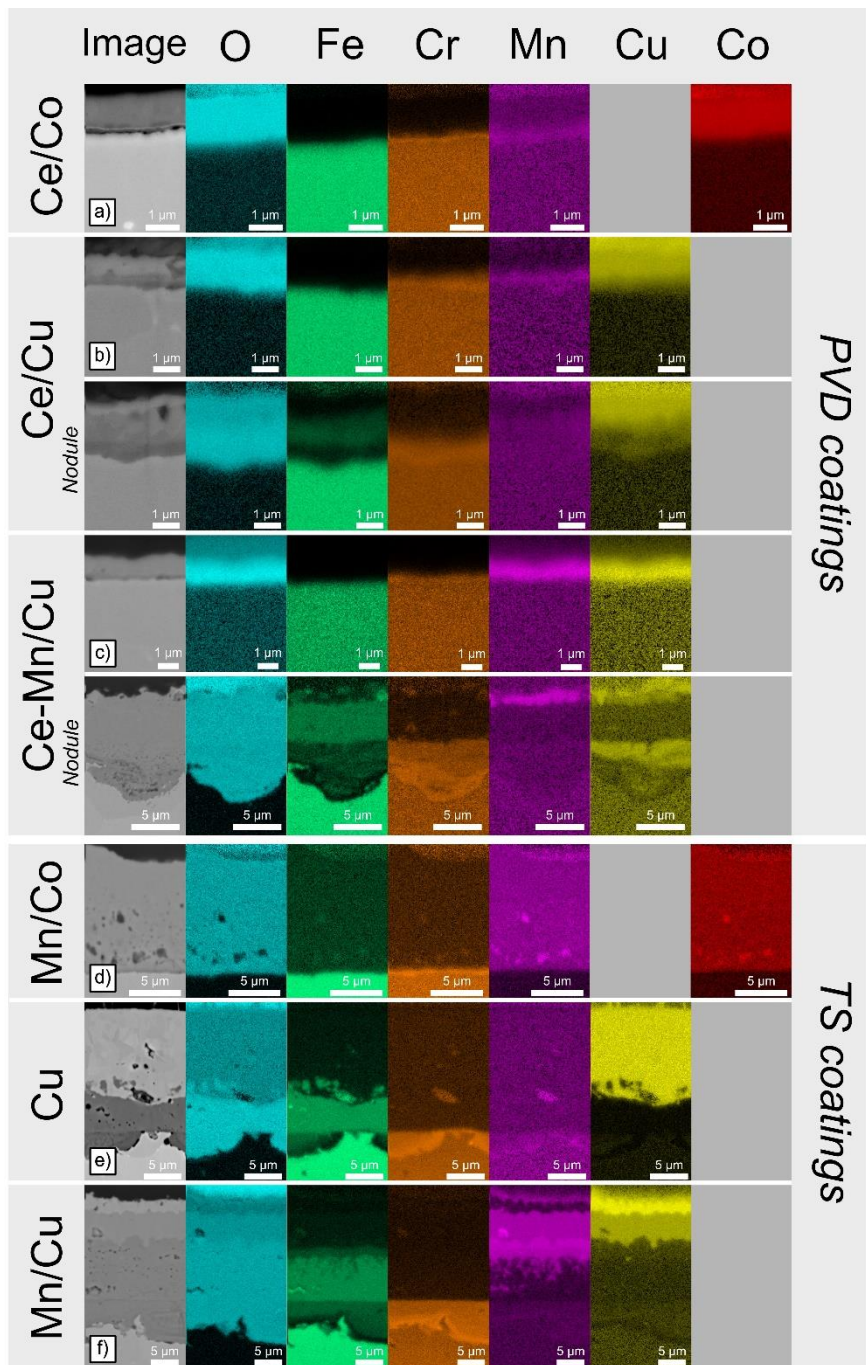


Figure 5.7: EDS mapping of the corresponding PVD and TS coatings exposed to air + 3 % H_2O at 650 °C for 1,000 h.

as discussed in Section 5.1.2. Beneath the top three layers, the cross-sectional image reveals the corrosion products: an Fe-rich oxide layer, an $(Fe, Cr)_3O_4$ layer, and finally, at the metal/oxide interface, a continuous Cr_2O_3 layer. The Fe-rich oxide layer is relatively porous. Cu-containing coatings seem to promote rapid Fe diffusion, resulting in Fe-rich intermediate oxide layers. The lack of a CeO_2 layer seems to affect the Cr_2O_3 thickness, as the TS-coated samples exhibit thicker chromia scales than the PVD-coated samples. The effects of REs have been described numerous times [110, 111, 190], and these elements are believed to promote selective oxidation of Cr and decrease the Cr_2O_3 scale growth rate. In addition, the presence of

a ceria layer seems to act as a diffusion barrier, as a lower level of Fe enrichment was observed on the PVD coatings than on the TS coatings. Falk Windisch et al. [118] have suggested a mechanism whereby a Ce layer acts as a diffusion barrier to impede the diffusion of Fe within the scale. A similar behaviour has been observed by Froitzheim et al. [191], who have suggested the use of CeO_2 as a barrier coating to avoid Ni diffusion from the anode in the FSS, thereby preventing the formation of a localised austenitic phase.

The TS-coated samples show lower Cr(VI) evaporation than the PVD-coated samples, which is attributed to having thicker scales from the start (ratio, 1:10). However, the difference should not be over-interpreted, as the Cr(VI) evaporation values are very low. Furthermore, Cu-containing coatings seem to suffer from higher Fe diffusion rates, leading to the formation of nodules or a continuous Fe-rich layer, as previously observed for PVD coatings.

5.1.5 Area-specific resistance – *Influence of the coating*

The ASR measurements for the different uncoated commercial FSS, including six Cr_2O_3 -forming steels (Crofer 22 APU, Crofer 22H, AISI 441, AISI 444, AISI 430 and EN 1.4622) and one Al_2O_3 -forming steel (Kanthal EF 101), are shown in Figure 5.8. Apart from AISI 430 (A), which exhibits breakaway oxidation, the Cr_2O_3 -forming steels have similar ASR values ($\sim 5 \text{ m}\Omega\cdot\text{cm}^2$) after 500 h of exposure. These results indicate that the thickness of the Cr_2O_3 layer is similar on all the Cr_2O_3 -forming steels. The electrical conductivity of chromia at 600 °C varies in the literature [63, 139, 140]. Enrichment of different alloying elements, such as Mn or Fe, within the Cr_2O_3 layer can lead to substantial changes in conductivity. As discussed in Section 3.3.4, Petric et al. [123] have investigated the electrical conductivities of certain spinels at high temperatures and found that the $\text{Mn}_{1.2}\text{Cr}_{1.8}\text{O}_4$ spinel exhibits low conductivity at 800 °C ($\sigma = 0.02 \text{ S}\cdot\text{cm}^{-1}$), and an even lower conductivity is expected at 600 °C. Falk Windisch et al. [192] have reported an ASR value of approximately $4 \text{ m}\Omega\cdot\text{cm}^2$ for Sanergy HT exposed at 650 °C for 500 h, which matches well with the measured values in the present work. Kanthal EF 101 displays the highest ASR values, and this is attributed to the growth of a thin Al_2O_3 layer, which is known to have insulating properties [62, 193, 194]. The presence of an Si-rich layer, as suggested by previous studies [183, 184], could further increase the overall ASR values.

To avoid a steep increase in Cr_2O_3 thickness, possibly leading to increased ASR [55], coatings can be used. The PVD Ce/Co coatings display the lowest ASR values (Figure 5.9). The average ASR value is $3 \text{ m}\Omega\cdot\text{cm}^2$, which correlates well with previous results for uncoated steels (Figure 5.8), indicating the presence of a Cr_2O_3 of similar thickness. Previous studies [110, 113] have described the beneficial effects of REs, such as Ce, in reducing the corrosion rate by changing the diffusion mechanism from outward diffusion of Cr to inward diffusion of oxygen, thereby reducing chromia growth. Previous research [118] conducted on Sanergy HT Ce/Co-coated samples has shown that Ce/Co-coated samples have ASR values of around $8 \text{ m}\Omega\cdot\text{cm}^2$ after 500 h of exposure at 650 °C under similar conditions. The PVD Ce/Cu-coated samples showed an ASR of about $15 \text{ m}\Omega\cdot\text{cm}^2$ after 1,000 h of exposure, while the Ce/MnCu-coated samples exhibited an ASR of about $28 \text{ m}\Omega\cdot\text{cm}^2$. These results are in line with those of the microstructural analysis (Figure 5.6). The PVD Ce/Cu-coated samples formed a very thin

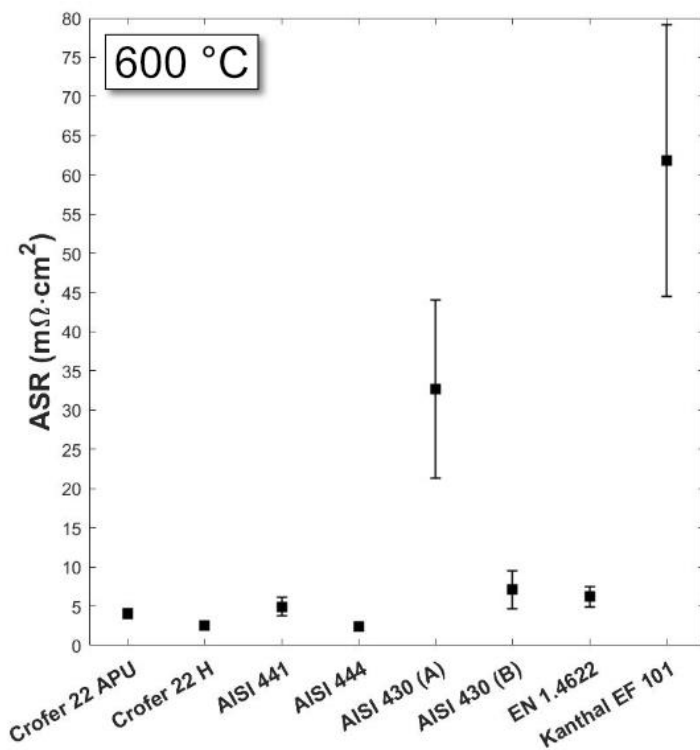


Figure 5.8: ASR measurements performed in air, on different grades of uncoated ferritic stainless steels exposed at 600 °C for 500 h in air + 3 % H_2O . Error bars indicate the standard deviation.

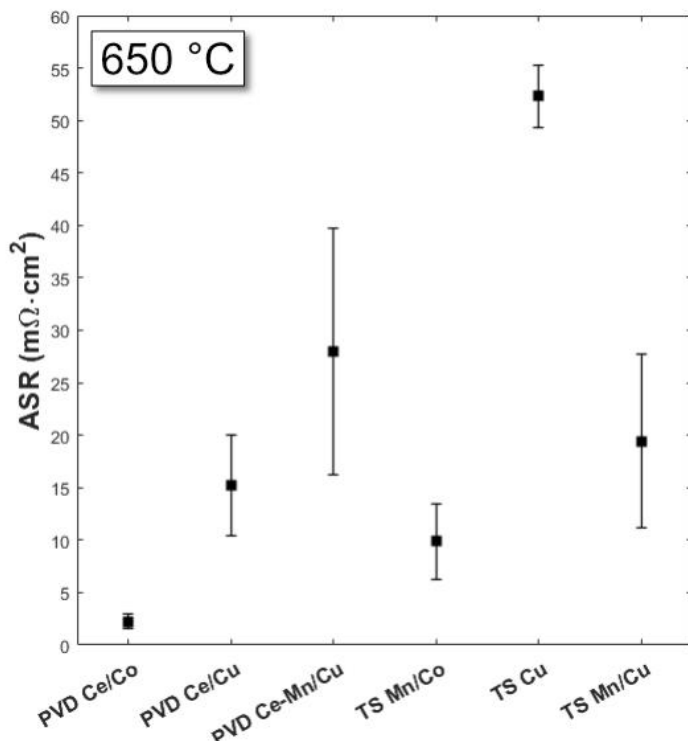


Figure 5.9: ASR measurements performed in air on PVD-coated and TS-coated samples exposed at 650 °C for 1,000 h in air + 3 % H_2O . Error bars indicate standard deviation.

Cr_2O_3 layer (~ 200 nm), while the Ce/MnCu-coated samples formed large oxide nodules with a slightly thicker chromia scale (~ 300 nm) underneath. As described in Section 3.3.4, manganite spinels, such as MnCo_2O_4 (60 S cm^{-1} at 800°C) and $\text{Cu}_{1.3}\text{Mn}_{1.7}\text{O}_4$ (225 S cm^{-1} at 750°C), are the most-conductive spinels, and a CuO-oxide layer is known to be conductive at high temperature ($2 \times 10^3 \text{ S cm}^{-1}$ at 700°C) [195]. The PVD Ce/MnCu-coated samples exhibit somewhat higher ASR values, as a significant part of the surface ($>50\%$) is covered with Fe-rich nodules. This accords with previous results showing that AISI 430 (A) has a higher ASR due to the Fe-rich oxide covering most of the sample's surface. The TS Mn/Co coating exhibits a low ASR value, comparable to that of the PVD Ce/Cu coating. This accords with the observation of a thin Cr_2O_3 layer underneath the coating. In contrast, the TS Cu coating has the highest ASR value, which is attributed to a thicker Cr_2O_3 scale and the presence of an Fe-rich intermediate oxide scale (pure within the accuracy limits of the EDS). The TS Mn/Cu coating exhibits these features as well but has a substantially lower average ASR of $19 \text{ m}\Omega\cdot\text{cm}^2$. This might be due to the presence of Mn in the Fe-rich layer. Overall, the PVD Ce/Co-coated and TS Mn/Co-coated samples exhibit similar ASR values, which are very similar to the values measured in uncoated samples. This indicates that the Cr_2O_3 layer does not grow significantly, allowing for good corrosion properties and an acceptable ASR penalty. However, as discussed in Section 5.1.4, Cu-based coatings seem to induce Fe diffusion to form Fe-rich intermediate layers, which drastically increases the ASR values.

5.2 Dual-Atmosphere Conditions – New Mitigation Strategies

As described in Section 3.4, the dual-atmosphere effect leads to increased corrosion on the air-facing side of the sample. The effect has been found to be most-pronounced at 600°C [20, 147]. Mitigating the dual-atmosphere effect is critical to increase the life-times of the interconnects when exposed around 600°C . Previous research [21, 144, 147, 196] has suggested a beneficial effect of pre-oxidation steps. The formation of chromia effectively reduces hydrogen permeation but it is insufficient. Therefore, coatings applied on the fuel-side or coating combinations applied on both sides appear to be promising approaches to address the dual-atmosphere effect and improving interconnect life-time.

5.2.1 Uncoated steels – *Evaluation of the corrosion behaviour*

This work investigated different uncoated commercial FSS, including six Cr_2O_3 -forming steels (Crofer 22 APU, Crofer 22H, AISI 441, AISI 444, EN 1.4622 and AISI 430) and one Al_2O_3 -forming steel (Kanthal EF 101), for their suitability as IT-SOFC interconnect applications. The steels were exposed to different dual-atmosphere conditions for 1–3 weeks, in order to evaluate the effects of alloying elements and gas compositions on the oxidation properties.

5.2.1.1 *Influence of the steel composition*

Top-view SEM micrographs of the different grades of steels, pre-oxidised for 20 min at

800 °C and exposed to classic dual-atmosphere conditions, i.e., Atmosphere 1 (4.8 % H₂ + 3 % H₂O), are shown in Figure 5.10a-g. A general trend is observed for the Cr₂O₃-forming steels, as they all exhibit non-protective behaviour after 500 h of exposure. However, substantial differences in the progress of breakaway corrosion are observed. Crofer 22 APU displays the highest resistance to the dual-atmosphere effect, as very few Fe₂O₃ nodules are present (Figure 5.10a). A higher concentration of Cr (~22.92 wt%) helps to maintain a Cr reservoir and sustain a protective Cr₂O₃ top layer. The presence of REs (e.g., La) helps to promote the selective oxidation of Cr and improve scale adhesion [110, 111, 190]. Kurokawa et al. [151] have demonstrated that hydrogen permeation through a chromia layer is about four orders of magnitude lower than that through an Fe-Cr steel. Therefore, it is possible that the earlier/purer Cr₂O₃ scale on the H₂/H₂O side plays a decisive role here in reducing the ingress of hydrogen. Crofer 22 H manifests more-severe corrosion than does Crofer 22 APU. As these two steels have comparable amounts of Cr and La, the likely difference resides in the presence of elements such as Si (~0.35 wt%), Nb (~0.49 wt%), and W (~1.94 wt%), leading to the formation of Laves phases within the grains and along the grain boundaries (Figure 5.11d).

AISI 441 shows a more-pronounced corrosion attack than Crofer 22 APU, although it has better corrosion resistance than Crofer 22 H. It is hypothesised that this surprising result is linked to a lower phase fraction of Laves phases compared to Crofer 22 H (Figure 5.11g). AISI 444 shows a more-severe corrosion attack than AISI 441 and seems to undergo slightly more-pronounced corrosion than Crofer 22 H. AISI 441 and AISI 444 have similar Cr contents, the main difference being the amount of Mo in AISI 444, which promotes the formation of Laves phase (Figure 5.11h), possibly affecting the corrosion resistance of the steel. Alloy 1.4622 exhibits milder corrosion than either Crofer 22 H or AISI 444 (Figure 5.10e), although it shows more-severe corrosion compared to Crofer 22 APU. AISI 430 seems to suffer milder corrosion than AISI 444 or Crofer 22 H, despite having a much lower Cr content (Figure 5.10f). It is hypothesised that it is because AISI 430 does not contain Laves phases.

Previous research [21] has suggested that hydrogen hinders the diffusion of Cr at the grain boundaries, thereby reducing the supply of Cr to the protective chromia oxide scale and leading to breakaway corrosion. In the cases of Crofer 22 H and AISI 444, the Laves phases precipitate predominantly at the grain boundaries, providing an almost continuous network throughout the entire thickness of the sample (Figure 5.11d,h). When comparing AISI 441 and AISI 444 (Figure 5.11e-h), a potential effect of the Laves phase concentration seems plausible, as these two steels have comparable Cr contents and grain sizes. However, AISI 444 has a much higher Laves phase fraction than AISI 441 and exhibits more-severe breakaway corrosion. Ponsoni et al. [197] have described a wide range of Laves phases and have suggested that the Fe₂Nb-type Laves phase can absorb hydrogen. Therefore, the Laves phase precipitates may provide easy pathways for hydrogen diffusion through the metal, thereby enhancing the dual-atmosphere-induced corrosion.

An alternative explanation for the higher-severity breakaway corrosion of Crofer 22 H (22 % Cr, ~7 % Laves phase) compared to AISI 430 (16 % Cr, no Laves phase) relates to differences in grain size. Crofer 22 H has the largest grain size, being roughly 32 µm in diameter. In contrast, AISI 430 has the smallest grain size (~9 µm in diameter) and shows a

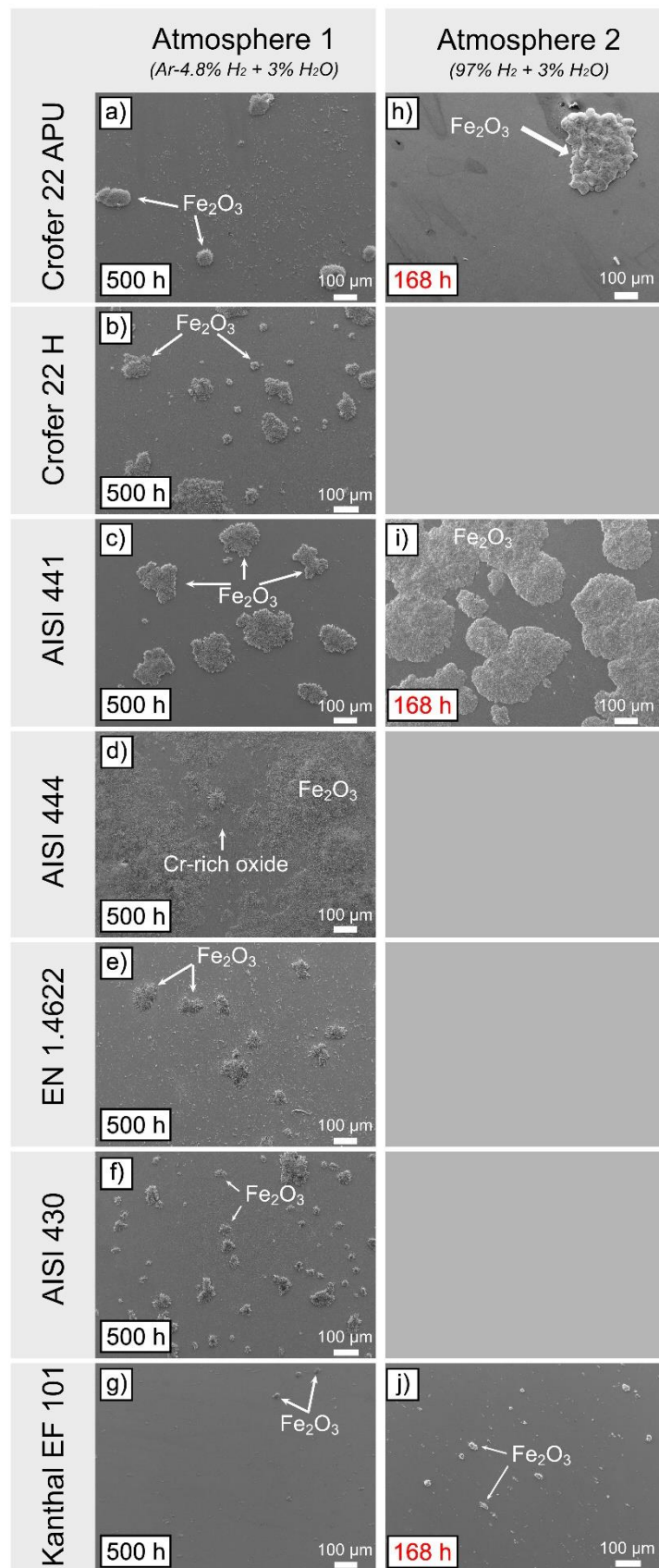


Figure 5.10: Top-view SEM micrographs of the different investigated steels pre-oxidised for 20 min at 800 °C and exposed under dual-atmosphere conditions at 600 °C for up to 500 h. Crofer 22 APU, AISI 441 and Kanthal EF 101 were exposed to two distinct fuel atmospheres, Atmosphere 1 and Atmosphere 2, for 500 h and 168 h, respectively.

more-protective behaviour despite having a lower Cr content than either Crofer 22 H or AISI 444. A smaller grain size facilitates more-efficient diffusivity pathways for Cr, and this is expected to be beneficial in terms of sustaining a protective chromia scale on the sample surface.

Kanthal EF 101 depicts almost no corrosion degradation after exposure, with only a very few and small Fe_2O_3 nodules being observed, which is attributed to the excellent hydrogen-barrier properties of the alumina oxide layer formed on top of the steel [198]. It is well-known that alumina oxides have very low H_2 permeability [199-201], making Al_2O_3 an ideal candidate for use as a hydrogen barrier.

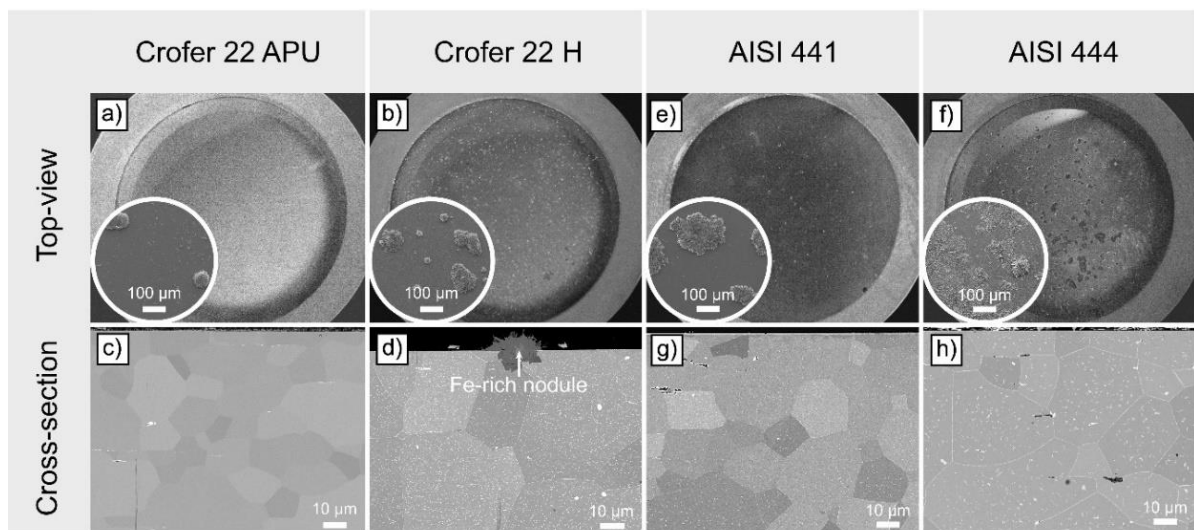


Figure 5.11: Photographs and SEM cross-sections of the air-sides of the selected alloys pre-oxidised for 20 min at 800 °C and exposed under dual-atmosphere conditions ($\text{Ar}-5\% \text{H}_2 + 3\% \text{H}_2\text{O} // \text{Air} + 3\% \text{H}_2\text{O}$) at 600 °C for 500 h. For Crofer 22 APU and Crofer 22 H, samples from Batch A were used, respectively. The insets show high-magnification SEM images of the corresponding alloys.

5.2.1.2 Effect of the gas composition of the fuel-side

Top-view SEM micrographs of Crofer 22 APU, AISI 441 and Kanthal EF 101 that were exposed to a high concentration of hydrogen on the fuel-side, i.e., Atmosphere 2 (97 % H_2 + 3 % H_2O), for 168 h at 600 °C, are shown in Figure 5.10h-j. A direct comparison of identical samples that were exposed to classic dual-atmosphere conditions, i.e., Atmosphere 1 (4.8 % H_2 + 3 % H_2O), and samples that were exposed to more-aggressive dual-atmosphere conditions, i.e., Atmosphere 2, shows a major effect of the hydrogen concentration. Samples that were exposed to almost pure hydrogen on the fuel-side display a more-severe corrosion on the air-facing side already after only 1 week of exposure. Among the Cr_2O_3 -forming steels, Crofer 22 APU seems to be less-affected by the more-aggressive fuel atmosphere (i.e., Atmosphere 2), as fewer nodules (~200 – 300 μm in diameter) are observed (Figure 5.10h). However, once exposed to Atmosphere 2, AISI 441 exhibits a surface that is almost fully covered with Fe_2O_3 (Figure 5.10i). This difference in corrosion resistance between Crofer 22 APU and AISI 441 is attributed to Crofer 22 APU having higher contents of Cr and RE, which facilitate the formation and maintenance of a more-protective Cr_2O_3 scale, thereby reducing the dual-atmosphere

effect.

Kanthal EF 101 displays the most-impressive behaviour of all the investigated FSS. As shown previously, when exposed to Atmosphere 1 (4.8 % H₂ + 3 % H₂O), the Al₂O₃-forming steel shows limited corrosion degradation, as very few Fe₂O₃ nodules are observed. Once Kanthal EF 101 is exposed to a more-aggressive environment, i.e., Atmosphere 2 (97 % H₂ + 3 % H₂O), for just 1 week at 600 °C, the sample displays more Fe₂O₃ nodules on the surface (Figure 5.10j), although they are still extremely small compared to those on the previously investigated Cr₂O₃-forming steels. Reisert et al. [144] found similar results for Al₂O₃-forming steel, after exposure under dual-atmosphere conditions (similar to Atmosphere 1) for 100 h at 600 °C. They noted the formation of Fe₂O₃ nodules surrounded by a γ-Al₂O₃ protective scale. Different studies [202, 203] have shown low hydrogen permeation of FeCrAl steels in the temperature range of 150 ° – 850 °C, as compared to pure Fe or Fe-Cr steels. Fe-Cr-Al alloys form a thin Al₂O₃ layer that acts as a hydrogen barrier. Alumina is known for its very low hydrogen permeation [199]. The most-desirable phase is α-Al₂O₃. Somjit et al. [204] have attributed the excellent hydrogen barrier properties of undoped α-Al₂O₃ to Al vacancies that trap hydrogen. They have also stated that doping the Al₂O₃ layer with Fe or Cr might further reduce hydrogen permeability. Nevertheless, a transient alumina layer seems to be effective in reducing drastically the hydrogen permeation on the fuel-side.

The exact mechanism behind the dual-atmosphere effect is presently unknown and widely debated. However, there is a consensus that hydrogen from the hydrogen-rich side diffuses through the metal and negatively affects air-side oxidation. The dual-atmosphere effect has been observed on both Cr₂O₃-forming and Al₂O₃-forming FSS, occurring after short periods of time and associated with noticeable differences in corrosion depending on the oxide formed during the exposure. As stated previously, Gunduz et al. [21] have proposed that hydrogen is blocking Cr diffusion at the grain boundaries, so as to inhibit chromia formation. In a recent paper, Reisert et al. [144] have hypothesised that the diffusion of hydrogen through the metal to the oxide alters the defect structure of the oxide, thereby facilitating the outward diffusion of iron, accelerating cation transport, and promoting the formation of thin whiskers/platelets through enhanced oxidation processes. These observations are in accordance with previous research carried out by Yang et al. [152], who have suggested that there is an increase in the concentration of cation vacancies in the oxide, which accelerates scale growth. Previous studies [205-207] have suggested that dissolved hydrogen increases oxygen permeability in the alloy, promoting internal oxidation, excessive depletion of Cr, and the earlier onset of breakaway oxidation. However, Chyrkin et al. [163] have studied the effects of hydrogen on oxygen permeability in a Pd-Cr alloy and Fe-Cr, in the temperature range of 600 ° – 950 °C, and they have found no effect. In another study [208], the same authors have demonstrated that dissolved hydrogen does not affect lattice oxygen permeability in ferrite.

These observations lead to the conclusion that hydrogen diffusion barrier coatings are necessary to improve the life-times of interconnects. In the following sections, fuel-side coatings and coating combination are investigated, as well as their electrical properties.

5.2.2 Mitigation of the dual-atmosphere effect – *Coatings as hydrogen diffusion barriers*

Coatings are necessary to reduce Cr(VI) evaporation from FSS, as discussed in Section 3.2 and Section 5.1. Therefore, researchers have focused on coatings for the air-facing side of the interconnect [81, 125, 209]. However, the results highlight the importance of a protective layer on the fuel-facing side, to act as a barrier to hydrogen diffusion, so as to reduce the dual-atmosphere effect. This work evaluates different PVD coating deposited on the fuel-side, as well as PVD coating combinations on both sides for AISI 441 samples exposed under dual-atmosphere conditions (i.e., Atmosphere 1: 4.8 % H₂ + 3 % H₂O) for up to 7,000 h.

5.2.2.1 Fuel-side coating systems

Top-view SEM images of the air-side of uncoated AISI 441 and cross-sections of the fuel-sides of coated AISI 441 samples, exposed for 1,000 h under dual-atmosphere conditions, are shown in Figure 5.12a-e. The top-views of the air-sides of both the uncoated and Cr₂O₃-coated samples (Figure 5.12a,b) show a mostly corroded surface that is covered by an Fe₂O₃ oxide layer. Approximately 65 % of the steel surface is covered by a poorly protective hematite layer. A Cr-rich layer is still visible as small patches on the sample's surface in both the uncoated and Cr₂O₃-coated samples. The CeO₂-coated samples show a drastic reduction in corrosion on the air-side of the sample (Figure 5.12c). The sample's surface is mostly covered by a protective Cr-rich oxide layer with evidence of some Fe₂O₃ nodules, which are approximately 100 µm in diameter and cover around 2 % of the sample's surface. A similar behaviour is observed for the YSZ-coated samples. The surface of the sample is covered predominantly by a protective Cr-rich oxide scale, together with the presence of some Fe₂O₃ nodules, which are approximately 80 µm in diameter (Figure 5.12d). The YSZ-coated samples show a greater reduction in Fe₂O₃ coverage (~ 0.1%) compared with the CeO₂ coatings. After 3,000 h of exposure under dual-atmosphere conditions, the 30-nm Al₂O₃-coated samples show limited corrosion on the air-facing side. The nodules are approximately 100 µm in diameter and cover less than 0.3 % of the surface. The corrosion level on the air-side is comparable to that on the YSZ-coated samples after a three-times longer exposure time. The SEM cross-sectional micrographs of the fuel-sides of the uncoated and PVD-coated AISI 441 samples exposed for 1,000 h under dual-atmosphere conditions are shown in Figure 5.12f-j. The fuel-side cross-sectional image of the uncoated sample (Figure 5.12f) shows a thin (<100 nm) and continuous Cr₂O₃ layer, while the PVD Cr₂O₃-coated sample shows a homogeneous and thin Cr₂O₃ layer that is roughly 200 nm in thickness (Figure 5.12g). The cross-section of the CeO₂-coated sample (Figure 5.12h) shows a thin (<100 nm) and continuous Cr₂O₃ layer underneath the continuous CeO₂ coating. The SEM cross-sectional image of the fuel-side of the YSZ-coated sample (Figure 5.12i) shows a thin YSZ oxide layer on top of a thin Cr₂O₃ layer. The fuel-side cross-sectional image of the Al₂O₃-coated sample shows the presence of a mixed Al₂O₃/spinel top layer (Figure 5.12j), which is followed by a thin Cr₂O₃ layer.

As shown previously, uncoated AISI 441 FSS suffers from severe breakaway oxidation after exposure at 600 °C under dual-atmosphere conditions, even when the steel sample is pre-oxidi-

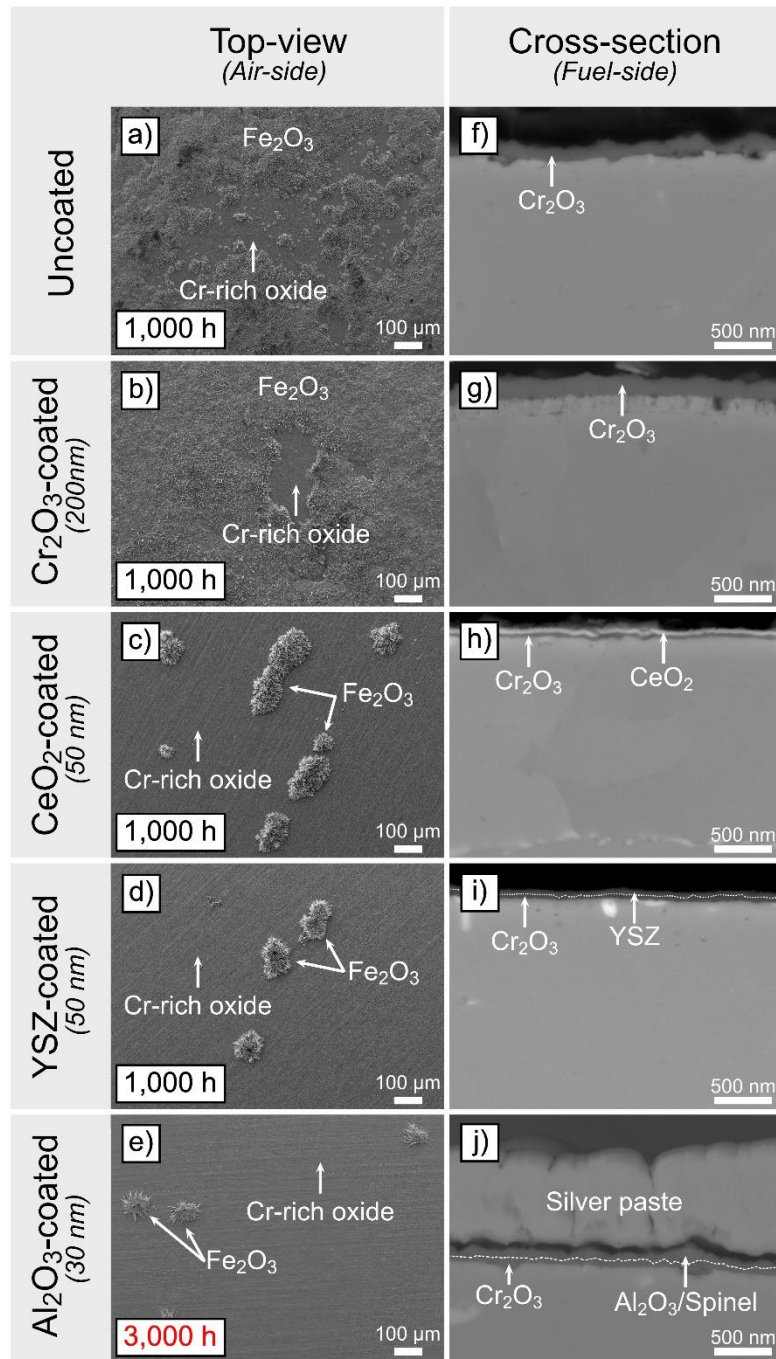


Figure 5.12: Top-view SEM micrographs of the air-side (a-e) and SEM cross-sectional micrographs of the fuel-side (f-j) of the investigated AISI 441 uncoated and PVD-coated samples on the fuel-side, pre-oxidised for 20 min at 800 °C and exposed under dual-atmosphere conditions (i.e., Atmosphere 1) at 600 °C for up to 3,000 h.

-sed. The pre-oxidation step, which is designed to replicate stack conditioning prior to operation, is anticipated to produce a protective Cr_2O_3 layer that serves as a barrier to both alloy oxidation and the migration of hydrogen from the fuel-side to the air side. Previous research [151] has exposed an Fe-16Cr steel at 800 °C and has demonstrated that after a continuous thermally grown chromia layer has formed, the permeation of hydrogen is reduced by four orders of magnitude. Despite having a thicker Cr_2O_3 layer on the fuel-side, the PVD Cr_2O_3 -coated sample suffers a similar level of corrosion as the uncoated sample. This indicates

that PVD-coated Cr₂O₃ is not sufficient to mitigate the dual-atmosphere corrosion effect. As discussed in Section 5.2.1.2, the exact mechanism by which hydrogen permeates an oxidised FSS is unknown. Nonetheless, it is commonly speculated that hydrogen permeates as protons through the Cr₂O₃ layer, while transport through the metal is attributed to atomic hydrogen transport [210, 211].

Therefore, to reduce further the dual-atmosphere effect, fuel-side coatings that have lower hydrogen permeation are necessary.

CeO₂ coatings are potential candidates as they carry several advantages. The presence of small amount of Ce is known to reduce the rate of oxide growth on chromia-forming alloys by changing the growth mechanism from outward diffusion of Cr to inward diffusion of oxygen [110, 113]. Grolig et al. [92] have shown that a thin layer of Ce drastically reduces the thickness of the Cr₂O₃ layer when exposed in air at 850 °C. Similarly, Alnegren et al. [212] has shown that a thin layer of Ce (~10 nm) can reduce the chromia thickness by approximately a factor of three after 4,500 h in Ar – 40 % H₂O – 3 % H₂ at 850 °C. In the present work, similar observations are made, as the thickness of the Cr₂O₃ layer present on the fuel-side of the CeO₂-coated sample is roughly half the thickness of the uncoated sample exposed under similar conditions, demonstrating a beneficial effect of the Ce. Another benefit of the CeO₂ coating, as discussed by Froitzheim et al. [191], is its ability to act as a diffusion barrier coating that prevents inter-diffusion between the FSS and the nickel-rich anode or the contact paste, preventing austenisation. Furthermore, as will be discussed in Section 5.2.3, CeO₂ displays good electrical conductivity in a low *p*O₂ environment [213, 214].

The use of YSZ as a hydrogen diffusion barrier is promising, as previous work [215] has shown that YSZ is an effective hydrogen barrier at high temperatures. Other research [216] has shown very low hydrogen permeation in a YSZ single crystal. Individually, yttria and zirconia when used as coatings display low hydrogen permeability. Previous research [217] on yttria-coated Eurofer steel showed excellent reduction of hydrogen permeation compared with the uncoated steel. Previous work carried out by Yen et al. [218] on the application of ZrO₂ coatings to AISI 430 showed a drastic reduction of hydrogen permeation compared with an uncoated sample. Previous work [219] performed hydrogen permeation tests on ZrO₂-coated (180 nm) AISI 430 and confirmed its excellent hydrogen barrier properties. In their work, they identified defects such as grain boundaries as permeation pathways for hydrogen in ZrO₂. However, as will be discussed further (see Section 5.2.3), the YSZ coating has very poor electronic conductivity, which makes its use challenging.

In this work, a thin Al₂O₃ coating shows the most-promising results in terms of a hydrogen diffusion barrier. As stated in Section 5.2.1.2, the most-desirable Al₂O₃ phase for application is expected to be α-Al₂O₃. Previous research [200, 204] has suggested that hydrogen diffusion in the corundum structure occurs between energy minima positions, preferentially along the c-axis, and has attributed the excellent hydrogen barrier properties of α-Al₂O₃ to Al vacancies that trap hydrogen. Nevertheless, α-Al₂O₃ is known to form at much higher temperatures (>1,000 °C), even if the formation of α-Al₂O₃ at lower temperatures (800 °C) has been reported

[220]. In a previous study [198], a similar PVD-sputtered Al_2O_3 oxide layer (~ 500 nm) was investigated using Grazing Incidence X-ray Diffractometry (GI-XRD). Since no sign of α - Al_2O_3 was found, the Al-oxide was considered amorphous. However, the use of Al_2O_3 is challenging, as it has poor electronic conductivity (see Section 5.2.3). A thicker Al_2O_3 scale might be beneficial in terms of further reducing the dual-atmosphere effect. This is discussed in the following section.

5.2.2.2 Aluminium oxide as hydrogen diffusion barrier

PVD alumina coatings represent the most-promising candidate coatings in terms of hydrogen diffusion barrier properties. In Section 5.2.2.1, it is described how a 30-nm Al_2O_3 -coated AISI 441 shows a low corrosion level (similar to the YSZ-coated sample) after 3,000 h of exposure, which is three-times longer than for the other fuel-side coatings investigated. Therefore, a range of PVD Al_2O_3 coatings were studied under similar exposure conditions.

Top-views of the air-sides of the Al_2O_3 -coated AISI 441 samples that were fuel-side coated are shown in Figure 5.13a-c. The SEM micrographs show the presence of Fe_2O_3 nodules of approximately 80 μm in diameter. Cross-sectional analysis of the air-side (see **Paper V**) show that all the samples have a thin Cr-rich oxide layer (<100 nm) covering the sample's surface.

Cross-sectional images of the fuel-sides of the Al_2O_3 -coated AISI 441 samples are shown in Figure 5.13g-i. All of the Al_2O_3 -coated samples show a homogeneous Al_2O_3 layer on top and a thin Cr_2O_3 layer (<100 nm). No signs of spallation of the oxide scale are evident in the 100-nm, 300-nm, and 600-nm Al_2O_3 -coated samples, indicating good adherence of the sputtered oxide. A thicker Al_2O_3 coating seems to have a beneficial effect, as fewer nodules are observed on the air-facing side of the samples the thicker the coating. Overall, after 3,000 h of exposure, the Al_2O_3 -coated AISI 441 samples exhibit very low corrosion levels.

Previous research [196] has demonstrated that pre-oxidation is beneficial for increasing the life-span of the interconnect under dual-atmosphere conditions. Therefore, PVD Al_2O_3 -coated AISI 441 samples were pre-oxidised for 5 h at 800 °C and exposed for 3,000 h at 600 °C under dual-atmosphere conditions (i.e., Atmosphere 1: 4.8 % H_2 + 3 % H_2O). This pre-oxidation step allows for the growth of a thicker Cr_2O_3 scale, possibly further hindering hydrogen diffusion. The top-view micrograph of the air-side of PVD Al_2O_3 -coated AISI 441 shows fewer Fe_2O_3 nodules after 3,000 h of exposure than was observed for the previous Al_2O_3 coatings (Figure 5.13d). These nodules are much smaller (~ 50 μm) than those of the previously investigated alumina coatings. The remainder of the sample surface is covered by a Cr-rich oxide. Cross-sectional analysis of the air-side, (see **Paper V**), reveals a thicker Cr_2O_3 scale (~ 200 nm), as compared with the sample that was pre-oxidised for 20 min, after exposure. Cross-sectional imaging of the fuel-side reveals a homogeneous Al-oxide layer together with a thin (~ 150 nm) Cr_2O_3 underneath (Figure 5.13j). The addition of a thicker chromia scale seems to be beneficial in reducing further the dual-atmosphere effect by slowing hydrogen ingress from the fuel-side. These results match the previous observations showing that longer pre-oxidation times lead to delayed onset of breakaway oxidation.

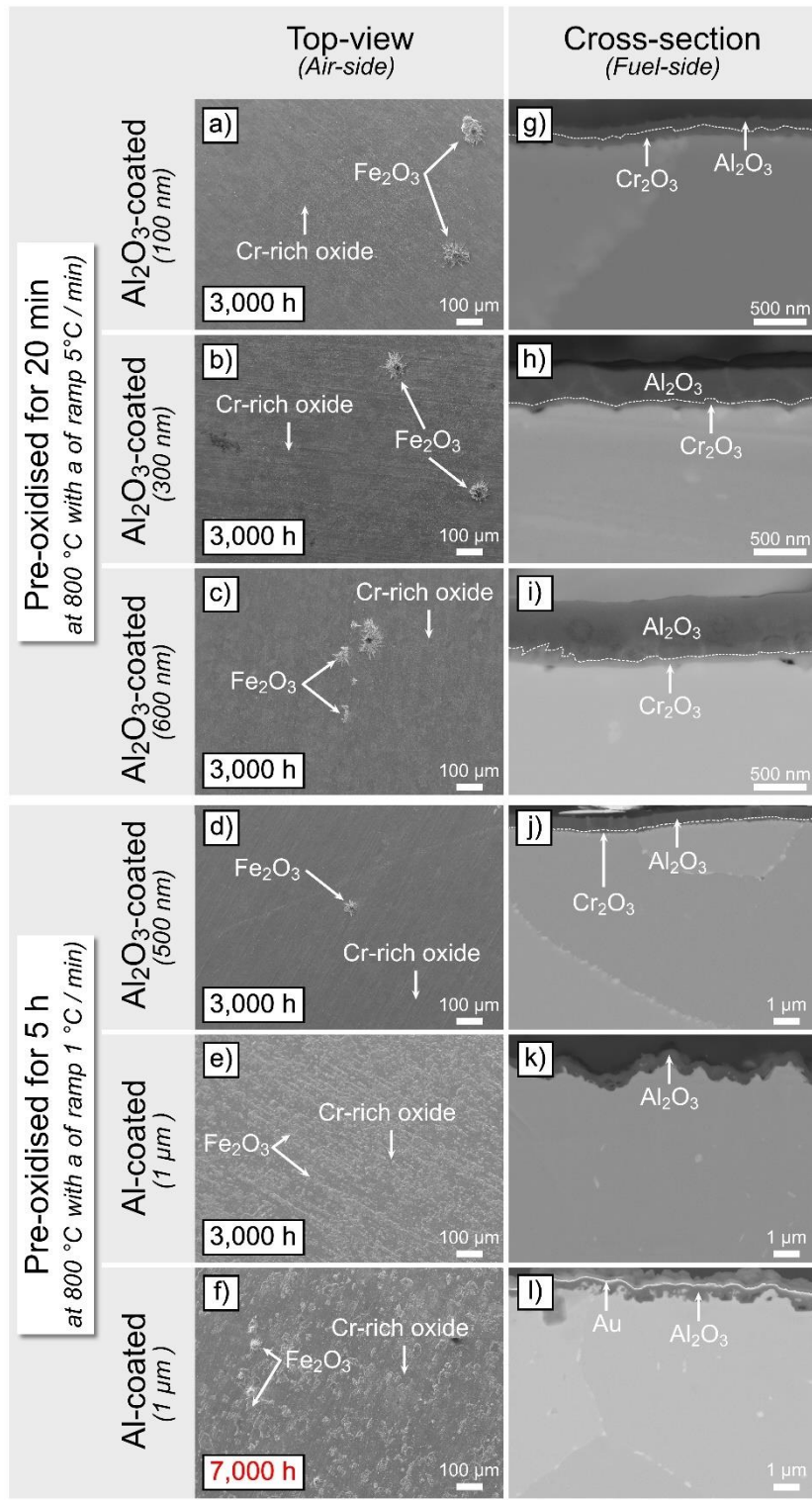


Figure 5.13: Top-view SEM micrographs of the air-side (a-f) and SEM cross-sectional micrographs of the fuel-side (g-l) of the investigated AISI 441 PVD Al_2O_3 -coated and Al-coated samples on the fuel-side, exposed under dual-atmosphere conditions (i.e., Atmosphere 1) at 600°C for up to 7,000 h.

The use of alumina might prove challenging, as the oxide on the pre-coated sheets can be damaged during the shaping of the interconnect or during the stack assembly process. It is, therefore, important to investigate the use of a conversion coating route similar to the Co coatings, as described in Section 3.2.2. The deposition, through the large-scale roll-to-roll

coating process [129], of metallic Al that oxidises to Al_2O_3 could be a cost-effective strategy, as well as a way to create an efficient hydrogen diffusion barrier.

The PVD Al-coated AISI 441 samples were pre-oxidised for 5 h at 800 °C. This procedure allows for the growth of a thicker Cr_2O_3 scale, reduced inter-diffusion of metallic Al into the steel substrate, and a potential reduction of metallic Al evaporation. A top-view micrograph of the air-side of the PVD Al-coated sample exposed for 3,000 h is depicted in Figure 5.13e. After 3,000 h of exposure, the sample displays small nodules that are aligned with the rolling direction of the steel sheet. These nodules were already evident after the pre-oxidation step (Figure 5.14a) and show minimal growth after exposure under dual-atmosphere conditions, indicating good hydrogen diffusion barrier properties of the Al-coating.

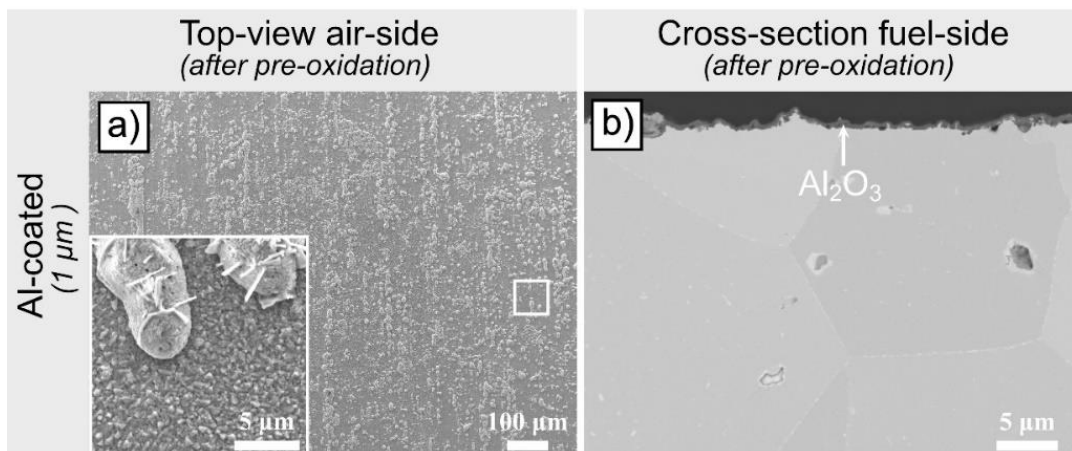


Figure 5.14: SEM micrographs of the air-side (Top-view) and fuel-side (Cross-section) of the PVD Al-coated AISI 441 after pre-oxidation for 5 h at 800 °C with a ramp rate of 1 °C/min, in air + 3 % H_2O .

The cross-sectional image of the fuel-side (Figure 5.13k) displays a wavy surface, although the layer thickness is homogeneous at around 500 nm. This morphology was observed already after the pre-oxidation step (Figure 5.14b). XRD analysis shows that the observed Al-rich oxide is the γ - Al_2O_3 phase (data not shown). The initial coating thickness was 1,000 nm, which upon oxidation to Al_2O_3 would have generated a layer thickness of around 1,300 nm. Therefore, some Al is “lost”, which will be discussed in detail below. No signs of spallation of the oxide scale were recorded for the sample, indicating good adherence of the oxidised coating. These observations prompted prolonged exposures (for up to 7,000 h). Figure 5.13f shows the top-view micrograph of the air-side of PVD Al-coated AISI 441 that was exposed for 7,000 h under identical conditions. A microstructure similar to that of the PVD Al-coated sample exposed for 3,000 h is observed. Nodules are observed along the rolling direction of the steel sheet. Some of the nodules seem to have grown and merged with the neighbouring nodules to form “patches” over time. However, this effect seems to be very limited. On top of these nodules, better-defined “whiskers-type” structures can be observed, corresponding to the Fe_2O_3 nodules commonly observed in previous studies [95, 144, 145, 147, 221]. The cross-sectional image of the fuel-side of PVD Al-coated AISI 441 (Figure 5.13l) shows a wavy Al-oxide scale on the fuel-side that resembles that on the previous Al-coated sample exposed for 3,000 h.

The initial Al thickness was 1,000 nm. However, after pre-oxidation, the observed thickness

was approximately 500 nm (Figure 5.14). The loss of Al is attributed to inter-diffusion between the coating and the steel substrate. To quantify this, a line-scan analysis was conducted on the PVD Al-coated 441 sample that was pre-oxidised for 5 h at 800 °C (Figure 5.15). The analysis reveals that Al has diffused into the alloy (to a depth of ~15 µm). Beneath the Al-rich surface layer, the Al concentration gradually decreases from 4 % to the detection limit of the EDS. The EDS line-scan also indicates the presence of Fe within the top layer (~10 at%). This proves that Al diffuses inside the alloy during the pre-oxidation step. Due to the slow heating rate, evaporation of metallic Al is considered unlikely, although it cannot be definitively ruled out.

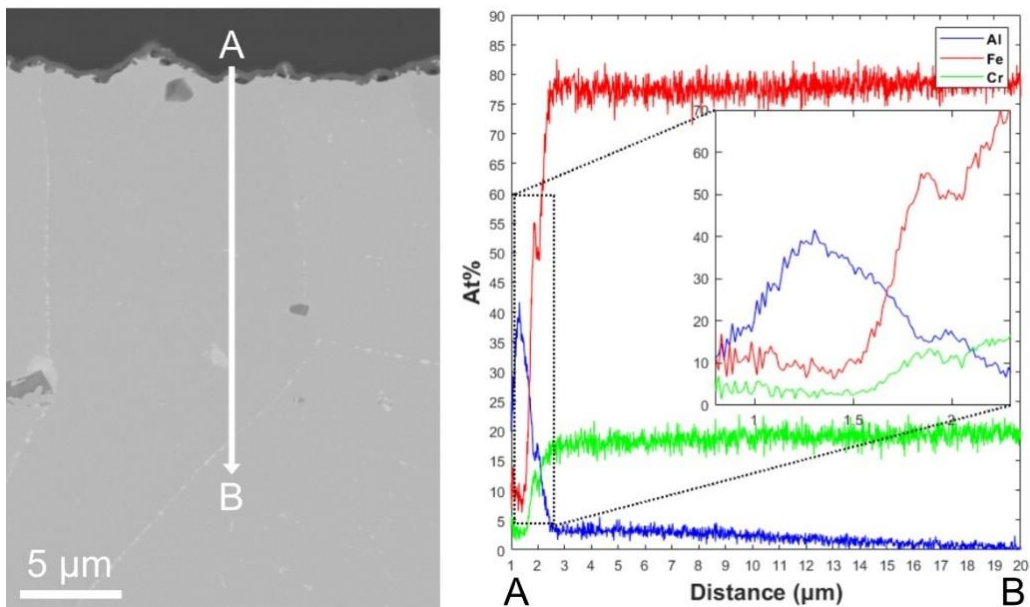


Figure 5.15: SEM micrograph representing the line-scan analysis used to determine the inter-diffusion of Al within the sample of an Al-coated AISI 441 sample exposed for 5 h in humid air (3 % H₂O) at 800 °C with up and down ramp rates of 1°C/min.

Metallic Al coatings exhibit, after oxidation, excellent hydrogen barrier properties, as after 7,000 h of exposure, the air-side morphology is almost unchanged. The growth of Fe-rich nodules/islands seems to occur mainly during the pre-oxidation step and once Al₂O₃ is formed, little corrosion degradation is observed. Metallic Al can be coated using the large-scale roll-to-roll coating process [129], making it an excellent candidate for cost-effective stack manufacturing.

5.2.2.3 Coating combinations

As stated in Section 3.2.2, a 600-nm Co layer combined with a thin 10-nm Ce layer represents an excellent coating system for use under single-atmosphere conditions, as it combines low Cr(VI) evaporation and good electrical properties, as described in Sections 5.1.4 and 5.1.5, respectively. Previous research [55, 118, 132] has reported similar results for PVD Ce/Co-coated steels exposed in this temperature range. Goebel et al. [222] exposed PVD Ce/Co-coated AISI 441 in stagnant laboratory air in a box furnace for up to 38,000 h. They showed that the coated steel exhibited protective behaviour even after approximately 4 years of exposure. The Cr(VI) evaporation, as well as the ASR values were within the acceptable

ranges [223]. However, PVD Ce/Co coatings have not been investigated under dual-atmosphere conditions for extended periods of time.

To address this gap in the knowledge, PVD Ce/Co-coated AISI 441 was exposed under dual-atmosphere conditions (i.e., Atmosphere 1) for 3,000 h (Figure 5.16). In the SEM micrographs, the air-side of the sample exhibits some Fe-rich nodules that are roughly 150 µm in diameter with whiskers on top, while the largest fraction of the sample's surface is covered by a protective oxide scale (Figure 5.16a). There are no signs of spallation of the oxide scale on the sample, indicating good adherence of the oxidised coating. The cross-sectional image of the air-side of the sample is shown in Figure 5.16b, with two different microstructures being evident: the nodules, and the protective scale. The nodules consist of three distinct layers. The top layer comprises an $(\text{Fe},\text{Co})_3\text{O}_4$ spinel. EDS analysis shows that the top layer contains Fe (~20 at%), Co (~10 at%), and a low percentage of Cr (~5 at%). In this case, it appears that the Fe diffused within the oxide scale even in the presence of a Ce layer. Underneath this layer, an Fe-rich oxide with thickness of approximately 20 µm is observed. Underneath the original sample surface, there is an $(\text{Fe},\text{Cr})_3\text{O}_4$ spinel with thickness similar to that of the Fe-rich oxide phase observed previously. The overall thickness of the nodules is approximately 40 µm. The nodules are fewer but more localised and thicker than those observed in uncoated samples (Figure 5.12a). The protective oxide scale comprises a very thin (~100 nm) $(\text{Co},\text{Cr})_3\text{O}_4$ spinel on top, which contains 10 at% Co and 10 at% Cr, followed by 1-µm-thick Co_3O_4 spinel with a thin (~200 nm) Cr_2O_3 layer. The presence of Cr in the top layer is attributed to Cr(VI) evaporation from the sample holder, which is composed of 253MA steel. Skilbred et al. [221] observed similar cubic-shaped grains on the top layer of Ce/Co-coated samples exposed under dual-atmosphere conditions at 850 °C. Moreover, in their study, the cross-sectional image depicted a thin Co_3O_4 layer followed by a thin Cr_2O_3 oxide scale. However, there were no signs of Fe-rich nodules. This is mainly attributed to the less-severe dual-atmosphere effect at high temperatures, as well as the short exposure time (150 h), which did not allow sufficient time for the breakaway oxidation to happen [21].

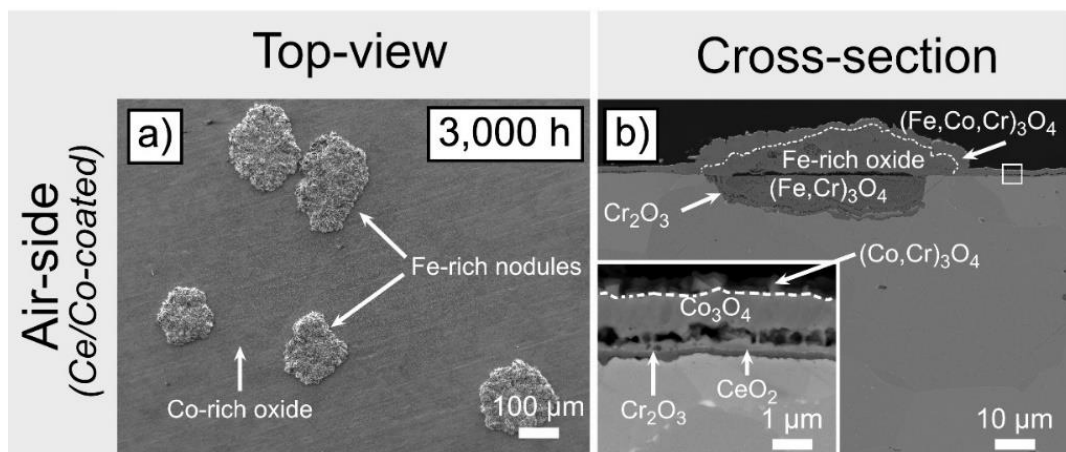


Figure 5.16: Top-view and cross-sectional SEM micrographs of the investigated AISI 441 PVD Ce/Co-coated sample on the air-side, exposed under dual-atmosphere conditions (i.e., Atmosphere 1) at 600 °C for 3,000 h. Inset: Higher-magnification image of selected scale regions.

These observations indicate the somewhat better resistance to the dual-atmosphere effect of the PVD Ce/Co-coated sample, as compared with the uncoated sample. It has been shown that regardless of whether the top layer is Co_3O_4 , $(\text{Co}, \text{Mn})_3\text{O}_4$ or $(\text{Co}, \text{Mn}, \text{Fe})_3\text{O}_4$, the Cr(VI) evaporation rates at 600 °C and 650 °C are significantly lower for PVD Ce/Co-coated materials than for uncoated Fe-Cr steel. Thus, the depletion of Cr over time is less-extensive, which is expected to result in less-severe breakaway oxidation.

The use of a PVD Ce/Co coating on the air-facing side of the sample results in more-localised breakaway oxidation than in the uncoated samples, although the sample still suffers from the dual-atmosphere effect after long-term exposure. As shown in Section 5.2.2.1, fuel-side coatings are essential as barriers against hydrogen permeation. Metallic Al and Al_2O_3 coatings are proven to be highly effective owing to their low hydrogen permeability. Therefore, a PVD Ce/Co coating on the air-side and an Al coating on the fuel-side of AISI 441 were investigated for up to 7,000 h under dual-atmosphere conditions (i.e., Atmosphere 1).

The top-view SEM micrograph of the air-side of the sample (Figure 5.17a) shows the presence of a few large Fe-rich nodules, comparable to the nodules observed on the PVD Ce/Co-coated samples (Figure 5.16a). The nodules are of equivalent size, albeit less frequent. Smaller nodules are visible, seem to be covered by an oxide scale, and follow the rolling direction of the steel sheet. Those features were observed already after pre-oxidation (data not shown).

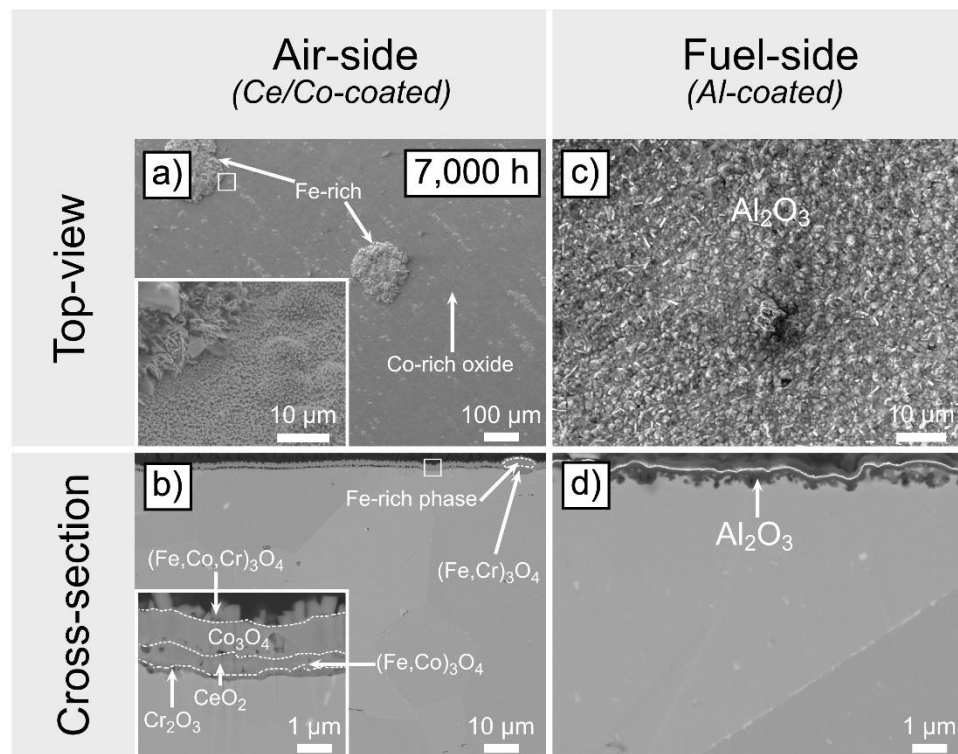


Figure 5.17: Top-view and cross-sectional SEM micrographs of the investigated AISI 441 PVD Al//Ce/Co-coated sample, exposed under classic dual-atmosphere conditions (i.e., Atmosphere 1) at 600 °C for 7,000 h. Inset: Higher-magnification image of selected scale regions. An Au-layer was sputtered on the fuel-side to enhance the contrast of the cross-section.

The cross-sectional image of the air-side (see Figure 5.17b) reveals two different microstructures: a homogeneous four-layer microstructure and a small-nodule microstructure. The outer layer of the homogeneous part consists of a $(\text{Cr}, \text{Co})_3\text{O}_4$ spinel that contains approximately 19 at% Cr and 15 at% Co. The Cr in the top layer is believed to originate from the sample holder, as discussed previously. The second layer consists of an almost-pure Co_3O_4 spinel that contains roughly 4 at% Fe. The third layer is a $(\text{Fe}, \text{Co})_3\text{O}_4$ spinel with 14 at% Fe, 14 at% Co, and low percentages of Cr and Mn (6 at% and 3 at%, respectively). Closest to the metal, a thin Cr_2O_3 layer is present. Overall, this four-layer microstructure appears to be porous and is roughly 1 μm in thickness. The second part consists of Fe-rich, small nodules located underneath a $(\text{Co}, \text{Cr})_3\text{O}_4$ spinel, and beneath this, a $(\text{Fe}, \text{Cr})_3\text{O}_4$ spinel is present. The top-view of the fuel-side (Figure 5.17c) does not show visible signs of severe corrosion, and has the same morphology as observed after the pre-oxidation step. The Al-rich layer is homogeneous and covers the sample. The cross-sectional image of the fuel-side (Figure 5.17d) depicts a wavy and irregular Al_2O_3 scale, similar to the one observed for the Al-coated sample (Figure 5.13l). The oxide scale is much thinner than the nominal coating thickness (1,000 nm), and it is attributed to Al inter-diffusion, as described in Section 5.2.2.2.

The coating combination of Al on the fuel-side and Ce/Co on the air-side is proven to be efficient and, consequently, it reduces the dual-atmosphere effect. Despite the thickness reduction noted during the pre-oxidation stage, due to Al diffusion within the bulk, the thin Al_2O_3 layer acts as a barrier to hydrogen diffusion. The Ce/Co coating on the air-side of the sample is the optimal candidate for Cr(VI) mitigation, providing additional protection against corrosion. Figure 5.18 shows an overview of the PVD Al- and Al//Ce/Co-coated samples that were exposed for up to 7,000 h at 600 °C under dual-atmosphere conditions. After 3,000 h, the PVD Ce/Co-coated AISI 441 sample exhibits greater corrosion degradation than the PVD Al//Ce/Co-coated sample. After 7,000 h of exposure, the PVD Al//Ce/Co-coated sample shows less corrosion than the PVD Ce/Co-coated steel after 3,000 h. These outcomes are in accordance with previous observations, and underline the importance of coatings on the fuel-side to prevent the dual-atmosphere effect.

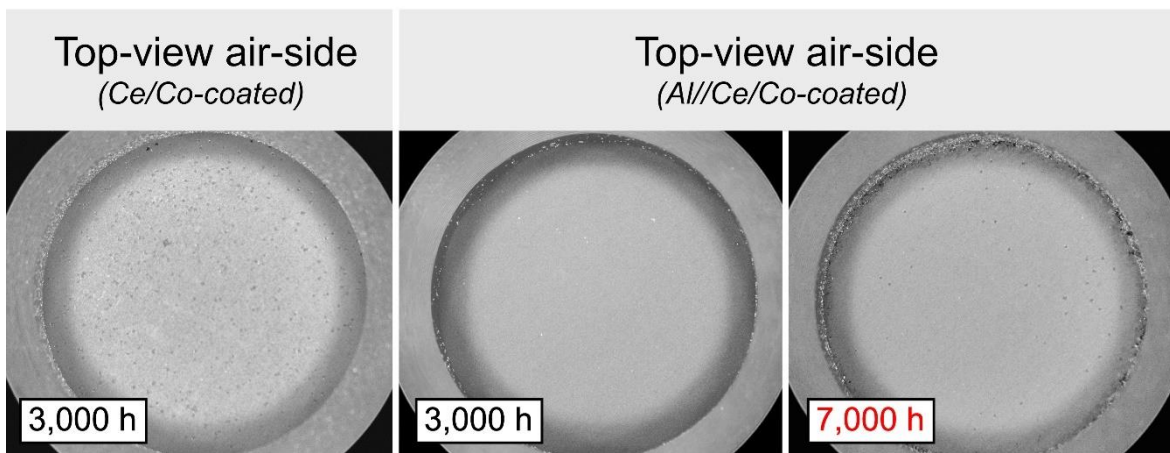


Figure 5.18: Optical images of the air-side of the Al- and Al//Ce/Co-coated AISI 441 samples exposed for up to 7,000 h at 600 °C under dual-atmosphere conditions.

5.2.3 ASR evaluation of the coatings – *Suitability for interconnect applications*

The electrical conductivity of the coated interconnect directly impacts the eventual performance of FC. Therefore, the resistance must be kept as low as possible, and it should increase as little as possible over time. An ASR value of $<100 \text{ m}\Omega\cdot\text{cm}^2$ is commonly reported as an acceptable threshold for ASR [223], although as low values as possible are desirable. The ASR measurements performed in humid Ar – 5 % H₂ for uncoated, and CeO₂--, YSZ-, Al₂O₃-, and Al-coated samples exposed for up to 500 h at 600 °C are reported in Figure 5.19. Uncoated samples exhibit an ASR of 15 mΩ·cm² on average, while Cr₂O₃-coated samples exhibit an ASR of 30 mΩ·cm² on average. This correlates with the previous observations of Goebel et al. [55], who reported that the Cr₂O₃ layer is the main contributor to ASR.

Uncoated samples exhibit a Cr₂O₃ layer that is approximately 100 nm in thickness, while Cr₂O₃-coated samples display an oxide layer that is 200 nm in thickness. This approximately two-fold increase in thickness matches the increased ASR values.

The CeO₂-coated samples exhibit an ASR value of approximately 16 mΩ·cm². Previous studies [213, 214] have shown that at low *p*O₂, CeO₂ becomes an n-type semi-conductor with substantial electronic conductivity. Previous research [213, 224] has found that at 600 °C, pure CeO₂ exhibits a higher conductivity than Cr₂O₃ under the same conditions [63]. The measured ASR values are, therefore, mainly determined by the Cr₂O₃ layer, as stated in Section 5.1.5. The CeO₂-coated samples exhibit a chromia layer thickness of <100 nm, which corresponds approximately to the thickness observed for the uncoated sample, so similar ASR values are expected.

The YSZ-coated samples exhibit much higher ASR values than the CeO₂-coated samples. YSZ is a rather poor electronic conductor [225], which is why it is used as an electrolyte material. The YSZ-coated samples exhibit 3 – 4-times higher ASR values than the CeO₂-coated samples.

Alumina is known to be an electronic insulator [61, 193, 226], and the PVD Al₂O₃-coated (≥ 100 nm) samples accordingly show prohibitively high ASR values. Interestingly, the PVD 30-nm Al₂O₃-coated samples have only slightly higher ASR values than the uncoated and CeO₂-coated samples. This finding is attributed to the fact that pinholes in the coating provide high-conductivity pathways. For the Al-coated samples, an ASR value of about 75 mΩ·cm² was measured, which is lower than the commonly cited target of 100 mΩ·cm². The reason for the relatively low ASR value may be the presence of impurities within the oxide scale. As described in Section 5.2.2.2, Al diffuses during pre-oxidation and only half of the coating oxidises to Al₂O₃ (~500 nm). The ASR values are much lower than for the PVD 600-nm Al₂O₃-coated sample, and this is attributed in part to the lower thickness, but mostly due to the fact that Fe is incorporated into the Al-rich layer. An aliovalent ion such as Fe is expected to improve the electronic conductivity significantly. However, this ASR value was obtained after

1 week and it is currently uncertain as to whether the ASR target can be met during long-term operation.

The investigated coatings reveal that a trade-off between hydrogen barrier properties and increased ASR is required. The use of Al_2O_3 , either from the conversion route or deposited directly using PVD, at a thickness >100 nm seems challenging for use as a coating for SOFC interconnect applications, as it shows high ASR values due to its poor electronic conductivity. However, a thin Al_2O_3 coating (~ 30 nm) may provide sufficient protection against corrosion, even while accruing an acceptable ASR penalty. In addition, the CeO_2 coating greatly reduces the dual-atmosphere effect, as compared to the uncoated and the Cr_2O_3 -coated materials. Furthermore, CeO_2 is a reasonably good electronic conductor at 600 °C and at low $p\text{O}_2$.

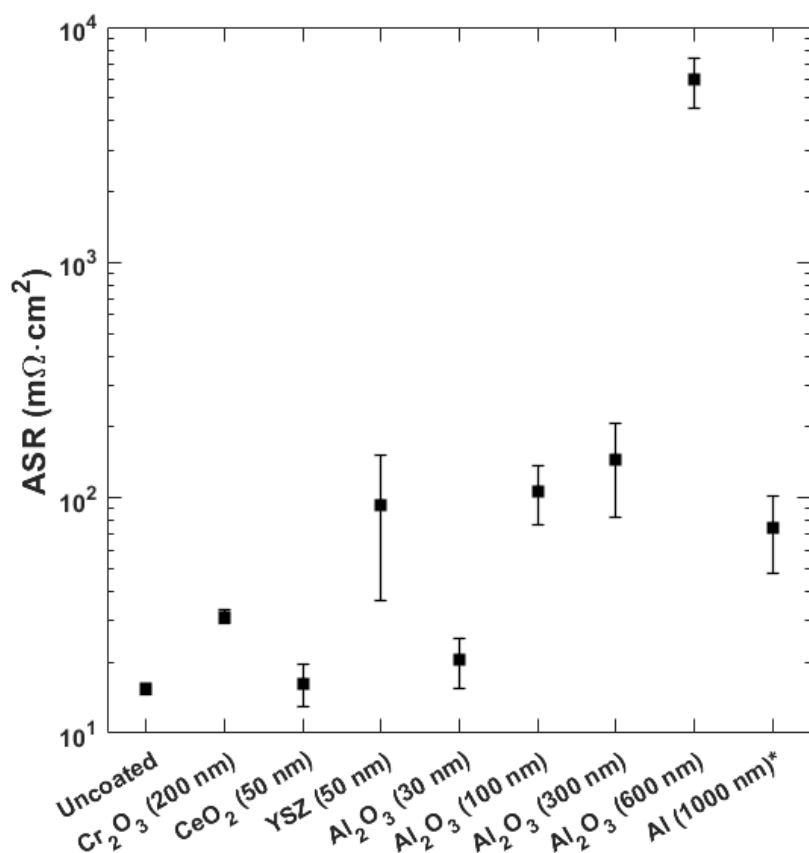


Figure 5.19: ASR measurements performed in humid H_2 at 600 °C on uncoated, Cr_2O_3 -coated, CeO_2 -coated, YSZ-coated, Al_2O_3 -coated, and Al-coated samples exposed for **500 h** in Ar – 4.8 % H_2 + 3 % H_2O . The uncoated side of the sample was ground so as to have the ASR contribution of the coating only. The error bars represent the standard deviation. *Al-coated samples were exposed for **168 h** in Ar – 4.8 % H_2 + 3 % H_2O .

6. Summary & Outlook

"I never see what has been done; I only see what remains to be done."

– Marie Curie

The present work has examined the degradation of FSS interconnects with respect to two main aspects. First, the uncoated, PVD-coated, and TS-coated alloys were exposed under single-atmosphere conditions, and their influences on the degradation of the interconnects were analysed. Second, the dual-atmosphere effect itself and strategies to mitigate it were investigated.

Uncoated alloys, with the exception of the non-pre-oxidised AISI 430, perform well in single-atmosphere experiments. The Cr₂O₃-forming steels exhibit small variations in oxidation kinetics and Cr(VI) evaporation and present similar ASR values. The Al₂O₃-forming alloy, Kanthal EF 101, displays an extremely low Cr(VI) evaporation but much higher ASR values due to the presence of an Al₂O₃ layer. These experiments suggest modest differences between the Cr₂O₃-forming steels, in terms of their applicability to IT-SOFCs.

PVD and TS coatings, specifically Cu-based coatings, were analysed with regard to three main factors: Cr(VI) evaporation, microstructure, and overall ASR value. This work shows that the PVD Ce/Cu and TS Mn/Co coatings are as effective as PVD Ce/Co coatings at 650 °C, in terms of Cr(VI) vaporisation and ASR values (<15 mΩ·cm²). However, the PVD Ce/Mn-Cu, TS Cu, and Mn/Cu coatings exhibit nodules or thick intermediate Fe-rich layers, which may be attributed to the presence of Mn or the lack of a CeO₂ layer. The PVD Ce/Cu coating is a strong candidate to replace the PVD Ce/Co coating, as it offers a low Cr(VI) evaporation and thin, adherent, and conductive oxide scales.

The second part of the thesis investigates the dual-atmosphere effect with regard to the following parameters: steel composition, fuel gas composition, and fuel-side coatings i.e., hydrogen barriers.

It is shown that all Cr₂O₃-forming alloys suffer some breakaway corrosion under dual-atmosphere conditions, which is attributed to the low exposure temperature (600 °C), which impedes Cr diffusion. The Al₂O₃-forming alloy (Kanthal EF 101) demonstrates the best behaviour towards the dual-atmosphere effect, as the alloy remains protective after exposure. Furthermore, it is demonstrated that alloys that contain large amounts of Laves phase precipitates seem to suffer from a more-severe dual-atmosphere effect.

Summary & Outlook

The gas composition on the fuel-side is shown to impact significantly the extent of the breakaway oxidation on the air-side of the steel. The higher the concentration of hydrogen on the fuel-side, the more corrosion occurs on the air-side. However, a significant difference is observed between a specifically designed commercial steel, such as Crofer 22 APU, and a cheaper commercial steel, such as AISI 441. Thus, Crofer 22 APU sustains a harsher fuel gas atmosphere more effectively than AISI 441, as a significant difference in corrosion degradation on the air-side is observed. The Al₂O₃-former shows almost no signs of breakaway oxidation after exposure to 97 % H₂, indicating the ability of the alumina layer to act as a hydrogen barrier. Based on the conclusions drawn above, coatings on the fuel-side of the sample seem to be necessary to effectively hinder hydrogen diffusion through the steel.

Different fuel-side coating systems were investigated, including Cr₂O₃, CeO₂, YSZ, Al and Al₂O₃. This work finds that despite having a lower hydrogen permeation than Fe-Cr steel, PVD-coated Cr₂O₃ is not able to reduce sufficiently the hydrogen diffusion so as to avoid breakaway oxidation over time, and after 1,000 h of exposure, corrosion levels similar to those seen in uncoated samples are observed. Nonetheless, CeO₂ shows good hydrogen barrier properties, as well as low ASR values. The coating systems with the best hydrogen barrier properties are found to be the Al-based coatings, produced either through conversion of metallic Al to Al₂O₃ or direct deposition of Al₂O₃. This work shows that a trade-off between hydrogen barrier properties and increased ASR value is required. In this context, the best results are obtained with a very thin Al₂O₃ layer (~30 nm). Low corrosion levels are found on the air-facing of the samples after 3,000 h of exposure and reasonably low ASR values are measured despite the presence of Al₂O₃. These results indicate that CeO₂-based coatings or very thin Al₂O₃ coatings are promising candidates for fuel-side coatings.

As stated previously, the two major issues related to metallic interconnects are: Cr(VI) evaporation, and the dual-atmosphere effect. To mitigate these phenomena, combinations of coatings are necessary. This work reveals that coupling a PVD Ce/Co coating on the air-side with a metallic Al coating on the fuel-side represents an promising strategy for combating Cr(VI) evaporation and the dual-atmosphere effect even during 7,000 h of exposure, as low corrosion levels are observed on the air-side of the sample, while providing cost-efficient coating process for mass production.

Future outlook

Considerable efforts have been made in this thesis to evaluate and mitigate two major issues related to metallic interconnects. This has yielded a deeper understanding of how hydrogen affects the air-side of the interconnect and how the steel composition might affect hydrogen permeability. Novel mitigation strategies are investigated and show promising results in terms of extending further the interconnect life-span.

Therefore, additional research related to these findings would contribute to improving significantly this technology. It is expected that more research will be performed as these technologies (SOFCs and SOECs) emerge and become commercialised world-wide.

Future relevant research should focus on the following objectives:

- **Coating development and optimisation:** Cu-based coatings show promising results at low temperatures under single-atmosphere conditions. However, these coatings have not been investigated under dual-atmosphere conditions. It would be interesting to study different combinations of Cu-based coatings under such experimental conditions, to assess their suitability for IT-SOC applications.
The use of metallic Al shows promising results and could be cost-effective, although Al inter-diffusion leads to a drastic reduction of the coating thickness after heat treatment. The use of an intermediate barrier layer, such as Ce or yttria, might solve this problem.
- **The effect of the Laves phases under dual-atmosphere conditions:** The potential effect of Laves phases should be investigated further with model alloys that contain specific amounts of Si and Nb, to obtain a matrix with increasing Laves phases concentrations. These alloys should be annealed identically, to obtain the same grain size. The alloy with higher Laves phases concentration is expected to exhibit more-severe corrosion.
- **Understanding the mechanism underlying the dual-atmosphere effect:** A higher concentration of hydrogen in the fuel gas clearly accelerates breakaway oxidation on the air-facing side of the sample. Studying hydrogen permeation on the fuel-side is crucial for understanding the dual-atmosphere effect mechanism, and for identifying optimal mitigation strategies. One possibility is to use neutron scattering to measure hydrogen within the steel after or during exposure.
Another way could be to use an isotope, such as deuterium, as a tracer to investigate the effects that alloying elements, secondary phases, and surface treatments have on the diffusion of hydrogen.
- **The effect of current on the oxidation behaviour of the steel:** The literature reports a change in the nature and microstructure of an oxide when exposed to a current. One avenue of research could involve exposures under single-atmosphere and dual-atmosphere conditions in the presence of a flow of current.

References

1. Hannah, R., R. Max and R. Pablo. "CO₂ and Greenhouse Gas Emissions". 2020. OurWorldInData.org.
2. Armstrong McKay, D.I., A. Staal, J.F. Abrams, R. Winkelmann, B. Sakschewski, S. Loriani, I. Fetzer, S.E. Cornell, J. Rockström, and T.M. Lenton, *Exceeding 1.5 C global warming could trigger multiple climate tipping points*. Science, 2022. **377**(6611): p. eabn7950 DOI: <https://doi.org/10.1126/science.abn7950>.
3. Friedlingstein, P., M. O'sullivan, M.W. Jones, R.M. Andrew, L. Gregor, J. Hauck, C. Le Quéré, I.T. Luijkx, A. Olsen, and G.P. Peters, *Global carbon budget 2022*. Earth System Science Data Discussions, 2022. **2022**: p. 1-159 DOI: <https://doi.org/10.5194/essd-14-4811-2022>.
4. Hannah, R., R. Max and R. Pablo. "Energy". 2023. Available from: <https://ourworldindata.org/energy>.
5. Chen, T., Y. Jin, H. Lv, A. Yang, M. Liu, B. Chen, Y. Xie, and Q. Chen, *Applications of lithium-ion batteries in grid-scale energy storage systems*. Transactions of Tianjin University, 2020. **26**(3): p. 208-217 DOI: <https://doi.org/10.1007/s12209-020-00236-w>.
6. Yang, X., C.P. Nielsen, S. Song and M.B. McElroy, *Breaking the hard-to-abate bottleneck in China's path to carbon neutrality with clean hydrogen*. Nature Energy, 2022. **7**(10): p. 955-965 DOI: <https://doi.org/10.1038/s41560-022-01114-6>.
7. CO₂ emissions by sectors 2023. OurWorldInData.org. <https://ourworldindata.org/grapher/co-emissions-by-sector>
8. Riera, J.A., R.M. Lima and O.M. Knio, *A review of hydrogen production and supply chain modeling and optimization*. International Journal of Hydrogen Energy, 2023 DOI: <https://doi.org/10.1016/j.ijhydene.2022.12.242>.
9. Energy, D.-G.f. *Hydrogen*. [European Commision] 2023. Available from: https://energy.ec.europa.eu/topics/energy-systems-integration/hydrogen_en#renewable-hydrogen.
10. Gasunie. *What is hydrogen and how is it made?* 2023. Available from: <https://www.dewereldvanwaterstof.nl/gasunie/wat-is-waterstof?UA-142619432-2=>.
11. Institute, B.M., *Manufacturing cost analysis of 100 and 250 kW fuel cell systems for primary power and combined heat and power applications*. 2016, United States Department of Energy Golden: Department of Energy. p. 1-289. Available from: https://www.energy.gov/search/site?keywords=battelle&sort_by=search_api_relevance&f%5B0%5D=offices%3AHydrogen%20and%20Fuel%20Cell%20Technologies%20Office.
12. Institute, B.M., *Manufacturing Cost Analysis of 1, 5, 10 and 25 kW Fuel Cell Systems for Primary Power and Combined Heat and Power Applications* 2017, United States Department of Energy Golden: Department of Energy. p. 293. Available from: https://www.energy.gov/search/site?keywords=battelle&sort_by=search_api_relevance&f%5B0%5D=offices%3AHydrogen%20and%20Fuel%20Cell%20Technologies%20Office.
13. Smith, L., T. Ibn-Mohammed, F. Yang, I.M. Reaney, D.C. Sinclair and S.L.J.A.E. Koh, *Comparative environmental profile assessments of commercial and novel material structures for solid oxide fuel cells*. 2019. **235**: p. 1300-1313 DOI: <https://doi.org/10.1016/j.apenergy.2018.11.028>.
14. Brandon, N., E. Ruiz-Trejo and P. Boldrin, *Solid Oxide Fuel Cell Lifetime and*

References

- Reliability: Critical Challenges in Fuel Cells.* 2017.
15. Stambouli, A.B. and E. Traversa, *Solid oxide fuel cells (SOFCs): a review of an environmentally clean and efficient source of energy.* Renewable and Sustainable Energy Reviews, 2002. **6**(5): p. 433-455 DOI: [https://doi.org/10.1016/S1364-0321\(02\)00014-X](https://doi.org/10.1016/S1364-0321(02)00014-X).
16. Mukerjee, S., R. Leah, M. Selby, G. Stevenson and N.P. Brandon, *Chapter 9 - Life and Reliability of Solid Oxide Fuel Cell-Based Products: A Review*, in *Solid Oxide Fuel Cell Lifetime and Reliability*, N.P. Brandon, E. Ruiz-Trejo, and P. Boldrin, Editors. 2017, Academic Press. p. 173-191 DOI: <https://doi.org/10.1016/B978-0-08-101102-7.00009-X>.
17. Menzler, N.H. and L. Blum. *High-Temperature Fuel Cell Achieves Lifetime of More Than 11 Years.* [Forschungszentrum Jülich] 2019. Available from: <https://www.fz-juelich.de/en/news/archive/press-release/2019/2019-02-07-sofc-en?expand=translations,fzjsettings,nearest-institut>.
18. Shaigan, N., W. Qu, D.G. Ivey and W. Chen, *A review of recent progress in coatings, surface modifications and alloy developments for solid oxide fuel cell ferritic stainless steel interconnects.* Journal of Power Sources, 2010. **195**(6): p. 1529-1542 DOI: <https://doi.org/10.1016/j.jpowsour.2009.09.069>.
19. Quadakkers, W., J. Piron-Abellán, V. Shemet and L. Singheiser, *Metallic interconnectors for solid oxide fuel cells—a review.* Materials at high temperatures, 2003. **20**(2): p. 115-127 DOI: <https://doi.org/10.1179/mht.2003.015>.
20. Alnegren, P., M. Sattari, J.-E. Svensson and J. Froitzheim, *Temperature dependence of corrosion of ferritic stainless steel in dual atmosphere at 600–800 C.* Journal of Power Sources, 2018. **392**: p. 129-138 DOI: <https://doi.org/10.1016/j.jpowsour.2018.04.088>.
21. Gunduz, K.O., A. Chyrkin, C. Goebel, L. Hansen, O. Hjorth, J.-E. Svensson, and J. Froitzheim, *The effect of hydrogen on the breakdown of the protective oxide scale in solid oxide fuel cell interconnects.* Corrosion Science, 2021. **179**: p. 109112 DOI: <https://doi.org/10.1016/j.corsci.2020.109112>.
22. Grove, W.R., *LVI. On a new voltaic combination: To the editors of the Philosophical Magazine and Journal.* The London, Edinburgh, and Dublin Philosophical Magazine and Journal of Science, 1838. **13**(84): p. 430-431 DOI: <https://doi.org/10.1080/14786443808649618>.
23. Grove, W.R., *XXIV. On voltaic series and the combination of gases by platinum.* The London, Edinburgh, and Dublin Philosophical Magazine and Journal of Science, 1839. **14**(86-87): p. 127-130 DOI: <https://doi.org/10.1080/14786443908649684>.
24. Schönbein, C.F., X. *On the voltaic polarization of certain solid and fluid substances: To the editors of the Philosophical Magazine and Journal.* The London, Edinburgh, and Dublin Philosophical Magazine and Journal of Science, 1839. **14**(85): p. 43-45 DOI: <https://doi.org/10.1080/14786443908649658>.
25. Srinivasan, S., *Fuel cells: from fundamentals to applications.* 1 ed. 2006: Springer New York, NY. 662 DOI: <https://doi.org/10.1007/0-387-35402-6>.
26. Kirubakaran, A., S. Jain and R. Nema, *A review on fuel cell technologies and power electronic interface.* Renewable and Sustainable Energy Reviews, 2009. **13**(9): p. 2430-2440 DOI: <https://doi.org/10.1016/j.rser.2009.04.004>.
27. Hansen, J.B. and N. Christiansen, *Solid Oxide Fuel Cells, Marketing Issues*, in *Fuel Cells: Selected Entries from the Encyclopedia of Sustainability Science and Technology*, K.-D. Kreuer, Editor. 2013, Springer New York: New York, NY. p. 687-730 DOI: https://doi.org/10.1007/978-1-4614-5785-5_20.
28. Steinberger-Wilckens, R., *Introduction to Fuel Cell Basics*, in *Advances in Medium and High Temperature Solid Oxide Fuel Cell Technology*, M. Boaro and A.A. Salvatore,

- Editors. 2017, Springer International Publishing: Cham. p. 1-29 DOI: https://doi.org/10.1007/978-3-319-46146-5_1.
29. de Frank Bruijn, A. and G.J.M. Janssen, *PEM Fuel Cell Materials: Costs, Performance, and Durability*, in *Fuel Cells and Hydrogen Production: A Volume in the Encyclopedia of Sustainability Science and Technology, Second Edition*, T.E. Lipman and A.Z. Weber, Editors. 2019, Springer New York: New York, NY. p. 195-234 DOI: https://doi.org/10.1007/978-1-4939-7789-5_152.
30. Wang, Y., K.S. Chen, J. Mishler, S.C. Cho and X.C. Adroher, *A review of polymer electrolyte membrane fuel cells: Technology, applications, and needs on fundamental research*. Applied energy, 2011. **88**(4): p. 981-1007 DOI: <https://doi.org/10.1016/j.apenergy.2010.09.030>.
31. Naimaster, E.J. and A.K. Sleiti, *Potential of SOFC CHP systems for energy-efficient commercial buildings*. Energy and Buildings, 2013. **61**: p. 153-160 DOI: <https://doi.org/10.1016/j.enbuild.2012.09.045>.
32. Staffell, I., A. Ingram and K. Kendall, *Energy and carbon payback times for solid oxide fuel cell based domestic CHP*. International Journal of Hydrogen Energy, 2012. **37**(3): p. 2509-2523 DOI: <https://doi.org/10.1016/j.ijhydene.2011.10.060>.
33. Ni, M., M.K. Leung and D.Y. Leung, *Technological development of hydrogen production by solid oxide electrolyzer cell (SOEC)*. International journal of hydrogen energy, 2008. **33**(9): p. 2337-2354 DOI: <https://doi.org/10.1016/j.ijhydene.2008.02.048>.
34. Scherer, G.G., *Fuel Cell Types and Their Electrochemistry*, in *Fuel Cells and Hydrogen Production: A Volume in the Encyclopedia of Sustainability Science and Technology, Second Edition*, T.E. Lipman and A.Z. Weber, Editors. 2019, Springer New York: New York, NY. p. 83-98 DOI: https://doi.org/10.1007/978-1-4939-7789-5_132.
35. Scott, K., *Introduction to Electrolysis, Electrolysers and Hydrogen Production*, in *Electrochemical Methods for Hydrogen Production*, K. Scott, Editor. 2019, The Royal Society of Chemistry. p. 0 DOI: <https://doi.org/10.1039/9781788016049-00001>.
36. Jolaoso, L.A., I.T. Bello, O.A. Ojelade, A. Yousuf, C. Duan and P. Kazempoor, *Operational and scaling-up barriers of SOEC and mitigation strategies to boost H₂ production- a comprehensive review*. International Journal of Hydrogen Energy, 2023. **48**(85): p. 33017-33041 DOI: <https://doi.org/10.1016/j.ijhydene.2023.05.077>.
37. Gómez, S.Y. and D. Hotza, *Solid Oxide Electrolysers*, in *Electrochemical Methods for Hydrogen Production*, K. Scott, Editor. 2019, The Royal Society of Chemistry. p. 0 DOI: <https://doi.org/10.1039/9781788016049-00136>.
38. Winkler, W., *Chapter 3 - Thermodynamics*, in *High Temperature and Solid Oxide Fuel Cells*, S.C. Singhal and K. Kendall, Editors. 2003, Elsevier Science: Amsterdam. p. 53-82 DOI: <https://doi.org/10.1016/B978-185617387-2/50020-9>.
39. Andrew L. Dicks, D.A.J.R., *Solid Oxide Fuel Cells*, in *Fuel Cell Systems Explained*. 2018. p. 235-261 DOI: <https://doi.org/10.1002/9781118706992.ch9>.
40. Ji, Y., J.A. Kilner and M.F. Carolan, *Electrical properties and oxygen diffusion in yttria-stabilised zirconia (YSZ)-La_{0.8}Sr_{0.2}MnO₃±δ (LSM) composites*. Solid State Ionics, 2005. **176**(9): p. 937-943 DOI: <https://doi.org/10.1016/j.ssi.2004.11.019>.
41. Yang, C.-C.T., W.-C.J. Wei and A. Roosen, *Electrical conductivity and microstructures of La_{0.65}Sr_{0.3}MnO₃-8mol% yttria-stabilized zirconia*. Materials Chemistry and Physics, 2003. **81**(1): p. 134-142 DOI: [https://doi.org/10.1016/S0254-0584\(03\)00158-5](https://doi.org/10.1016/S0254-0584(03)00158-5).
42. Minh, N.Q., *Ceramic fuel cells*. Journal of the American Ceramic Society, 1993. **76**(3): p. 563-588 DOI: <https://doi.org/10.1111/j.1151-2916.1993.tb03645.x>.
43. Yatoo, M.A., F. Habib, A.H. Malik, M.J. Qazi, S. Ahmad, M.A. Ganayee, and Z.

References

- Ahmad, *Solid-oxide fuel cells: A critical review of materials for cell components*. MRS Communications, 2023. **13**(3): p. 378-384 DOI: <https://doi.org/10.1557/s43579-023-00371-0>.
44. Berenov, A.V., A. Atkinson, J.A. Kilner, E. Bucher and W. Sitte, *Oxygen tracer diffusion and surface exchange kinetics in La_{0.6}Sr_{0.4}CoO₃–δ*. Solid State Ionics, 2010. **181**(17): p. 819-826 DOI: <https://doi.org/10.1016/j.ssi.2010.04.031>.
45. Lee, K.T., H.S. Yoon and E.D. Wachsman, *The evolution of low temperature solid oxide fuel cells*. Journal of Materials Research, 2012. **27**(16): p. 2063-2078 DOI: <https://doi.org/10.1557/jmr.2012.194>.
46. Wachsman, E.D. and K.T. Lee, *Lowering the Temperature of Solid Oxide Fuel Cells*. Science, 2011. **334**(6058): p. 935-939 DOI: <https://doi.org/10.1126/science.1204090>.
47. Tsoga, A., A. Gupta, A. Naoumidis and P. Nikolopoulos, *Gadolinia-doped ceria and yttria stabilized zirconia interfaces: regarding their application for SOFC technology*. Acta Materialia, 2000. **48**(18): p. 4709-4714 DOI: [https://doi.org/10.1016/S1359-6454\(00\)00261-5](https://doi.org/10.1016/S1359-6454(00)00261-5).
48. Z, C. and W. J-H, "Anodes", in *Solid oxide fuel cells: materials properties and performance*, J. Fergus, et al., Editors. 2009, Taylor & Francis Group DOI: <https://doi.org/10.1201/9781420088847>.
49. Niewolak, L., F. Tietz and W.J. Quadakkers, *7 - Interconnects*, in *High-Temperature Solid Oxide Fuel Cells for the 21st Century (Second Edition)*, K. Kendall and M. Kendall, Editors. 2016, Academic Press: Boston. p. 195-254 DOI: <https://doi.org/10.1016/B978-0-12-410453-2.00007-5>.
50. Wang, S., B. Lin, Y. Dong, D. Fang, H. Ding, X. Liu, and G. Meng, *Stable, easily sintered Ca-Zn-doped YCrO₃ as novel interconnect materials for co-fired yttrium-stabilized zirconia-based solid oxide fuel cells*. Journal of Power Sources, 2009. **188**(2): p. 483-488 DOI: <https://doi.org/10.1016/j.jpowsour.2008.12.005>.
51. Park, B.K., J.W. Lee, S.B. Lee, T.H. Lim, S.J. Park, R.H. Song, W.B. Im, and D.R. Shin, *La-doped SrTiO₃ interconnect materials for anode-supported flat-tubular solid oxide fuel cells*. International Journal of Hydrogen Energy, 2012. **37**(5): p. 4319-4327 DOI: <https://doi.org/10.1016/j.ijhydene.2011.10.125>.
52. Mori, M., Z. Wang, N. Serizawa and T. Itoh, *Evaluation of SrTi_{1-x}CoxO₃ perovskites (0≤x≤0.2) as interconnect materials for solid oxide fuel cells*. Journal of Fuel Cell Science and Technology, 2011. **8**(5) DOI: <https://doi.org/10.1115/1.4003761>.
53. Tietz, F., H.P. Buchkremer and D. Stöver, *Components manufacturing for solid oxide fuel cells*. Solid State Ionics, 2002. **152-153**: p. 373-381 DOI: [https://doi.org/10.1016/S0167-2738\(02\)00344-2](https://doi.org/10.1016/S0167-2738(02)00344-2).
54. Kofstad, P., *High temperature corrosion*. 1988: Elsevier Applied Science Publishers LTD. 558 DOI: <https://doi.org/10.1002/crat.2170240408>.
55. Goebel, C., A.G. Fefekos, J.-E. Svensson and J. Froitzheim, *Does the conductivity of interconnect coatings matter for solid oxide fuel cell applications?* Journal of Power Sources, 2018. **383**: p. 110-114 DOI: <https://doi.org/10.1016/j.jpowsour.2018.02.060>.
56. Huczkowski, P., N. Christicmsen, V. Shemet, L. Niewolak, J. Piron-Abellan, L. Singheiser, and W.J. Quadakkers, *Growth mechanisms and electrical conductivity of oxide scales on ferritic steels proposed as interconnect materials for SOFC's*. Fuel Cells, 2006. **6**(2): p. 93-99 DOI: <https://doi.org/10.1002/fuce.200500110>.
57. Jackson, R.W., F.S. Pettit and G.H. Meier, *The behavior of nickel and silver in a simulated solid oxide fuel cell environment*. Journal of Power Sources, 2008. **185**(2): p. 1030-1039 DOI: <https://doi.org/10.1016/j.jpowsour.2008.08.056>.
58. Bianco, M., M. Linder, Y. Larring, F. Greco and J. Van herle, *Chapter 7 - Lifetime Issues for Solid Oxide Fuel Cell Interconnects*, in *Solid Oxide Fuel Cell Lifetime and*

- Reliability*, N.P. Brandon, E. Ruiz-Trejo, and P. Boldrin, Editors. 2017, Academic Press. p. 121-144 DOI: <https://doi.org/10.1016/B978-0-08-101102-7.00007-6>.
59. Chevalier, S., *10 - Formation and growth of protective alumina scales*, in *Developments in High Temperature Corrosion and Protection of Materials*, W. Gao and Z. Li, Editors. 2008, Woodhead Publishing. p. 290-328 DOI: <https://doi.org/10.1533/9781845694258.2.290>.
60. Matsumura, T., *The electrical properties of alumina at high temperatures*. Canadian Journal of Physics, 1966. **44**(8): p. 1685-1698 DOI: <https://doi.org/10.1139/p66-143>.
61. Pappis, J. and W. Kingery, *Electrical properties of single-crystal and polycrystalline alumina at high temperatures*. Journal of the American Ceramic Society, 1961. **44**(9): p. 459-464 DOI: <https://doi.org/10.1111/j.1151-2916.1961.tb13756.x>.
62. Arizumi, T. and S. Tani, *On the Electrical Conductivity of Alumina*. Journal of the Physical Society of Japan, 1950. **5**(6): p. 442-447 DOI: <https://doi.org/10.1143/JPSJ.5.442>.
63. Holt, A. and P. Kofstad, *Electrical conductivity and defect structure of Cr₂O₃. II. Reduced temperatures (<~1000°C)*. Solid State Ionics, 1994. **69**(2): p. 137-143 DOI: [https://doi.org/10.1016/0167-2738\(94\)90402-2](https://doi.org/10.1016/0167-2738(94)90402-2).
64. Zhang, J. and D.P. Wilkinson, "Interconnects", in *Solid oxide fuel cells: materials properties and performance*, J. Fergus, et al., Editors. 2009, Taylor & Francis Group: Florida DOI: <https://doi.org/10.1201/9781420088847>.
65. Birks, N., G.H. Meier and F.S. Pettit, *Introduction to the high temperature oxidation of metals*. 2006: Cambridge University Press DOI: <https://doi.org/10.1017/CBO9781139163903>.
66. Atkins, P., *Shriver and Atkins' inorganic chemistry*. 2010: Oxford University Press, USA.
67. Young, J., *Chapter 2 Enabling Theory*, in *Corrosion Series*, D.J. Young, Editor. 2008, Elsevier Science. p. 29-79 DOI: [https://doi.org/10.1016/S1875-9491\(08\)00002-1](https://doi.org/10.1016/S1875-9491(08)00002-1).
68. Khanna, A.S., *Introduction to High Temperature Oxidation and Corrosion*. 2002: ASM International.
69. Birks, N., G.H. Meier and F.S. Pettit, *Mechanisms of oxidation*, in *Introduction to the High Temperature Oxidation of Metals*, N. Birks, G.H. Meier, and F.S. Pettit, Editors. 2006, Cambridge University Press: Cambridge. p. 39-74 DOI: <https://doi.org/10.1017/CBO9781139163903.005>.
70. Young, J., *Chapter 3 Oxidation of Pure Metals*, in *Corrosion Series*, D.J. Young, Editor. 2008, Elsevier Science. p. 81-137 DOI: [https://doi.org/10.1016/S1875-9491\(08\)00003-3](https://doi.org/10.1016/S1875-9491(08)00003-3).
71. Wagner, C., *Beitrag zur theorie des anlaufvorgangs*. Zeitschrift für physikalische Chemie, 1933. **21**(1): p. 25-41 DOI: <https://doi.org/10.1515/zpch-1933-2105>.
72. Evans, H.E., A.T. Donaldson and T.C. Gilmour, *Mechanisms of Breakaway Oxidation and Application to a Chromia-Forming Steel*. Oxidation of Metals, 1999. **52**(5): p. 379-402 DOI: <https://doi.org/10.1023/A:1018855914737>.
73. Tedmon, C.S., *The Effect of Oxide Volatilization on the Oxidation Kinetics of Cr and Fe-Cr Alloys*. Journal of The Electrochemical Society, 1966. **113**(8): p. 766 DOI: <https://doi.org/10.1149/1.2424115>.
74. West, A.R., *2 Crystal Defects, Non-Stoichiometry and Solid Solutions*, in *Solid state chemistry and its applications*. 2022, John Wiley & Sons.
75. Asteman, H. 2002 *Water Vapour induced active oxidation of stainless steel*, University of Gothenburg, Ph.D thesis
76. West, A.R., *8 Electrical Properties*, in *Solid state chemistry and its applications*. 2022, John Wiley & Sons.

References

77. Latu-Romain, L., Y. Parsa, M. Ollivier, S. Mathieu, M. Vilasi, G. Renou, F. Robaut, and Y. Wouters, *About the control of semiconducting properties of chromia: investigation using photoelectrochemistry and orientation mapping in a TEM*. Materials at High Temperatures, 2018. **35**(1-3): p. 159-167 DOI: <https://doi.org/10.1080/09603409.2017.1389113>.
78. Holt, A. and P. Kofstad, *Electrical conductivity of Cr₂O₃ doped with TiO₂*. Solid State Ionics, 1999. **117**(1): p. 21-25 DOI: [https://doi.org/10.1016/S0167-2738\(98\)00244-6](https://doi.org/10.1016/S0167-2738(98)00244-6).
79. Blackburn, P.E., M. Hoch and H.L. Johnston, *The Vaporization of Molybdenum and Tungsten Oxides*. The Journal of Physical Chemistry, 1958. **62**(7): p. 769-773 DOI: <https://doi.org/10.1021/j150565a001>.
80. Sachitanand, R., M. Sattari, J.-E. Svensson and J. Froitzheim, *Evaluation of the oxidation and Cr evaporation properties of selected FeCr alloys used as SOFC interconnects*. International Journal of Hydrogen Energy, 2013. **38**(35): p. 15328-15334 DOI: <https://doi.org/10.1016/j.ijhydene.2013.09.044>.
81. Stanislowski, M., J. Froitzheim, L. Niewolak, W.J. Quadakkers, K. Hilpert, T. Markus, and L. Singheiser, *Reduction of chromium vaporization from SOFC interconnectors by highly effective coatings*. Journal of Power Sources, 2007. **164**(2): p. 578-589 DOI: <https://doi.org/10.1016/j.jpowsour.2006.08.013>.
82. Caplan, D. and M. Cohen, *The Volatilization of Chromium Oxide*. Journal of The Electrochemical Society, 1961. **108**(5): p. 438 DOI: <https://doi.org/10.1149/1.2428106>.
83. Falk-Windisch, H., J.E. Svensson and J. Froitzheim, *The effect of temperature on chromium vaporization and oxide scale growth on interconnect steels for Solid Oxide Fuel Cells*. Journal of Power Sources, 2015. **287**: p. 25-35 DOI: <https://doi.org/10.1016/j.jpowsour.2015.04.040>.
84. Gindorf, C., L. Singheiser and K. Hilpert, *Vaporisation of chromia in humid air*. Journal of Physics and Chemistry of Solids, 2005. **66**(2): p. 384-387 DOI: <https://doi.org/10.1016/j.jpcs.2004.06.092>.
85. Hilpert, K., D. Das, M. Miller, D. Peck and R. Weiss, *Chromium vapor species over solid oxide fuel cell interconnect materials and their potential for degradation processes*. Journal of the Electrochemical Society, 1996. **143**(11): p. 3642 DOI: <https://doi.org/10.1149/1.1837264>.
86. Ebbinghaus, B.B.J.C. and Flame, *Thermodynamics of gas phase chromium species: the chromium oxides, the chromium oxyhydroxides, and volatility calculations in waste incineration processes*. 1993. **93**(1-2): p. 119-137 DOI: [https://doi.org/10.1016/0010-2180\(93\)90087-J](https://doi.org/10.1016/0010-2180(93)90087-J).
87. Froitzheim, J., H. Ravash, E. Larsson, L.G. Johansson and J.E. Svensson, *Investigation of Chromium Volatilization from FeCr Interconnects by a Denuder Technique*. Journal of The Electrochemical Society, 2010. **157**(9): p. B1295 DOI: <https://doi.org/10.1149/1.3462987>.
88. Niewolak, L., E. Wessel, L. Singheiser and W.J. Quadakkers, *Potential suitability of ferritic and austenitic steels as interconnect materials for solid oxide fuel cells operating at 600°C*. Journal of Power Sources, 2010. **195**(22): p. 7600-7608 DOI: <https://doi.org/10.1016/j.jpowsour.2010.06.007>.
89. Niewolak, L., L. Garcia-Fresnillo, G.H. Meier and W.J. Quadakkers, *Sigma-phase formation in high chromium ferritic steels at 650 °C*. Journal of Alloys and Compounds, 2015: p. 405-418 DOI: <https://doi.org/10.1016/j.jallcom201503076>.
90. Andy Watson, Marina Bulanova, Jean-Claude Tedenac and MSIT, *Cr-Fe Binary Phase Diagram Evaluation*. 2007. Springer Materials. https://materials.springer.com/msi/phase-diagram/docs/sm_msi_r_10_010528_01_full_LnkDia0

91. Yang, Z., M. Guo, N. Wang, C. Ma, J. Wang and M. Han, *A short review of cathode poisoning and corrosion in solid oxide fuel cell*. International Journal of Hydrogen Energy, 2017. **42**(39): p. 24948-24959 DOI: <https://doi.org/10.1016/j.ijhydene.2017.08.057>.
92. Grolig, J.G., J. Froitzheim and J.E. Svensson, *Coated stainless steel 441 as interconnect material for solid oxide fuel cells: Oxidation performance and chromium evaporation*. Journal of Power Sources, 2014. **248**: p. 1007-1013 DOI: <https://doi.org/10.1016/j.jpowsour.2013.08.089>.
93. Zhao, Y. and J.W. Fergus, *Oxidation of Alloys 430 and 441 in SOFC Dual Atmospheres: Effects of Flow Rate and Humidity*. Journal of The Electrochemical Society, 2012. **159**(3): p. C109 DOI: <https://doi.org/10.1149/2.013203jes>.
94. Rufner, J., P. Gannon, P. White, M. Deibert, S. Teintze, R. Smith, and H. Chen, *Oxidation behavior of stainless steel 430 and 441 at 800°C in single (air/air) and dual atmosphere (air/hydrogen) exposures*. International Journal of Hydrogen Energy, 2008. **33**(4): p. 1392-1398 DOI: <https://doi.org/10.1016/j.ijhydene.2007.12.067>.
95. Li, J., D. Yan, Y. Gong, Y. Jiang, J. Li, J. Pu, B. Chi, and L. Jian, *Investigation of Anomalous Oxidation Behavior of SUS430 Alloy in Solid Oxide Fuel Cell Dual Atmosphere*. Journal of The Electrochemical Society, 2017. **164**(14): p. C945 DOI: <https://doi.org/10.1149/2.0251714jes>.
96. Fergus, J. and Y. Zhao, *Low-Chromium Alloys for Solid Oxide Fuel Cell Interconnects*. ECS Transactions, 2011. **35**(1): p. 2447 DOI: <https://doi.org/10.1149/1.3570242>.
97. Wagner, C., *Reaktionstypen bei der Oxydation von Legierungen*. Zeitschrift für Elektrochemie, Berichte der Bunsengesellschaft für physikalische Chemie, 1959. **63**(7): p. 772-782 DOI: <https://doi.org/10.1002/bbpc.19590630713>.
98. Cunat, P.-J., *Alloying elements in stainless steel and other chromium-containing alloys*. Euro Inox, 2004. **2004**: p. 1-24.
99. Meier, G.H., K. Jung, N. Mu, N.M. Yanar, F.S. Pettit, J. Pirón Abellán, T. Olszewski, L. Nieto Hierro, W.J. Quadakkers, and G.R. Holcomb, *Effect of Alloy Composition and Exposure Conditions on the Selective Oxidation Behavior of Ferritic Fe–Cr and Fe–Cr–X Alloys*. Oxidation of Metals, 2010. **74**(5): p. 319-340 DOI: <https://doi.org/10.1007/s11085-010-9215-5>.
100. Holappa, L., *Chapter 1.6 - Secondary Steelmaking*, in *Treatise on Process Metallurgy*, S. Seetharaman, Editor. 2014, Elsevier: Boston. p. 301-345 DOI: <https://doi.org/10.1016/B978-0-08-096988-6.00012-2>.
101. Srivastava, J.K., M. Prasad and J.B. Wagner, *Electrical Conductivity of Silicon Dioxide Thermally Grown on Silicon*. Journal of The Electrochemical Society, 1985. **132**(4): p. 955 DOI: <https://doi.org/10.1149/1.2113993>.
102. Mikkelsen, L., S. Linderoth and J.B. Bilde-Sørensen, *The Effect of Silicon Addition on the High Temperature Oxidation of a Fe–Cr Alloy*. Materials Science Forum, 2004. **461-464**: p. 117-122 DOI: <https://doi.org/10.4028/www.scientific.net/MSF.461-464.117>.
103. Seo, H.S., D.W. Yun and K.Y. Kim, *Effect of Ti addition on the electric and ionic property of the oxide scale formed on the ferritic stainless steel for SOFC interconnect*. International Journal of Hydrogen Energy, 2012. **37**(21): p. 16151-16160 DOI: <https://doi.org/10.1016/j.ijhydene.2012.08.073>.
104. Jablonski, P.D., C.J. Cowen and J.S. Sears, *Exploration of alloy 441 chemistry for solid oxide fuel cell interconnect application*. Journal of Power Sources, 2010. **195**(3): p. 813-820 DOI: <https://doi.org/10.1016/j.jpowsour.2009.08.023>.
105. Yamamoto, K., Y. Kimura, F.-G. Wei and Y. Mishima, *Design of Laves phase strengthened ferritic heat resisting steels in the Fe–Cr–Nb(–Ni) system*. Materials

References

- Science and Engineering: A, 2002. **329-331**: p. 249-254 DOI: [https://doi.org/10.1016/S0921-5093\(01\)01586-6](https://doi.org/10.1016/S0921-5093(01)01586-6).
106. Stein, F. and A. Leineweber, *Laves phases: a review of their functional and structural applications and an improved fundamental understanding of stability and properties*. Journal of Materials Science, 2021. **56**(9): p. 5321-5427 DOI: <https://doi.org/10.1007/s10853-020-05509-2>.
107. Froitzheim, J., G.H. Meier, L. Niewolak, P.J. Ennis, H. Hattendorf, L. Singheiser, and W.J. Quadakkers, *Development of high strength ferritic steel for interconnect application in SOFCs*. Journal of Power Sources, 2008. **178**(1): p. 163-173 DOI: <https://doi.org/10.1016/j.jpowsour.2007.12.028>.
108. PFEIL, L. and W. GRIFFITHS, *Improvement in heat-resisting alloys*. 1937. United Kingdom. 459848.
109. Naumenko, D., B.A. Pint and W.J. Quadakkers, *Current Thoughts on Reactive Element Effects in Alumina-Forming Systems: In Memory of John Stringer*. Oxidation of Metals, 2016. **86**(1): p. 1-43 DOI: <https://doi.org/10.1007/s11085-016-9625-0>.
110. Hou, P.Y. and J. Stringer, *The effect of reactive element additions on the selective oxidation, growth and adhesion of chromia scales*. Materials Science and Engineering: A, 1995. **202**(1): p. 1-10 DOI: [https://doi.org/10.1016/0921-5093\(95\)09798-8](https://doi.org/10.1016/0921-5093(95)09798-8).
111. Polman, E.A., T. Fransen and P.J. Gellings, *The reactive element effect; ionic processes of grain-boundary segregation and diffusion in chromium oxide scales*. Journal of Physics: Condensed Matter, 1989. **1**(28): p. 4497 DOI: <https://doi.org/10.1088/0953-8984/1/28/001>.
112. Hou, P.Y., *The Reactive Element Effect – Past, Present and Future*. Materials Science Forum, 2011. **696**: p. 39-44 DOI: <https://doi.org/10.4028/www.scientific.net/MSF.696.39>.
113. Whittle, D. and J. Stringer, *Improvements in high temperature oxidation resistance by additions of reactive elements or oxide dispersions*. Philosophical Transactions of the Royal Society of London. Series A, Mathematical and Physical Sciences, 1980. **295**(1413): p. 309-329 DOI: <https://doi.org/10.1098/rsta.1980.0124>.
114. Funkenbusch, A.W., J.G. Smeggil and N.S. Bornstein, *Reactive element - sulfur interaction and oxide scale adherence* Metallurgical transactions a-physical metallurgy and materials science 1985. **16**(6): p. 1164-1166 DOI: <https://doi.org/10.1007/BF02811687>.
115. Lees, D.G., *On the reasons for the effects of dispersions of stable oxides and additions of reactive elements on the adhesion and growth-mechanisms of chromia and alumina scales - the sulfur effect*. Oxidation of Metals, 1987. **27**(1-2): p. 75-81 DOI: <https://doi.org/10.1007/bf00656731>.
116. Fontana, S., S. Chevalier and G. Caboche, *Metallic Interconnects for Solid Oxide Fuel Cell: Performance of Reactive Element Oxide Coating During 10, 20 and 30 Months Exposure*. Oxidation of Metals, 2012. **78**(5): p. 307-328 DOI: <https://doi.org/10.1007/s11085-012-9308-4>.
117. Kurokawa, H., C.P. Jacobson, L.C. DeJonghe and S.J. Visco, *Chromium vaporization of bare and of coated iron–chromium alloys at 1073 K*. Solid State Ionics, 2007. **178**(3): p. 287-296 DOI: <https://doi.org/10.1016/j.ssi.2006.12.010>.
118. Falk-Windisch, H., J. Claqueur, M. Sattari, J.-E. Svensson and J. Froitzheim, *Co- and Ce/Ce-coated ferritic stainless steel as interconnect material for Intermediate Temperature Solid Oxide Fuel Cells*. Journal of Power Sources, 2017. **343**: p. 1-10 DOI: <https://doi.org/10.1016/j.jpowsour.2017.01.045>.
119. Tan, K.H., H.A. Rahman and H. Taib, *Coating layer and influence of transition metal for ferritic stainless steel interconnector solid oxide fuel cell: A review*. International

- Journal of Hydrogen Energy, 2019. **44**(58): p. 30591-30605 DOI: <https://doi.org/10.1016/j.ijhydene.2019.06.155>.
120. Mah, J.C.W., A. Muchtar, M.R. Somalu and M.J. Ghazali, *Metallic interconnects for solid oxide fuel cell: A review on protective coating and deposition techniques*. International Journal of Hydrogen Energy, 2017. **42**(14): p. 9219-9229 DOI: <https://doi.org/10.1016/j.ijhydene.2016.03.195>.
121. Yang, Z., G.-G. Xia, G.D. Maupin and J.W. Stevenson, *Conductive protection layers on oxidation resistant alloys for SOFC interconnect applications*. Surface and Coatings Technology, 2006. **201**(7): p. 4476-4483 DOI: <https://doi.org/10.1016/j.surfcoat.2006.08.082>.
122. Quadakkers, W.J., H. Greiner, M. Hänsel, A. Pattanaik, A.S. Khanna and W. Malléner, *Compatibility of perovskite contact layers between cathode and metallic interconnector plates of SOFCs*. Solid State Ionics, 1996. **91**(1): p. 55-67 DOI: [https://doi.org/10.1016/S0167-2738\(96\)00425-0](https://doi.org/10.1016/S0167-2738(96)00425-0).
123. Petric, A. and H. Ling, *Electrical conductivity and thermal expansion of spinels at elevated temperatures*. Journal of the American Ceramic Society, 2007. **90**(5): p. 1515-1520 DOI: <https://doi.org/10.1111/j.1551-2916.2007.01522.x>.
124. Han, S.J., Z. Pala and S. Sampath, *Plasma sprayed manganese–cobalt spinel coatings: Process sensitivity on phase, electrical and protective performance*. Journal of Power Sources, 2016. **304**: p. 234-243 DOI: <https://doi.org/10.1016/j.jpowsour.2015.11.040>.
125. Reddy, M.J., B. Kamecki, B. Talic, E. Zanchi, F. Smeacetto, J.S. Hardy, J.P. Choi, Ł. Mazur, R. Vaßen, S.N. Basu, T. Brylewski, J.-E. Svensson, and J. Froitzheim, *Experimental review of the performances of protective coatings for interconnects in solid oxide fuel cells*. Journal of Power Sources, 2023. **568**: p. 232831 DOI: <https://doi.org/10.1016/j.jpowsour.2023.232831>.
126. Puranen, J., M. Pihlatie, J. Lagerbom, T. Salminen, J. Laakso, L. Hyvärinen, M. Kylmälähti, O. Himanen, J. Kiviahö, and P. Vuoristo, *Influence of powder composition and manufacturing method on electrical and chromium barrier properties of atmospheric plasma sprayed spinel coatings prepared from MnCo₂O₄ and Mn₂CoO₄ + Co powders on Crofer 22 APU interconnectors*. International Journal of Hydrogen Energy, 2014. **39**(30): p. 17246-17257 DOI: <https://doi.org/10.1016/j.ijhydene.2014.08.016>.
127. Froitzheim, J., S. Canovic, M. Nikumaa, R. Sachitanand, L.G. Johansson and J.E. Svensson, *Long term study of Cr evaporation and high temperature corrosion behaviour of Co coated ferritic steel for solid oxide fuel cell interconnects*. Journal of Power Sources, 2012. **220**: p. 217-227 DOI: <http://doi.org/10.1016/j.jpowsour.2012.06.092>.
128. Talic, B., S. Molin, K. Wiik, P.V. Hendriksen and H.L. Lein, *Comparison of iron and copper doped manganese cobalt spinel oxides as protective coatings for solid oxide fuel cell interconnects*. Journal of Power Sources, 2017. **372**: p. 145-156 DOI: <https://doi.org/10.1016/j.jpowsour.2017.10.060>.
129. Lundberg, M.W., R. Berger, J. Westlinder, N. Folkeson and H. Holmberg, *Novel Multilayered PVD-Coating in a Roll to Roll Mass Production Process*. ECS Transactions, 2013. **57**(1): p. 2203 DOI: <https://doi.org/10.1149/05701.2203ecst>.
130. Huang, K., P.Y. Hou and J.B. Goodenough, *Reduced area specific resistance for iron-based metallic interconnects by surface oxide coatings*. Materials Research Bulletin, 2001. **36**(1): p. 81-95 DOI: [https://doi.org/10.1016/S0025-5408\(01\)00506-2](https://doi.org/10.1016/S0025-5408(01)00506-2).
131. Sanchez, M.G., M. Oum, S. Pandyan, A. Majewski, L. Troskialina and R. Steinberger-Wilckens, *Scored 2: O-Steel coatings for reducing degradation*. 2017. Belgium.
132. Reddy, M.J., J.-E. Svensson and J. Froitzheim, *Reevaluating the Cr Evaporation*

References

- Characteristics of Ce/Co Coatings for Interconnect Applications.* ECS Meeting Abstracts, 2021. **MA2021-03**(1): p. 268 DOI: <https://doi.org/10.1149/MA2021-031268mtgabs>.
133. Colinge, J.-P. and C.A. Colinge, *Physics of semiconductor devices*. 2005: Springer Science & Business Media.
134. Balkan, N. and A. Erol, *Intrinsic and Extrinsic Semiconductors*, in *Semiconductors for Optoelectronics: Basics and Applications*, N. Balkan and A. Erol, Editors. 2021, Springer International Publishing: Cham. p. 37-78 DOI: https://doi.org/10.1007/978-3-319-44936-4_2.
135. Holt, A. and P. Kofstad, *Electrical conductivity and defect structure of Cr₂O₃. I. High temperatures (>~1000°C)*. Solid State Ionics, 1994. **69**(2): p. 127-136 DOI: [https://doi.org/10.1016/0167-2738\(94\)90401-4](https://doi.org/10.1016/0167-2738(94)90401-4).
136. Latu-Romain, L., Y. Parsa, S. Mathieu, M. Vilasi, M. Ollivier, A. Galerie, and Y. Wouters, *Duplex n- and p-Type Chromia Grown on Pure Chromium: A Photoelectrochemical and Microscopic Study*. Oxidation of Metals, 2016. **86**(5): p. 497-509 DOI: <https://doi.org/10.1007/s11085-016-9648-6>.
137. Latu-Romain, L., S. Mathieu, M. Vilasi, G. Renou, S. Coindeau, A. Galerie, and Y. Wouters, *The Role of Oxygen Partial Pressure on the Nature of the Oxide Scale on a NiCr Model Alloy*. Oxidation of Metals, 2017. **88**(3): p. 481-493 DOI: <https://doi.org/10.1007/s11085-016-9670-8>.
138. Nagai, H., T. Fujikawa and K.-i. Shoji, *Electrical Conductivity of Cr₂O₃ Doped with La₂O₃, Y₂O₃ and NiO*. Transactions of the Japan Institute of Metals, 1983. **24**(8): p. 581-588 DOI: <https://doi.org/10.2320/matertrans1960.24.581>.
139. Crawford, J.A. and R.W. Vest, *Electrical Conductivity of Single-Crystal Cr₂O₃*. Journal of Applied Physics, 2004. **35**(8): p. 2413-2418 DOI: <https://doi.org/10.1063/1.1702871>.
140. Park, J.H. and K. Natesan, *Electronic transport in thermally grown Cr₂O₃*. Oxidation of Metals, 1990. **33**(1): p. 31-54 DOI: <https://doi.org/10.1007/BF00665668>.
141. Huang, K., P.Y. Hou and J.B. Goodenough, *Characterization of iron-based alloy interconnects for reduced temperature solid oxide fuel cells*. Solid State Ionics, 2000. **129**(1): p. 237-250 DOI: [https://doi.org/10.1016/S0167-2738\(99\)00329-X](https://doi.org/10.1016/S0167-2738(99)00329-X).
142. Gillot, B., R. Legros, R. Metz and A. Rousset, *Electrical conductivity of copper and nickel manganites in relation with the simultaneous presence of Mn³⁺ and Mn⁴⁺ ions on octahedral sites of the spinel structure*. Solid State Ionics, 1992. **51**(1): p. 7-9 DOI: [https://doi.org/10.1016/0167-2738\(92\)90337-O](https://doi.org/10.1016/0167-2738(92)90337-O).
143. Navrotsky, A. and O. Kleppa, *The thermodynamics of cation distributions in simple spinels*. Journal of Inorganic and Nuclear Chemistry, 1967. **29**(11): p. 2701-2714.
144. Reisert, M., M.R. Anisur, L. Lee, A.N. Aphale, J. Hong, M. Yaginuma, T. Shiomi, N. Dale, A.M. Hussain, and P. Singh, *Corrosion of Chromia-Forming and Alumina-Forming Ferritic Stainless Steels under Dual Atmosphere Exposure Conditions*. Journal of The Electrochemical Society, 2021. **168**(11): p. 111506 DOI: <https://doi.org/10.1149/1945-7111/ac38f9>.
145. Reisert, M., A.N. Aphale and P. Singh, *The Effects of Dual Atmosphere Exposure Duration and Temperature on the Growth of Iron Oxide on Ferritic Stainless Steels*. ECS Transactions, 2020. **98**(1): p. 35 DOI: <https://doi.org/10.1149/09801.0035ecst>.
146. Stygar, M., K. Matsuda, S. Lee and T. Brylewski, *Corrosion Behavior of Crofer 22APU for Metallic Interconnects in Single and Dual Atmosphere Exposures at 1073 K*. Acta Physica Polonica A, 2017. **131**(5): p. 1394-1398 DOI: <https://doi.org/10.12693/APhysPolA.131.1394>.
147. Alnegren, P., M. Sattari, J.-E. Svensson and J. Froitzheim, *Severe dual atmosphere*

- effect at 600 °C for stainless steel 441.* Journal of Power Sources, 2016. **301**: p. 170-178 DOI: <https://doi.org/10.1016/j.jpowsour.2015.10.001>.
148. Bredvei Skilbred, A.W. and R. Haugsrud, *The effect of dual atmosphere conditions on the corrosion of Sandvik Sanergy HT.* International Journal of Hydrogen Energy, 2012. **37**(9): p. 8095-8101 DOI: <https://doi.org/10.1016/j.ijhydene.2011.10.096>.
149. Ardigo, M.R., I. Popa, L. Combemale, S. Chevalier, F. Herbst and P. Girardon, *Dual atmosphere study of the K41X stainless steel for interconnect application in high temperature water vapour electrolysis.* International Journal of Hydrogen Energy, 2015. **40**(15): p. 5305-5312 DOI: <https://doi.org/10.1016/j.ijhydene.2015.01.116>.
150. Kurokawa, H., K. Kawamura and T. Maruyama, *Oxidation behavior of Fe-16Cr alloy interconnect for SOFC under hydrogen potential gradient.* Solid State Ionics, 2004. **168**(1): p. 13-21 DOI: <https://doi.org/10.1016/j.ssi.2004.02.008>.
151. Kurokawa, H., Y. Oyama, K. Kawamura and T. Maruyama, *Hydrogen Permeation Through Fe-16Cr Alloy Interconnect in Atmosphere Simulating SOFC at 1073 K.* Journal of The Electrochemical Society, 2004. **151**(8): p. A1264 DOI: <https://doi.org/10.1149/1.1767349>.
152. Yang, Z., M.S. Walker, P. Singh, J.W. Stevenson and T. Norby, *Oxidation Behavior of Ferritic Stainless Steels under SOFC Interconnect Exposure Conditions.* Journal of The Electrochemical Society, 2004. **151**(12): p. B669 DOI: <https://doi.org/10.1149/1.1810393>.
153. Yang, Z., M.S. Walker, P. Singh and J.W. Stevenson, *Anomalous Corrosion Behavior of Stainless Steels under SOFC Interconnect Exposure Conditions.* Electrochemical and Solid-State Letters, 2003. **6**(10): p. B35 DOI: <https://doi.org/10.1149/1.1603012>.
154. Gannon, P. and R. Amendola, *High-Temperature, Dual-Atmosphere Corrosion of Solid-Oxide Fuel Cell Interconnects.* JOM, 2012. **64**(12): p. 1470-1476 DOI: <https://doi.org/10.1007/s11837-012-0473-3>.
155. Young, D.J., J. Zurek, L. Singheiser and W.J. Quadakkers, *Temperature dependence of oxide scale formation on high-Cr ferritic steels in Ar-H₂-H₂O.* Corrosion Science, 2011. **53**(6): p. 2131-2141 DOI: <https://doi.org/10.1016/j.corsci.2011.02.031>.
156. Nakagawa, K., Y. Matsunaga and T. Yanagisawa, *Corrosion behavior of ferritic steels on the air sides of boiler tubes in a steam/air dual environment.* Materials at High Temperatures, 2003. **20**(1): p. 67-73 DOI: <https://doi.org/10.1179/mht.2003.010>.
157. Kiuchi, K. and R.B. McLellan, *The solubility and diffusivity of hydrogen in well-annealed and deformed iron.* Acta Metallurgica, 1983. **31**(7): p. 961-984 DOI: [https://doi.org/10.1016/0001-6160\(83\)90192-X](https://doi.org/10.1016/0001-6160(83)90192-X).
158. Song, E.J., D.-W. Suh and H.K.D.H. Bhadeshia, *Theory for hydrogen desorption in ferritic steel.* Computational Materials Science, 2013. **79**: p. 36-44 DOI: <https://doi.org/10.1016/j.commatsci.2013.06.008>.
159. Higginson, R.L. and G. Green, *Whisker growth morphology of high temperature oxides grown on 304 stainless steel.* Corrosion Science, 2011. **53**(5): p. 1690-1693 DOI: <https://doi.org/10.1016/j.corsci.2011.01.026>.
160. Leistikow, S., I. Wolf and H.J. Grabke, *Effects of Cold Work on the Oxidation Behavior and Carburization Resistance of Alloy 800.* Werkstoffe Und Korrosion-Materials and Corrosion, 1987. **38**(10): p. 556-562 DOI: <https://doi.org/10.1002/maco.19870381003>.
161. Grabke, H.J., E.M. Muller-Lorenz, S. Strauss, E. Pippel and J. Woltersdorf, *Effects of Grain Size, Cold Working, and Surface Finish on the Metal-Dusting Resistance of Steels.* Oxidation of Metals, 1998. **50**(3): p. 241-254 DOI: <https://doi.org/10.1023/A:1018888321213>.
162. Holcomb, G.R., M. Ziomek-Moroz, S.D. Cramer, B.S. Covino and S.J. Bullard, *Dual-environment effects on the oxidation of metallic interconnects.* Journal of Materials

References

- Engineering and Performance, 2006. **15**(4): p. 404-409 DOI: <https://doi.org/10.1361/105994906X117198>.
163. Chyrkin, A., C. Cossu, J.-E. Svensson and J. Froitzheim, *Internal Oxidation of a Fe–Cr Binary Alloy at 700–900 °C: The Role of Hydrogen and Water Vapor*. Oxidation of Metals, 2022. **98**(3): p. 273-289 DOI: <https://doi.org/10.1007/s11085-022-10121-7>.
164. Essuman, E., G.H. Meier, J. Zurek, M. Hänsel, L. Singheiser and W.J. Quadakkers, *Enhanced internal oxidation as trigger for breakaway oxidation of Fe-Cr alloys in gases containing water vapor*. Scripta Materialia, 2007. **57**(9): p. 845-848 DOI: <https://doi.org/10.1016/j.scriptamat.2007.06.058>.
165. Sand, T. 2019 *High Temperature Corrosion Behaviour of Ni-base Alloys and FeCrAl Alloys—The Influence of Water Vapour*, Chalmers Tekniska Hogskola (Sweden)
166. Fournier-Salaün, M.-C. and P. Salaün, *Quantitative determination of hexavalent chromium in aqueous solutions by UV-Vis spectrophotometer*. Central European Journal of Chemistry, 2007. **5**(4): p. 1084-1093 DOI: <https://doi.org/10.2478/s11532-007-0038-4>.
167. Egerton, R.F., *The Scanning Electron Microscope*, in *Physical Principles of Electron Microscopy: An Introduction to TEM, SEM, and AEM*, R.F. Egerton, Editor. 2005, Springer US: Boston, MA. p. 125-153 DOI: https://doi.org/10.1007/0-387-26016-1_5.
168. Zhou, W., R. Apkarian, Z.L. Wang and D. Joy, *Fundamentals of Scanning Electron Microscopy (SEM)*, in *Scanning Microscopy for Nanotechnology: Techniques and Applications*, W. Zhou and Z.L. Wang, Editors. 2007, Springer New York: New York, NY. p. 1-40 DOI: https://doi.org/10.1007/978-0-387-39620-0_1.
169. Goldstein, J.I., D.E. Newbury, J.R. Michael, N.W.M. Ritchie, J.H.J. Scott and D.C. Joy, *Backscattered Electrons*, in *Scanning Electron Microscopy and X-Ray Microanalysis*, J.I. Goldstein, et al., Editors. 2018, Springer New York: New York, NY. p. 15-28 DOI: https://doi.org/10.1007/978-1-4939-6676-9_2.
170. Goldstein, J.I., D.E. Newbury, J.R. Michael, N.W.M. Ritchie, J.H.J. Scott and D.C. Joy, *Electron Beam—Specimen Interactions: Interaction Volume*, in *Scanning Electron Microscopy and X-Ray Microanalysis*, J.I. Goldstein, et al., Editors. 2018, Springer New York: New York, NY. p. 1-14 DOI: https://doi.org/10.1007/978-1-4939-6676-9_1.
171. Goldstein, J.I., D.E. Newbury, J.R. Michael, N.W.M. Ritchie, J.H.J. Scott and D.C. Joy, *Energy Dispersive X-ray Spectrometry: Physical Principles and User-Selected Parameters*, in *Scanning Electron Microscopy and X-Ray Microanalysis*, J.I. Goldstein, et al., Editors. 2018, Springer New York: New York, NY. p. 209-234 DOI: https://doi.org/10.1007/978-1-4939-6676-9_16.
172. Van Leer, B., L.A. Giannuzzi and P. Anzalone, *Applications of FIB and DualBeam for Nanofabrication*, in *Scanning Microscopy for Nanotechnology: Techniques and Applications*, W. Zhou and Z.L. Wang, Editors. 2007, Springer New York: New York, NY. p. 225-236 DOI: https://doi.org/10.1007/978-0-387-39620-0_8.
173. Egerton, R.F., *The Transmission Electron Microscope*, in *Physical Principles of Electron Microscopy: An Introduction to TEM, SEM, and AEM*, R.F. Egerton, Editor. 2005, Springer US: Boston, MA. p. 57-92 DOI: https://doi.org/10.1007/0-387-26016-1_3.
174. Epp, J., *4 - X-ray diffraction (XRD) techniques for materials characterization*, in *Materials Characterization Using Nondestructive Evaluation (NDE) Methods*, G. Hübschen, et al., Editors. 2016, Woodhead Publishing. p. 81-124 DOI: <https://doi.org/10.1016/B978-0-08-100040-3.00004-3>.
175. Smart, L.E. and E.A. Moore, *Physical Methods for Characterising Solids*, in *Solid state chemistry: an introduction*. 2016, CRC press: Boca Raton. p. 62 DOI: <https://doi.org/10.1016/B978-0-08-100040-3.00004-3>.

- [https://doi.org/10.1201/b12047.](https://doi.org/10.1201/b12047)
176. Grolig, J.G., J. Froitzheim and J.-E. Svensson, *Coated stainless steel 441 as interconnect material for solid oxide fuel cells: Evolution of electrical properties*. Journal of Power Sources, 2015. **284**: p. 321-327 DOI: <https://doi.org/10.1016/j.jpowsour.2015.03.029>.
177. Canovic, S., J. Froitzheim, R. Sachitanand, M. Nikumaa, M. Halvarsson, L.G. Johansson, and J.E. Svensson, *Oxidation of Co- and Ce-nanocoated FeCr steels: A microstructural investigation*. Surface and Coatings Technology, 2013. **215**: p. 62-74 DOI: <https://doi.org/10.1016/j.surfcoat.2012.08.096>.
178. Directorate-General for Internal Market, I., Entrepreneurship and SMEs and E. Commission. https://ec.europa.eu/growth/sectors/raw-materials/areas-specific-interest/critical-raw-materials_en. 2020.
179. Pause, L., *Chapter 10 - Conflicts related to resources: The case of cobalt mining in the Democratic Republic of Congo*, in *The Material Basis of Energy Transitions*, A. Bleicher and A. Pehlken, Editors. 2020, Academic Press. p. 153-167 DOI: <https://doi.org/10.1016/B978-0-12-819534-5.00010-6>.
180. Farjana, S.H., N. Huda and M.A.P. Mahmud, *Life cycle assessment of cobalt extraction process*. Journal of Sustainable Mining, 2019. **18**(3): p. 150-161 DOI: <https://doi.org/10.1016/j.jsm.2019.03.002>.
181. Segerdahl, K., J.E. Svensson and L.G. Johansson, *Protective and Nonprotective Behavior of 11% Cr Steel in O₂ + H₂O Environment at 450-700°C*. Journal of The Electrochemical Society, 2004. **151**(7): p. B394 DOI: <https://doi.org/10.1149/1.1753584>.
182. Reddy, M.J., J.-E. Svensson and J. Froitzheim, *Evaluating candidate materials for balance of plant components in SOFC: Oxidation and Cr evaporation properties*. Corrosion Science, 2021. **190**: p. 109671 DOI: <https://doi.org/10.1016/j.corsci.2021.109671>.
183. Sand, T., A. Edgren, C. Geers, V. Asokan, J. Eklund, T. Helander, J.E. Svensson, and L.G. Johansson, *Exploring the Effect of Silicon on the High Temperature Corrosion of Lean FeCrAl Alloys in Humid Air*. Oxidation of Metals, 2021. **95**(3): p. 221-238 DOI: <https://doi.org/10.1007/s11085-020-10019-2>.
184. Eklund, J., B. Jönsson, A. Persdotter, J. Liske, J.E. Svensson and T. Jonsson, *The influence of silicon on the corrosion properties of FeCrAl model alloys in oxidizing environments at 600 °C*. Corrosion Science, 2018. **144**: p. 266-276 DOI: <https://doi.org/10.1016/j.corsci.2018.09.004>.
185. Asteman, H., J.E. Svensson, M. Norell and L.G. Johansson, *Influence of Water Vapor and Flow Rate on the High-Temperature Oxidation of 304L; Effect of Chromium Oxide Hydroxide Evaporation*. Oxidation of Metals, 2000. **54**(1): p. 11-26 DOI: <https://doi.org/10.1023/A:1004642310974>.
186. Spotorno, R., D. Paravidino, S. Delsante and P. Piccardo, *Volatilization of chromium from AISI 441 stainless steel: Time and temperature dependence*. Surface and Coatings Technology, 2022. **433**: p. 128125 DOI: <https://doi.org/10.1016/j.surfcoat.2022.128125>.
187. Crawmer, D.E., *Thermal Spray Processes*, in *Thermal Spray Technology*, R.C. Tucker, Jr., Editor. 2013, ASM International. p. 0 DOI: <https://doi.org/10.31399/asm.hb.v05a.a0005718>.
188. Talic, B., P.V. Hendriksen, K. Wiik and H.L. Lein, *Diffusion couple study of the interaction between Cr₂O₃ and MnCo₂O₄ doped with Fe and Cu*. Solid State Ionics, 2019. **332**: p. 16-24 DOI: <https://doi.org/10.1016/j.ssi.2019.01.008>.
189. Molin, S., P. Jasinski, L. Mikkelsen, W. Zhang, M. Chen and P.V. Hendriksen, *Low*

References

- temperature processed MnCo₂O₄ and MnCo_{1.8}Fe_{0.2}O₄ as effective protective coatings for solid oxide fuel cell interconnects at 750 °C.* Journal of Power Sources, 2016. **336**: p. 408-418 DOI: <https://doi.org/10.1016/j.jpowsour.2016.11.011>.
190. Stringer, J., *The reactive element effect in high-temperature corrosion.* Materials Science and Engineering: A, 1989. **120-121**: p. 129-137 DOI: [https://doi.org/10.1016/0921-5093\(89\)90730-2](https://doi.org/10.1016/0921-5093(89)90730-2).
191. Froitzheim, J., L. Niewolak, M. Brandner, L. Singheiser and W.J. Quadakkers, *Anode Side Diffusion Barrier Coating for Solid Oxide Fuel Cells Interconnects.* Journal of Fuel Cell Science and Technology, 2010. **7**(3) DOI: <https://doi.org/10.1115/1.3182731>.
192. Windisch, H.F. 2017 *Improved Oxidation Resistance and Reduced Cr Vaporization from Thin-Film Coated Solid Oxide Fuel Cell Interconnects,*
193. Schemmel, R., L. Philipp, J. Stringer and R. Gordon. Hanford Engineering Development Lab., Richland, WA (United States). *Electrical properties of a polycrystalline alumina sample.* 1972.
194. Cohen, J., *Electrical conductivity of alumina.* Journal of the American Ceramic Society, 1959. **38**(9): p. 441-46.
195. Meyer, B.K., A. Polity, D. Reppin, M. Becker, P. Hering, P.J. Klar, T. Sander, C. Reindl, J. Benz, M. Eickhoff, C. Heiliger, M. Heinemann, J. Bläsing, A. Krost, S. Shokovets, C. Müller, and C. Ronning, *Binary copper oxide semiconductors: From materials towards devices.* physica status solidi (b), 2012. **249**(8): p. 1487-1509 DOI: <https://doi.org/10.1002/pssb.201248128>.
196. Goebel, C., P. Alnegren, R. Faust, J.-E. Svensson and J. Froitzheim, *The effect of pre-oxidation parameters on the corrosion behavior of AISI 441 in dual atmosphere.* International Journal of Hydrogen Energy, 2018. **43**(31): p. 14665-14674 DOI: <https://doi.org/10.1016/j.ijhydene.2018.05.165>.
197. Ponsoni, J.B., V. Aranda, T.d.S. Nascimento, R.B. Strozi, W.J. Botta and G. Zepon, *Design of multicomponent alloys with C14 laves phase structure for hydrogen storage assisted by computational thermodynamic.* Acta Materialia, 2022. **240**: p. 118317 DOI: <https://doi.org/10.1016/j.actamat.2022.118317>.
198. Tomas, M., A. Visibile, J.E. Svensson and J. Froitzheim, *Novel coatings for protecting solid oxide fuel cell interconnects against the dual-atmosphere effect.* International Journal of Hydrogen Energy, 2023. **48**(48): p. 18405-18419 DOI: <https://doi.org/10.1016/j.ijhydene.2023.01.313>.
199. Serra, E., A. Calza Bini, G. Cosoli and L. Pilloni, *Hydrogen Permeation Measurements on Alumina.* Journal of the American Ceramic Society, 2005. **88**(1): p. 15-18 DOI: <https://doi.org/10.1111/j.1551-2916.2004.00003.x>.
200. Belonoshko, A.B., A. Rosengren, Q. Dong, G. Hultquist and C. Leygraf, *First-principles study of hydrogen diffusion in α-Al₂O₃ and liquid alumina.* Physical Review B, 2004. **69**(2): p. 024302 DOI: <https://doi.org/10.1103/PhysRevB.69.024302>.
201. Shirasaka, H., T. Shimonosono, Y. Hirata and S. Sameshima, *Analysis of gas permeability of porous alumina powder compacts.* Journal of Asian Ceramic Societies, 2013. **1**(4): p. 368-373 DOI: <https://doi.org/10.1016/j.jascer.2013.11.002>.
202. Rebak, R.B. and Y.-J. Kim. *Hydrogen Diffusion in FeCrAl Alloys for Light Water Reactors Cladding Applications.* in ASME 2016 Pressure Vessels and Piping Conference. 2016. DOI: <https://doi.org/10.1115/pvp2016-63164>.
203. Van Deventer, E.H. and V.A. Maroni, *Hydrogen permeation characteristics of some Fe-Cr-Al alloys.* Journal of Nuclear Materials, 1983. **113**(1): p. 65-70 DOI: [https://doi.org/10.1016/0022-3115\(83\)90167-8](https://doi.org/10.1016/0022-3115(83)90167-8).
204. Somjit, V. and B. Yildiz, *Doping α-Al₂O₃ to reduce its hydrogen permeability: Thermodynamic assessment of hydrogen defects and solubility from first principles.*

- Acta Materialia, 2019. **169**: p. 172-183 DOI: <https://doi.org/10.1016/j.actamat.2019.02.031>.
205. Essuman, E., G.H. Meier, J. Żurek, M. Hänsel, L. Singheiser and W.J. Quadakkers, *Enhanced internal oxidation as trigger for breakaway oxidation of Fe–Cr alloys in gases containing water vapor*. Scripta Materialia, 2007. **57**(9): p. 845-848 DOI: <https://doi.org/10.1016/j.scriptamat.2007.06.058>.
206. Quadakkers, W.J., J. Żurek and M. Hänsel, *Effect of water vapor on high-temperature oxidation of FeCr alloys*. JOM, 2009. **61**(7): p. 44-50 DOI: <https://doi.org/10.1007/s11837-009-0102-y>.
207. Essuman, E., G.H. Meier, J. Żurek, M. Hänsel and W.J. Quadakkers, *The Effect of Water Vapor on Selective Oxidation of Fe–Cr Alloys*. Oxidation of Metals, 2008. **69**(3): p. 143-162 DOI: <https://doi.org/10.1007/s11085-007-9090-x>.
208. Chyrkin, A., C. Cossu, J.-E. Svensson and J. Froitzheim, *Effect of Hydrogen on the Internal Oxidation of a Pd–Cr Alloy in Dual-Atmosphere Conditions*. Oxidation of Metals, 2022. **97**(5): p. 527-538 DOI: <https://doi.org/10.1007/s11085-022-10104-8>.
209. Tomas, M., V. Asokan, J. Puranen, J.E. Svensson and J. Froitzheim, *Efficiencies of cobalt- and copper-based coatings applied by different deposition processes for applications in intermediate-temperature solid oxide fuel cells*. International Journal of Hydrogen Energy, 2022. **47**(76): p. 32628-32640 DOI: <https://doi.org/10.1016/j.ijhydene.2022.07.168>.
210. Tveten, B., G. Hultquist and T. Norby, *Hydrogen in Chromium: Influence on the High-Temperature Oxidation Kinetics in O₂, Oxide-Growth Mechanisms, and Scale Adherence*. Oxidation of Metals, 1999. **51**(3): p. 221-233 DOI: <https://doi.org/10.1023/A:1018866505708>.
211. Norby, T. and R. Haugsrud, *Dense Ceramic Membranes for Hydrogen Separation*, in *Nonporous Inorganic Membranes*. 2006. p. 1-48 DOI: <https://doi.org/10.1002/3527608796.ch1>.
212. Alnegren, P. 2018 *Corrosion of ferritic stainless steel interconnects for solid oxide cells—challenging operating conditions*, Chalmers Tekniska Hogskola (Sweden)
213. Tuller, H.L. and A.S. Nowick, *Defect Structure and Electrical Properties of Nonstoichiometric CeO₂ Single Crystals*. Journal of The Electrochemical Society, 1979. **126**(2): p. 209 DOI: <https://doi.org/10.1149/1.2129007>.
214. Naik, I.K. and T.Y. Tien, *Small-polaron mobility in nonstoichiometric cerium dioxide*. Journal of Physics and Chemistry of Solids, 1978. **39**(3): p. 311-315 DOI: [https://doi.org/10.1016/0022-3697\(78\)90059-8](https://doi.org/10.1016/0022-3697(78)90059-8).
215. Nigara, Y., K. Yashiro, J.O. Hong, T. Kawada and J. Mizusaki, *Hydrogen permeability of YSZ single crystals at high temperatures*. Solid State Ionics, 2004. **171**(1): p. 61-67 DOI: [https://doi.org/10.1016/S0167-2738\(03\)00274-1](https://doi.org/10.1016/S0167-2738(03)00274-1).
216. Khatamian, D., *Diffusion of Hydrogen in Single Crystals of Monoclinic-ZrO₂ and Yttrium Stabilized Cubic Zirconia*. Defect and Diffusion Forum, 2010. **297-301**: p. 631-640 DOI: <https://doi.org/10.4028/www.scientific.net/DDF.297-301.631>.
217. Engels, J., A. Houben and C. Linsmeier, *Hydrogen isotope permeation through yttria coatings on Eurofer in the diffusion limited regime*. International Journal of Hydrogen Energy, 2021. **46**(24): p. 13142-13149 DOI: <https://doi.org/10.1016/j.ijhydene.2021.01.072>.
218. Yen, S.K., I.B. Huang and Z.S. Yen, *Effects of Electrolytic Zirconium Oxide Coating on Hydrogen Permeation of AISI 430 Stainless Steel*. Corrosion, 2000. **56**(10): p. 998-1004 DOI: <https://doi.org/10.5006/1.3294391>.
219. Hatano, Y., K. Zhang and K. Hashizume, *Fabrication of ZrO₂ coatings on ferritic steel by wet-chemical methods as a tritium permeation barrier*. Physica Scripta, 2011.

References

- 2011(T145): p. 014044 DOI: <https://doi.org/10.1088/0031-8949/2011/T145/014044>.
220. Josefsson, H., F. Liu, J.-E. Svensson, M. Halvarsson and L.-G. Johansson, *Oxidation of FeCrAl alloys at 500–900°C in dry O₂*. Materials and Corrosion, 2005. **56**(11): p. 801-805 DOI: <https://doi.org/10.1002/maco.200503882>.
221. Skilbred, A.W.B. and R. Haugsrud, *The Effect of Water Vapour on the Corrosion of Sandvik Sanergy HT Under Dual Atmosphere Conditions*. Oxidation of Metals, 2013. **79**(5): p. 639-654 DOI: <https://doi.org/10.1007/s11085-012-9313-7>.
222. Goebel, C., R. Berger, C. Bernuy-Lopez, J. Westlinder, J.-E. Svensson and J. Froitzheim, *Long-term (4 year) degradation behavior of coated stainless steel 441 used for solid oxide fuel cell interconnect applications*. Journal of Power Sources, 2020. **449**: p. 227480 DOI: <https://doi.org/10.1016/j.jpowsour.2019.227480>.
223. Piccardo, P., P. Gannon, S. Chevalier, M. Viviani, A. Barbucci, G. Caboche, R. Amendola, and S. Fontana, *ASR evaluation of different kinds of coatings on a ferritic stainless steel as SOFC interconnects*. Surface and Coatings Technology, 2007. **202**(4): p. 1221-1225 DOI: <https://doi.org/10.1016/j.surfcoat.2007.07.096>.
224. Xiong, Y.-P., H. Kishimoto, K. Yamaji, M. Yoshinaga, T. Horita, M.E. Brito, and H. Yokokawa, *Electronic conductivity of pure ceria*. Solid State Ionics, 2011. **192**(1): p. 476-479 DOI: <https://doi.org/10.1016/j.ssi.2010.07.017>.
225. Ikeda, S., O. Sakurai, K. Uematsu, N. Mizutani and M. Kato, *Electrical conductivity of yttria-stabilized zirconia single crystals*. Journal of Materials Science, 1985. **20**(12): p. 4593-4600 DOI: <https://doi.org/10.1007/BF00559349>.
226. Özkan, O.T. and A.J. Moulson, *The electrical conductivity of single-crystal and polycrystalline aluminium oxide*. Journal of Physics D: Applied Physics, 1970. **3**(6): p. 983 DOI: <https://doi.org/10.1088/0022-3727/3/6/420>.

List of Figures

<i>Figure 1.1: Annual CO₂ emissions by sector worldwide for the period of 1990 – 2020. Source: [7].</i>	2
<i>Figure 1.2: Graphical abstract displaying the different colours attributed to hydrogen, and the end-products, depending on the source of energy and production method used. Partially taken from [10].</i>	3
<i>Figure 2.1: Different fuel cell systems. Adapted from [34].</i>	9
<i>Figure 2.2: Solid oxide fuel cell: a) operating principle; and b) fuel cell stack.</i>	11
<i>Figure 2.3: Ellingham diagram of the selected oxides. Shown are the standard free energies of formation for selected oxides vs. temperature [67].</i>	17
<i>Figure 2.4: Steps in the process of the oxide layer growth on a metal substrate [54]: 1) O₂ adsorption; 2) Oxide nucleation; and 3) Continuous oxide scale growth.</i>	18
<i>Figure 2.5: Typical metal oxidation kinetics.</i>	21
<i>Figure 2.6: Schematic of Schottky and Frenkel point defects common to stoichiometric oxides. The ratio of the ion diameter is not representative of the actual ratio [74].</i>	22
<i>Figure 2.7: Simplified model of diffusion-controlled oxidation in a metal oxide during oxidation. Adapted from [75].</i>	24
<i>Figure 2.8: Rate of Cr vaporisation as a function of gas flow rate at 850 °C in air + 3 % H₂O on Sanergy HT substrate. Data used with permission from [87].</i>	26
<i>Figure 3.1: Space-filling representation of; a) body-centred cubic; and b) faced-centred cubic crystalline structures.</i>	27
<i>Figure 3.2: Binary Fe-Cr phase diagram, adapted from [90]. α-Fe has a BCC crystalline structure, i.e., ferritic phase, and γ-Fe has an FCC crystalline structure, i.e., austenitic phase.</i>	28
<i>Figure 3.3: Space-filling representation of: a) a Perovskite-type structure; and b) a Spinel-type structure.</i>	33
<i>Figure 3.4: Schematic of an interconnect exposed under dual-atmosphere conditions. The ratio of the atom diameter is not representative of the actual ratio.</i>	37
<i>Figure 3.5: Cross-section of a hematite nodule formed on the air-side of a Crofer 22 H foil after exposure in dual-atmosphere conditions (i.e. Ar – 4.8 % H₂ – 3 % H₂O // air – 3 % H₂O) at 600 °C for 336 h.</i>	38
<i>Figure 4.1: Tubular furnace used for the single-atmosphere exposures and Cr(VI) evaporation measurements.</i>	44
<i>Figure 4.2: Schematic representation of the Cr evaporation technique. Courtesy of [125].</i>	45
<i>Figure 4.3: Experimental set-up for the tube furnace exposures and Cr(VI) evaporation measurements based on Froitzheim et al. [87]. Courtesy of [165].</i>	45
<i>Figure 4.4: METTLER TOLEDO XP6 scale used for the mass gain measurements.</i>	46

List of Figures

<i>Figure 4.5: Sample holder used for the dual-atmosphere experiments described in Papers II, IV and V.</i>	46
<i>Figure 4.6: Schematic and operating principle of the dual-atmosphere sample holder used for the exposures involving high hydrogen concentrations in Paper III.</i>	47
<i>Figure 4.7: Schematic of the operating principle of the BIB milling process at different times. The ion source is Ar⁺.</i>	49
<i>Figure 4.8: Schematic of the different SEM signals produced (a-c) and their interaction volumes (d) [167, 168].</i>	50
<i>Figure 4.9: Schematic of: a) Bragg's law; and b) Bragg-Brentano geometry.</i>	52
<i>Figure 4.10: Schematic of the electrode preparation process.</i>	53
<i>Figure 4.11: ASR experimental set-up showing: a) the mounted sample; b) the ProboStat top; and c) the entire set-up.</i>	54
<i>Figure 5.1: Cumulative Cr(VI) evaporation as a function of time for the Cr₂O₃- and Al₂O₃-forming steels exposed at 600 °C for 500 h in air that contained 3 % water vapour. The error bars represent the standard deviation. For Crofer 22 APU and Crofer 22 H, samples from Batch A were used, respectively. The symbols are slightly shifted (± 1 h) to enhance readability.</i>	57
<i>Figure 5.2: Cumulative Cr(VI) evaporation as a function of time for uncoated and coated AISI 441 samples exposed for 1,000 h at 650 °C in air that contained 3 % water vapor. Error bars indicate the standard deviation.</i>	57
<i>Figure 5.3: Mass gains of the different grades of steels exposed for 500 h at 600 °C in air that contained 3 % water vapour. The blue bars represent the net average mass gains, and the orange bars represent the gross average mass gains (corrected for the Cr evaporation). For Crofer 22 APU and Crofer 22 H, samples from Batch A were used, respectively.</i>	59
<i>Figure 5.4: Average mass as a function of time for the PVD-coated, TS-coated, and uncoated samples, all of which were exposed for 1,000 h at 650 °C in air that contained 3 % water vapour. Error bars indicate the standard deviation.</i>	59
<i>Figure 5.5: Grazing-incidence diffractogram performed for 20 h on an AISI 441 sample exposed under single-atmosphere (air + 3 % H₂O) conditions for 500 h at 600 °C.</i>	60
<i>Figure 5.6: SEM Back-scattered Electron (BSE) image of BIB milled cross-section of the investigated PVD and TS coatings exposed to air + 3 % H₂O at 650 °C for 1,000 h.</i>	62
<i>Figure 5.7: EDS mapping of the corresponding PVD and TS coatings exposed to air + 3 % H₂O at 650 °C for 1,000 h.</i>	63
<i>Figure 5.8: ASR measurements performed in air, on different grades of uncoated ferritic stainless steels exposed at 600 °C for 500 h in air + 3 % H₂O. Error bars indicate the standard deviation.</i>	65
<i>Figure 5.9: ASR measurements performed in air on PVD-coated and TS-coated samples exposed at 650 °C for 1,000 h in air + 3 % H₂O. Error bars indicate standard deviation.</i>	65
<i>Figure 5.10: Top-view SEM micrographs of the different investigated steels pre-oxidised for 20 min at 800 °C and exposed under dual-atmosphere conditions at 600 °C for up to 500 h. Crofer 22 APU, AISI 441 and Kanthal EF 101 were exposed to two distinct fuel atmospheres, Atmosphere 1 and</i>	

<i>Atmosphere 2, for 500 h and 168 h, respectively.....</i>	68
<i>Figure 5.11: Photographs and SEM cross-sections of the air-sides of the selected alloys pre-oxidised for 20 min at 800 °C and exposed under dual-atmosphere conditions (Ar-5% H₂ + 3% H₂O // Air + 3 % H₂O) at 600 °C for 500 h. For Crofer 22 APU and Crofer 22 H, samples from Batch A were used, respectively. The insets show high-magnification SEM images of the corresponding alloys.....</i>	69
<i>Figure 5.12: Top-view SEM micrographs of the air-side (a-e) and SEM cross-sectional micrographs of the fuel-side (f-j) of the investigated AISI 441 uncoated and PVD-coated samples on the fuel-side, pre-oxidised for 20 min at 800 °C and exposed under dual-atmosphere conditions (i.e., Atmosphere 1) at 600 °C for up to 3,000 h.....</i>	72
<i>Figure 5.13: Top-view SEM micrographs of the air-side (a-f) and SEM cross-sectional micrographs of the fuel-side (g-l) of the investigated AISI 441 PVD Al₂O₃-coated and Al-coated samples on the fuel-side, exposed under dual-atmosphere conditions (i.e., Atmosphere 1) at 600°C for up to 7,000 h.....</i>	75
<i>Figure 5.14: SEM micrographs of the air-side (Top-view) and fuel-side (Cross-section) of the PVD Al-coated AISI 441 after pre-oxidation for 5 h at 800 °C with a ramp rate of 1 °C/min, in air + 3 % H₂O.</i>	76
<i>Figure 5.15: SEM micrograph representing the line-scan analysis used to determine the inter-diffusion of Al within the sample of an Al-coated AISI 441 sample exposed for 5 h in humid air (3 % H₂O) at 800 °C with up and down ramp rates of 1°C / min.</i>	77
<i>Figure 5.16: Top-view and cross-sectional SEM micrographs of the investigated AISI 441 PVD Ce/Co-coated sample on the air-side, exposed under dual-atmosphere conditions (i.e., Atmosphere 1) at 600 °C for 3,000 h. Inset: Higher-magnification image of selected scale regions.....</i>	78
<i>Figure 5.17: Top-view and cross-sectional SEM micrographs of the investigated AISI 441 PVD Al // Ce/Co-coated sample, exposed under classic dual-atmosphere conditions (i.e., Atmosphere 1) at 600 °C for 7,000 h. Inset: Higher-magnification image of selected scale regions. An Au-layer was sputtered on the fuel-side to enhance the contrast of the cross-section.....</i>	79
<i>Figure 5.18: Optical images of the air-side of the Al- and Al//Ce/Co-coated AISI 441 samples exposed for up to 7,000 h at 600 °C under dual-atmosphere conditions.....</i>	80
<i>Figure 5.19: ASR measurements performed in humid H₂ at 600 °C on uncoated, Cr₂O₃-coated, CeO₂-coated, YSZ-coated, Al₂O₃-coated, and Al-coated samples exposed for 500 h in Ar – 5 % H₂ + 3 % H₂O. The uncoated side of the sample was ground so as to have the ASR contribution of the coating only. The error bars represent the standard deviation. *Al-coated samples were exposed for 168 h in Ar – 5 % H₂ + 3 % H₂O.</i>	82

